

THERMODYNAMIC FEEDBACK OF SEA SPRAY AT AIR-SEA INTERFACE

A Dissertation

Submitted to the Graduate School  
of the University of Notre Dame  
in Partial Fulfillment of the Requirements  
for the Degree of

Doctor of Philosophy

by

Tianze Peng

---

Dr. David H. Richter, Director

Graduate Program in Civil and Environmental Engineering and Earth Sciences

Notre Dame, Indiana

October 2019

# THERMODYNAMIC FEEDBACK OF SEA SPRAY AT AIR-SEA INTERFACE

Abstract

by

Tianze Peng

Sea-spray droplets generated in large quantities under strong winds exchange heat and water vapor with the turbulent airflow, which potentially modifies air-sea heat fluxes. However, questions regarding the appropriate method for modeling the effects of spray on air-sea fluxes still exist due to untested assumptions in existing models and low fidelity in the measurements. In this study, an Eulerian-Lagrangian model is implemented to simulate two-way coupled spray droplets in a turbulent flow via direct numerical simulations. While the study is not meant to replicate a real air-sea interface, the fundamental physics underlying turbulence-droplet coupling is the focus. With high-fidelity simulations with mono- and poly-dispersed droplet size distributions, the dissertation covers topics on: (1) the sensitivity of air-sea heat fluxes on various droplet and flow parameters; (2) fundamental assumptions on the micro-physics and the poly-dispersity of spray droplets using bulk air-sea algorithms; and (3) potential improvements and corrections to the bulk algorithms on parameterizing spray effects. The findings of this dissertation bring insights on the spray micro-physics and feedback effects from a small-scale perspective, which narrows the gap in understanding the spray effects at the air-sea interface for the large-scale modeling community.

To things that seem obvious.

# CONTENTS

Figures . . . . .	vi
Tables . . . . .	xii
Preface . . . . .	xiii
Acknowledgments . . . . .	xiv
Chapter 1: Introduction . . . . .	1
1.1 A mismatch of scales . . . . .	1
1.2 Physical processes at the air-sea interface and sea spray . . . . .	2
1.3 Previous efforts in quantifying spray’s influences in the air-sea heat fluxes . . . . .	5
1.4 Objectives and structures of the dissertation . . . . .	10
Chapter 2: Methodology . . . . .	12
2.1 Overview . . . . .	12
2.2 The Eulerian-Lagrangian algorithm . . . . .	12
2.2.1 Governing equations . . . . .	13
2.2.1.1 Carrier phase . . . . .	13
2.2.1.2 Dispersed phase . . . . .	15
2.2.1.3 Two-way coupling . . . . .	17
2.2.2 Numerical set-up . . . . .	19
2.2.2.1 Simulation domain . . . . .	19
2.2.2.2 Boundary and initial conditions . . . . .	21
2.2.2.3 Selection of other droplet parameters . . . . .	22
2.2.2.4 Droplet size and size distributions . . . . .	24
2.2.3 Timescales of evaporating spray droplets . . . . .	25
2.2.4 Heat fluxes partitioning . . . . .	28
2.3 Bulk parameterizations for spray-mediated heat fluxes . . . . .	29
2.3.1 Heat fluxes in a bulk model . . . . .	29
2.3.2 Estimates of spray-mediated heat fluxes . . . . .	30

Chapter 3: Influence of Evaporating Droplets in the Lower Marine Atmospheric Boundary Layer . . . . .	34
3.1 Overview . . . . .	34
3.2 Results and discussion . . . . .	35
3.2.1 Influence of droplet size . . . . .	35
3.2.1.1 Behaviors of droplets in the turbulence . . . . .	37
3.2.1.2 A statistical view . . . . .	41
3.2.1.3 Heat fluxes . . . . .	42
3.2.2 Influence of mass loading . . . . .	48
3.2.3 Influence of boundary conditions . . . . .	51
3.3 Summary . . . . .	54
Chapter 4: Assessing Bulk Algorithms of Air-Sea Heat Fluxes . . . . .	57
4.1 Overview . . . . .	57
4.2 Results and discussion . . . . .	58
4.2.1 Predicting spray-mediated heat fluxes . . . . .	58
4.2.2 The feedback effect of spray evaporation . . . . .	62
4.2.3 Spray evaporation in turbulent air and its temporal dependence . . . . .	67
4.2.3.1 Influence of spray timescales . . . . .	68
4.2.3.2 The ambient conditions of spray evaporation . . . . .	71
4.2.3.3 A tentative estimate of the equivalent ambient condition . . . . .	74
4.2.4 The importance of spray timescales on estimating spray feedback . . . . .	75
4.3 Summary . . . . .	82
Chapter 5: Feedback in the Poly-dispersed System . . . . .	85
5.1 Introduction . . . . .	85
5.1.1 Background . . . . .	85
5.1.2 Goals of this chapter . . . . .	89
5.1.3 Simulation configurations . . . . .	90
5.1.4 Partitioning spray-mediated fluxes by size . . . . .	90
5.2 Bi-dispersed cases: A test on the superposition of mono-dispersed distributions . . . . .	93
5.2.1 Bi-dispersed droplet size distribution . . . . .	93
5.2.2 Responses in air temperature and humidity . . . . .	93
5.2.3 Responses of heat fluxes . . . . .	96
5.2.4 Statistics on the temperature and radius change of droplets . . . . .	103
5.2.5 Bulk estimates of heat fluxes . . . . .	107
5.2.6 Summary for the bi-dispersed cases . . . . .	109
5.3 Simulations with a poly-dispersed size distribution . . . . .	110
5.3.1 Changes in droplet temperature and radius . . . . .	112
5.3.2 Bulk estimation for the poly-dispersed cases . . . . .	115
5.3.2.1 Spray-mediated heat fluxes . . . . .	115
5.3.2.2 Total heat flux . . . . .	118

5.3.3	Representative droplet sizes of a continuum size distribution . . . . .	120
5.3.3.1	Poly-dispersity and the representative size of SSGFs . . . . .	121
5.3.3.2	Comparisons on air temperature, humidity, and heat fluxes . . . . .	122
5.3.3.3	Effective size range . . . . .	126
5.4	Summary . . . . .	128
Chapter 6: Conclusions . . . . .		130
Bibliography . . . . .		133

## FIGURES

- 2.1 (a) A schematic of the domain, (b) an instantaneous snapshot of the domain, where the open-channel flow is driven by a pressure gradient in the  $x$ -direction that generates shear-driven turbulence. Contours of velocity, temperature, and humidity are plotted with the presence of water droplets (black dots) interacting with turbulent temperature and humidity fields. The number of droplets is held constant by the re-injection mechanism. . . . . 20
- 2.2 A schematic example showing spray timescales in an  $x-z$  cross-section of the domain with an instantaneous contour of simulated air temperature. Three timescales listed near dashed lines are the residence time ( $t_L$ ), temperature response time ( $\tau_T$ ), and radius response time ( $\tau_r$ ). . . . . 26
- 2.3 Temperature and radius evolution of droplets at a quiescent environment, where the ambient temperature is 298.15 K, and the relative humidity is set constant as 90%. Dashed lines denote temperature change, and solid line denote radius change. . . . . 27
- 3.1 Overview of the mean flow quantities for the unladen and selected laden cases with  $\Phi_m = 10\%$ : (a) mean velocity of droplet phase (solid lines) and air phase (dashed line, which is equivalent to unladen flow); (b) horizontally averaged mass concentration,  $\Phi_m = m_w/m_a$ ; (c) mean relative humidity ( $RH$ ); (d) mean temperature. Angular brackets denote the horizontal averaging. . . . . 37
- 3.2 Time series evolution for 25  $\mu\text{m}$  (column 1 and 2) and 200  $\mu\text{m}$  (column 3) droplets for various quantities: vertical location (first row), particle temperature difference from ambient (second row), specific humidity difference (third row), and radius change from inception (fourth row). . . . . 39
- 3.3 Probability density functions (PDFs) of (a) normalised residence time ( $t_L$ ), where temperature time scales  $\tau_T$  for droplets are 0.0075 s (25  $\mu\text{m}$ ), 0.0670 s (75  $\mu\text{m}$ ), 0.4788 s (200  $\mu\text{m}$ ), (b) temperature difference (normalized by its initial temperature), and (c) radius difference (normalized by its initial radius) through their lifetime, compared with (d) time evolution of temperature and radius compared to their initial values during quiescent evaporation ( $T_f = 298.15$  K,  $T_{p,init} = 301.15$  K,  $RH = 90\%$ ). Three types of droplets are presented: small (25  $\mu\text{m}$ , red), medium (75  $\mu\text{m}$ , yellow), and large (200  $\mu\text{m}$ , blue) . . . . . 40

3.4	Normalized vertical heat fluxes for the 25 $\mu\text{m}$ case (brown) and unladen case (black): (a) Turbulent and particle heat fluxes, (b) diffusive and total heat fluxes. Components of heat flux are normalized by $u_*(h_{bot} - h_{top})$ , where $h_{bot}$ and $h_{top}$ are calculated based on Eq. 2.19 given the specific humidity and temperature, and $u_*$ is the friction velocity at lower boundary. (c) total heat flux extracted at the top of the spray layer versus particle radii. Asterisk indicates the unladen value. . . .	43
3.5	Sensible heat flux components versus droplet radius extracted at $z = \delta/8$ , compared with non-evaporative droplets (diamond), and unladen flow (blue asterisk). Components of heat flux are normalized by the total heat flux between two boundaries in z direction. (a) Total sensible heat flux $H_{s,total}$ , (b) turbulent component of sensible heat flux $H_{s,turb}$ , (c) particle direct sensible flux $H_{s,sp}$ . . . . .	44
3.6	Latent heat flux components versus droplet radius, compared with unladen flow (blue asterisk) at the top of ejection layer ( $z = \delta/8$ ). Components of heat flux are normalized by the total enthalpy difference between the two boundaries in the z direction. (a) Total latent heat flux $H_{L,total}$ , (b) turbulent component of latent heat flux $H_{L,turb}$ , (c) particle direct latent flux $H_{L,sp}$ . . . . .	46
3.7	Normalized total heat flux $H_T$ for a mass loading of $\Phi = 10\%$ for 25 $\mu\text{m}$ case (brown), 200 $\mu\text{m}$ case (blue) and unladen case (black). (a) (c) Turbulent and particle heat fluxes, and (b) (d) diffusive and total heat fluxes. Heat fluxes are normalized by the total enthalpy difference between the two boundaries in the z direction. . . . .	49
3.8	Sensible and latent heat fluxes at a height of $z = \delta/8$ versus droplet mass fraction $\Phi_m$ , compared with unladen flow (blue asterisk): (a) Total heat flux $H_T$ , (b) turbulent component of sensible heat flux $H_{s,turb}$ , (c) particle sensible flux $H_{s,sp}$ , (d) turbulent component of latent heat flux $H_{L,turb}$ , (e) particle latent flux $H_{L,sp}$ . Note: in (a) and (c), 75 $\mu\text{m}$ and 200 $\mu\text{m}$ have overlapped curves. . . . .	50
3.9	Normalized vertical heat flux for different boundary conditions. (a) Profiles of vertical heat flux for 25 $\mu\text{m}$ droplets. (b) Profiles of vertical heat flux for 200 $\mu\text{m}$ droplets. The colors are given in the legend. Here we combine the sensible and latent heat fluxes from same physical mechanism as one term, e.g. $H_{turb} = H_{s,turb} + H_{L,turb}$ , $H_{diff} = H_{s,diff} + H_{L,diff}$ , etc. Note: Lines not shown in the plot are overlapped with same terms for different BCs. . . . .	52
3.10	Selected normalized components of sensible and latent heat flux, $H_{s,turb}$ , $H_{s,sp}$ , $H_{L,turb}$ , and $H_{L,sp}$ , for the four boundary conditions given in Table 2.3 . . . . .	53
3.11	A schematic of the influences of large and small droplets on particle-induced enthalpy. . . . .	56

4.1	Estimated spray-mediated heat fluxes vs. DNS computed results: [a] spray-mediated sensible heat flux ( $H_{s,sp}$ vs. $\bar{Q}_s$ ), and [b] spray-mediated latent heat flux ( $H_{L,sp}$ vs. $\bar{Q}_L$ ). The product of the friction velocity ( $u_\tau$ ) and the vertical enthalpy difference of the domain ( $\Delta h$ ) is used to normalize heat fluxes. . . . .	60
4.2	DNS-computed spray-mediated total heat flux $H_{sp}$ vs. nominal sensible heat flux ( $\bar{Q}_s$ ), showing spray-mediated heat fluxes are reflected in its internal energy change. Heat fluxes are normalized by the product of the friction velocity ( $u_\tau$ ) and the vertical enthalpy difference of the domain ( $\Delta h$ ). Various simulations with different $Re_\tau$ , $\Phi_m$ , and size are denoted by color and marker in the legends. See Table 2.3 for simulation settings. . . . .	61
4.3	DNS-computed total heat flux ( $H_T$ ) versus the estimated total heat flux ( $H_{sp} + H_{int,0}$ ) by adding the DNS-computed spray-mediated flux with the corresponding unladen total interfacial heat flux. The heat fluxes are normalized by $u_\tau \Delta h$ . Color of symbols and marker styles in the legends match Fig. 4.2. . . . .	63
4.4	Modification of total interfacial heat flux ( $\Delta H_{int}$ ) versus nominal latent heat flux $\bar{Q}_L$ , showing that evaporation of spray induces a modification of the total interfacial heat flux. Color of symbols and marker styles in the legends match Fig. 4.2. . . . .	64
4.5	DNS-computed total heat flux ( $H_T$ ) versus the estimated total heat flux by Eq. (4.3) with a negative feedback term from the spray-mediated latent heat flux $\bar{Q}_L$ . Color of symbols and marker styles in the legends match Fig. 4.2. . . . .	66
4.6	Joint PDFs of residence time ( $t_L$ ) and droplet temperature change ( $\Delta T_p$ , left column) and radius change ( $r_p$ , right column) at $Re_\tau=1500$ . Three radii are presented: $25\mu\text{m}$ (first row), $75\mu\text{m}$ (second row), $200\mu\text{m}$ (third row). Color bars represents the density of the JPDFs in log-scale. . . . .	69
4.7	Conditional mean of temperature change ( $\Delta T_p$ [K]) and radius change ( $\Delta r_p$ [ $\mu\text{m}$ ]) given residence time ( $t_L$ [s]) for $75\text{-}\mu\text{m}$ spray droplets. Shaded areas represent possible solutions of stationary evaporation (grey for $\Delta T_p$ and green for $\Delta r_p$ ) with limits from two assumed constant ambient conditions (C1 and C2): (C1) $RH=97\%$ , $T_f=27.8^\circ\text{C}$ , and (C2) $RH=95.5\%$ , $T_f=27.4^\circ\text{C}$ . Also included are prediction using Eq. (4.5) for specifying representative ambient conditions: (P1) $RH=98.48\%$ , $T_f=27.35^\circ\text{C}$ , and (P2) $RH=96.19\%$ , $T_f=26.85^\circ\text{C}$ . . . . .	72

4.8	Conditional mean (expectation) and predictions of [a] temperature change ( $\Delta T_p$ [K]), and [b] radius change ( $\Delta r_p$ [ $\mu m$ ]) given residence time ( $t_L$ [s]) for 25- $\mu m$ spray droplets. The predictions (dashed lines) with equivalent ambient conditions are given by Eq. (4.5). The ambient conditions used for temperature are different from radius: (C1) & (P1) the quasi-equilibrium evaporation temperature of the spray at $RH=100\%$ , $T_f=28^\circ C$ , (C2) $RH=98\%$ , $T_f=28^\circ C$ , (C3) $RH=98\%$ , $T_f=27.8^\circ C$ , (C4) $RH=95\%$ , $T_f=27.4^\circ C$ , (P2) $RH=95.74\%$ , $T_f=26.35^\circ C$	76
4.9	Modification of total heat fluxes $H_T$ of different initial spray radii $r_p$ compared with no-spray scenario for each $Re_\tau$ with same boundary conditions indicated in Table 2.3. “M1” has $Re_\tau = 300$ , “R1” has $Re_\tau = 700$ , and “R2” has $Re_\tau = 1500$ , and markers specify the spray mass fraction. . . . .	79
4.10	Spray-mediated sensible ( $H_{s,sp}$ ) and latent ( $H_{L,sp}$ ) fluxes averaged in the spray layer $z \in [0, \delta_{inj}]$ . The heat fluxes are normalized by $u_\tau \Delta h$ . Colors specify the sensible or latent components, and line and marker styles are same as Fig. 4.9. . . . .	80
5.1	Instantaneous temperature and location of droplets (projection from $x$ -axis, i.e. the stream-wise direction). Mass fraction is here 5%, and half of droplets are plotted for a schematic. Color represents the droplet temperature, and the size of dots is scaled by the instantaneous droplet radius. . . . .	88
5.2	Normalized droplet mass concentration. For each curve, the total mass fraction $\Phi_m$ is same. Legends show the initial size of droplets ( $r_0$ ). . . . .	91
5.3	Air temperature ( $T_f$ ) and relative humidity ( $RH$ ) of different combinations of spray droplets. Solid lines represent the poly-dispersed cases, and dashed lines are the components from corresponding mono-dispersed cases. . . . .	95
5.4	Air temperature ( $T_f$ ) and specific humidity ( $q_f$ ) of different combinations of spray droplets. Solid lines represent the poly-dispersed cases, and dashed line is the superposition of corresponding mono-dispersed cases. . . . .	97
5.5	Modification of the total heat fluxes by droplets: bi-dispersed (solid lines) vs. mono-dispersed cases (dashed lines). . . . .	98
5.6	Sensible and latent spray-mediated heat fluxes, $H_{s,sp}$ (thin lines) and $H_{L,sp}$ (thick lines) respectively, of different combinations of spray droplets. Solid lines represent the poly-dispersed cases, and dashed line is the components from corresponding mono-dispersed cases. . . . .	99

5.7	Sensible and latent spray-mediated heat fluxes, $H_{s,sp}$ (thin lines) and $H_{L,sp}$ (thick lines) respectively, for different combinations of spray droplets. Solid lines represent the poly-dispersed cases, and dashed lines represent the superposition of corresponding mono-dispersed cases.	100
5.8	Sensible and latent turbulent heat fluxes, $H_{s,turb}$ (thin lines) and $H_{L,turb}$ (thick lines) respectively, for different combinations of spray droplets. Solid lines represent the poly-dispersed cases, and dashed line is the superposition of corresponding mono-dispersed cases to the unladen cases to the unladen case.	101
5.9	Mean error of heat fluxes between bi-dispersed cases and super-positioned cases. Negative errors indicate that the super-positioned value overestimates the corresponding DNS result.	104
5.10	$\Delta T_p$ and $\Delta r_p$ for bi-dispersed cases (markers) and mono-dispersed cases (lines). Three mass fraction are plotted: panel (a) and (d): $\Phi_m = 1\%$ ; panel (b) and (e): $\Phi_m = 5\%$ ; panel (c) and (f): $\Phi_m = 10\%$ .	105
5.11	Bulk estimation of $H_T$ vs. the DNS computed values. Markers filled in grey use the original expression shown in Eq. (4.3), and markers filled in green filter out the smaller size between the two sizes in a simulation.	108
5.12	(a) Number concentration distribution of the initial size ( $r_0$ ) for different SSGFs, and (b) Ratios of spray timescales given the initial size ( $r_0$ ). Note that the ratio between residence time ( $t_L$ ) and radius response time ( $\tau_r$ ) is much smaller than the ratio scaled by the temperature response time ( $\tau_T$ ).	111
5.13	Statistics of droplet temperature change ( $\Delta T_p$ ) and radius change ( $\Delta r_p$ ) as a function of initial droplet radius on different evaporation and two-way coupling conditions. In the left column, subplots (a) and (c) show the 2D-PDF for the ‘‘U-M’’ case (raw) under $\Phi_m = 5\%$ ; in the right column, subplots (b) and (d) show the mean of $\Delta T_p$ and $\Delta r_p$ for both ‘‘U-M’’ and ‘‘A98’’ SSGF under different $\Phi_m$ .	114
5.14	Spray-mediated heat fluxes: the ratio between the bulk estimates and DNS results as a function of initial droplet for the three mass fractions of the ‘UM’ SSGF ( $N_{r_0} = 35$ ). If the ratio between bulk-estimated value and DNS results is great than 1, it indicates the overestimation by the bulk models, and vice versa.	116
5.15	Spray-mediated heat fluxes: the ratio between the bulk estimates and DNS results for ‘UM’ (in green) and ‘A98’ (in yellow) ( $N_{r_0} = 35$ ). Different line styles indicates the evaporation and coupling conditions. Ratio $> 1$ indicates the overestimation by the bulk models, and vice versa.	117

5.16	Bulk estimation of $H_T$ vs. the DNS computed values for poly-dispersed cases. Markers filled in grey use the original expression shown in Eq. (4.3), and markers filled in green filter out the size smaller than $70\mu\text{m}$ in a simulation. A group of results considering $\beta = 0.9$ are also plotted as a comparison to the original expression. . . . .	119
5.17	The volume-weighted mean radius for three size ranges of the ‘UM’ SSGF, along with three representative sizes calculated for the ‘UM-medium’ case. . . . .	123
5.18	Air temperature ( $T_f$ , left) and relative humidity ( $RH$ , right) for the three representative cases and the ‘UM-medium’ case. . . . .	124
5.19	Comparisons of heat fluxes between the poly-dispersed cases and cases with the volume-weighted representative size ( $r_p=57\mu\text{m}$ ) for different boundary conditions listed in Table 2.3: (a) bottom and top boundaries have the same temperature (“M2”); and (b) inverse temperature difference (“M6”). . . . .	125
5.20	Sensible and latent spray-mediated heat fluxes (left), turbulent and total heat flux (right) for the three representative cases and the ‘UM-medium’ case. . . . .	126
5.21	Vertical mean profiles of (a) Air temperature ( $T_f$ ), (b) Sensible and latent spray-mediated heat fluxes, and (c) turbulent and total heat flux for $\langle r_p \rangle_3$ of the ‘UM-medium’ case and three ‘UM’ cases with different size distributions. . . . .	127

## TABLES

2.1	Simulation parameters . . . . .	14
2.2	Simulation grid setup under different $Re_\tau$ . . . . .	22
2.3	Boundary conditions of DNS simulations . . . . .	23
2.4	List of symbols for heat fluxes used in this study. . . . .	31
3.1	List of simulation groups . . . . .	35
4.1	Coefficients of bulk models and DNS-fit results . . . . .	67
5.1	Bi-dispersed cases . . . . .	94
5.2	Poly-dispered cases and their representative sizes . . . . .	122

## PREFACE

This dissertation study focuses on sea spray and its influences at the air-sea interface. While the spray droplets and their dynamics and thermodynamics are usually regarded as details to large-scale systems such as tropical cyclones, the consequences of different assumptions to these details could be significant.

Rather than replicating the real-world scenarios of spray transportation and evaporation at the air-sea surface, this dissertation aims at the inherent hypotheses in conventional meteorological models given a simplified but high-fidelity simulations of turbulent flows to investigate spray's influences and parameterization.

Three peer-reviewed journal articles based on this dissertation are published ( [Peng and Richter \(2017\)](#) for Ch. [3](#), and [Peng and Richter \(2019\)](#) for Ch. [4](#)) or in prep (Ch. [5](#)) at the time the dissertation was submitted at the being of the chapters. Updated contents may be present in the ETD record of the University Notre Dame via Curate ND (<https://curate.nd.edu>).

## ACKNOWLEDGMENTS

This dissertation study would not have been possible without help and support from a great number of individuals. As my advisor for the doctoral program and the director of the Dissertation Committee, Dr. David H. Richter impressed me with his passion and dedication to science and research, and it is his guidance that made this rewarding journey. Also, I am grateful to all members of the Dissertation Committee: Dr. Bolster, Dr. Crippa, and Dr. Fernando. They have not only provided me with suggestions and comments to the current study but also mentored me with personal and professional guidance.

Besides, I received constant support and help from colleagues at the Department of Civil and Environmental Engineering and Earth Sciences. To name a few, I am grateful for the constructive feedback and help from Brian Helgans, Indrajith Nisanka, H. John Park, Elise Wright, Zachary Hanson, Thomas Sherman, Kyuhyun Byun, Guiquan Wang, and Theodore MacMillan to this dissertation.

Moreover, I would like to express my gratitude to my family who live on the other side of the earth and have been unconditionally encouraging me for my studies at Notre Dame. I would not have completed this journey without their continued patience and endless love.

This dissertation study is supported by the National Science Foundation (NSF) grant AGS-1429921. I would like to acknowledge high-performance computing support from the Computing Research Center at the University of Notre Dame and Yellowstone/Cheyenne (UNDM0004) maintained by the Computational Information Systems Laboratory at the National Center for Atmospheric Research (NCAR).

NCAR is supported by the NSF.

## CHAPTER 1

### INTRODUCTION

#### 1.1 A mismatch of scales

Modeling the dynamics in the earth systems requires an enormous amount of computational resources. In modern meteorological applications such as numerical weather prediction suites, the dynamics of the atmosphere and other earth systems are calculated via software modules discretely in space and time. Each module has its solvers for a specific physical system, and solvers of these systems are also coupled with others to capture the interactions between each system. In general, the spatial resolution of a weather prediction model ranges from mesoscale at  $O(10 \text{ km})$  to  $O(100 \text{ km})$  to even a larger system (e.g., synoptic scale at  $O(1000 \text{ km})$ ), and nesting and local refinements of the mesh bring the spatial scale down to  $O(1 \text{ km})$  in the region of interests such as the interfaces of land-atmosphere or ocean-atmosphere systems (Park et al., 2014).

However, mismatch of scales occurs between smaller-scale physical processes and numerical weather models. These small-scale processes have characteristic scales ranging from the micro-scale at  $O(1 \text{ km})$  down to the Kolmogorov scale at  $O(1 \text{ cm})$ , and such processes include the cloud in the atmospheric boundary layer, wave breaking at the ocean surface, and turbulent transport near the complex territory. That is to say, the influences of smaller-scale processes have to be parameterized by other resolved meteorological parameters, which brings challenges to represent these small-scale processes in large-scale simulations.

One example showing the challenges could be the research for the energy transfer at the lower boundary of tropical cyclones (TCs). A tropical cyclone is defined as a cyclone originated from the ocean surface, and it is one of the most spectacular and lethal extreme weather events (Emanuel (2003)). It is generally believed that the a TC is fueled by the energy transferred from the ocean (Emanuel, 2003; Nolan, 2007) and that the air-sea exchange is a deterministic effect of hurricane intensity (Andreas et al., 2015; Lee and Chen, 2012; Montgomery et al., 2010). Meanwhile, in a cyclone model (e.g., (Lee and Chen, 2012)), the multinested grid size ranges from  $O(10)$ km to  $O(1)$ km. Therefore, how air-sea processes are parameterized will affect the accuracy in quantifying air-sea exchange in the numerical meteorological forecasts over the ocean. This kind of mismatch of scales motivates studies on various air-sea processes and their parameterizations.

## 1.2 Physical processes at the air-sea interface and sea spray

The air-sea interface (ASI) consists of the first few meters of ocean and the lower marine atmospheric boundary layer (MABL). On the atmospheric side, the MABL consists of multiple layers. Right above the ocean surface for a few millimeters, it is a molecular-diffusion layer, where the molecular diffusion dominates the transport processes. Beyond the diffusion layer to 10-100 m above the ocean surface, turbulence dominates the vertical transport, which is also called surface layer (Garbe et al., 2014).

Physical processes at the ASI are complex, including a series of events such as turbulence in multiple scales at both sides of the interface, waves and wave breaking, surface film, bubbles, and spray. In particular, these processes become more intense and chaotic under high winds, so they certainly play specific roles in the air-sea exchange of momentum, heat, moisture, and mass, although the degree to which they mediate air-sea transfer remains in question.

While complex processes occur at the air-sea interface, when evaluating the tur-

bulent transport at this region, the ocean surface is usually assumed as a flat surface with explicit parameterizations of these air-sea processes added on the flat-surface turbulent transport. For example, the turbulence in the lower MABL is assumed homogeneous and in an equilibrium condition. Hence, the vertical profile of the surface layer can be described by the Monin-Obukhov Similarity Theory (MOST) given a neutral atmosphere stratification (Stull, 1988), and the vertical transfer within the surface layer can be approximated by constant flux. In addition, the gradient transport hypothesis indicates that the constant surface fluxes in the surface layer are purely driven by the differences of the exchanged variables (e.g. wind speed, temperature, and humidity) between a reference height (subscript ‘ $z$ ’) and the sea surface (subscript ‘ $0$ ’) with the efficiency of the air-sea exchange represented by the transfer coefficients. Thus, one could write the surface fluxes of momentum ( $\tau$ ), sensible heat ( $H$ ), and moisture ( $E$ ) in a bulk form that is used in virtually all numerical weather prediction models as:

$$\tau = \rho_a u_\tau^2 = \rho_a C_D (U_z - U_0)^2, \quad (1.1)$$

$$H = \rho_a c_p \overline{w'\theta'} = \rho_a c_p C_K U_z (\theta_z - \theta_0), \quad (1.2)$$

and

$$E = \rho_a \overline{w'q'} = \rho_a C_E U_z (q_z - q_0), \quad (1.3)$$

where  $C_D$ ,  $C_K$ , and  $C_E$  are the bulk transfer coefficients. Thus, if all the meteorological parameters (e.g.,  $U_z$ ,  $\theta_z$ , and etc.) in Eqs. 1.1 to 1.3 can be fetched via observations or numerical models, one could evaluate the surface fluxes by retrieving the gradients of temperature and humidity. Therefore, the transfer coefficients play the deterministic role in evaluating air-sea surface fluxes.

However, difficulties exist in quantifying the air-sea transfer coefficients. First, these coefficients are not necessarily independent from the wind speed (Andreas and

(Mahrt, 2015; Bell et al., 2012), indicating wind-induced physical processes may play roles that are implicitly reflected in these coefficients. Second, transfer coefficients of different fluxes may have different dependence on wind speed, which adds complexity in understanding these processes. For example, from retrievals of the absolute angular momentum and total energy budget during the 2003 Coupled Boundary Layers Air-Sea Transfer (CBLAST) campaign (Bell et al., 2012), it shows  $C_K$  has an increasing trend with the average 10-m wind velocity while  $C_D$  has a decreasing trend, and  $C_K/C_D$  drastically increases wind speed exceeds  $60 \text{ m s}^{-1}$ . Therefore, explicitly quantifying the near-surface physical processes and their influences modifying the surface fluxes are necessary for developing air-sea exchange parameterizations.

Among common air-sea processes, ocean spray is one of the most visible phenomena at air-sea interface or lower MABL. The spray is generated from ocean surface by two main pathways: 1) bubble-burst after air being entrained in the water column by breaking waves (film and jet drops) and 2) surface wave torn off by strong winds (spume drops) (Veron (2015)). These spray droplets somewhat function like an additional continuum phase at lower MABL but also has its own characteristics which are separated from air flows. Hence, the distinctive characteristics of spray have been indeed challenging many observational and numerical studies in finding the potential influence of sea spray on air-sea fluxes.

One ordinary argument regarding spray's influence is the increased surface area of water in the atmosphere under hurricane strength winds (Hasse, 1992). For example, the ratio surface area of a spray droplet to its value is scaled as  $\frac{3}{r_p}$ , which indicates 1% of volume fraction of droplets with radius at  $10 \text{ }\mu\text{m}$  would result in about 3.3 times increase of the surface area of water droplets compared to the ocean surface area. Thus, based on this argument, one example question is whether or not  $C_E$  or  $C_K$  would grow with the increased surface area due to spray, which motivates a series of studies to quantify the influence of sea spray droplets.

### 1.3 Previous efforts in quantifying spray’s influences in the air-sea heat fluxes

In the past decades, there is a large volume of studies in quantifying and characterizing the complex physics associated with sea spray at the MABL. Nevertheless, the degree to which spray mediates air-sea transfer and the basic coupling mechanisms between the air and spray remain in elusive despite its potential impacts on meteorological forecasting (Andreas and Emanuel, 2001; Soloviev et al., 2014; Wang et al., 2001). As noted by Kepert et al. (1999) and others, two fundamental issues need to be solved in order to fully quantify the effects of spray: (i) the generation mechanisms of spray (i.e. constraining the source function); and (ii) the feedback mechanism by which spray droplets modify the the the local turbulent environment. These issues persist due to the inherent complexity of the system and difficulties in direct observations. The topic of this dissertation covers the latter of the two challenges, in particular, the thermodynamic feedback of spray on latent and sensible heat fluxes.

When the spray is present, the total (sensible and latent) heat transported from the sea to the air consists of two routes: interfacial fluxes and spray-mediated fluxes (Andreas, 1992). It is commonly assumed that these two independent components can be summed to produce the total heat flux, or that if one could estimate the interfacial component, the overall spray effects could be measured via the change of the total. In other words, the total heat fluxes can be written as

$$H_T = H_{s,int} + Q_s + H_{L,int} + Q_L, \quad (1.4)$$

where  $Q_s$  and  $Q_L$  are the sensible and latent heat fluxes mediated by spray, and  $H_{s,int}$ ,  $H_{L,int}$  are the corresponding interfacial fluxes. Given Eq. 1.4, one could evaluate the

transfer coefficient associated with the total heat flux in Eq. 1.2 can be written as

$$C_K = \frac{H_{s,int} + H_{L,int} + Q_s + Q_L}{\rho_a c_p U_z (\theta_z - \theta_0)}. \quad (1.5)$$

Thus, quantifying each term in Eq. 1.5 gives a  $C_K$  that is utilized in a large-scale meteorological model with spray effects considered.

In practice, however, decoupling the two routes, or measuring one in the absence of the other, is not trivial and involves significant approximation. Relatively few experimental or observational studies exist that even attempt to measure the total heat fluxes in high winds, and these are generally based on indirect measurements (Bell et al., 2012; Richter and Stern, 2014; Wang and Street, 1978), lab experiments (Jeong et al., 2012; Komori et al., 2018), or direct eddy covariance measurements (Drennan et al., 2007; Zhang et al., 2008). In these studies, it is challenging to address the role that sea spray plays conclusively. Also, it remains nearly impossible to distinguish between the interfacial and spray-mediated routes or provide the necessary detail for assessing whether or not the total heat flux can be decomposed in this way.

When developing models to account for the effects of the spray, one must consider both the droplet microphysics as well as the feedback effect of spray onto the surrounding flow. There are two directions where modeling studies focus on. The first type of study focuses on the effects of spray on specific meteorological events, such as spray's influences on the intensity of tropical cyclones. Usually, these studies apply the parameterizations of spray on momentum, heat, and mass transfer occurred in the lower marine atmospheric boundary layer (MABL) to the system and generalize the sensitivities of the objective meteorological events or variables to the sea spray (e.g., Andreas and Emanuel (2001); Bao et al. (2011); Fairall et al. (1994); Liu et al. (2011)). Another type of studies focuses on the parameterizations of spray's effects, given simplifications and assumptions on flow conditions. Based on the two direc-

tions of spray studies, the numerous numerical/theoretical spray models that exist can be categorized into three major groups: bulk algorithms, Eulerian multiphase approaches (or one-dimensional models), and Lagrangian approaches.

In general, bulk parametrizations are used as a standard tool for estimating the sensitivity of surface fluxes in large-scale weather and climate model to the spray, rather than being used as a tool to investigate spray’s influences. The models usually attempt to estimate the net air-sea fluxes without resolving the corresponding vertical profiles in the atmosphere nor the details of spray’s dynamics and thermodynamics (Andreas et al., 2015; Bao et al., 2011; Fairall et al., 1994; Mestayer and Lefauconnier, 1988). Hence, bulk models are associated with two common hypotheses: (i) contributions from individual sea-spray droplets are independent and can directly add to the interfacial heat fluxes, and (ii) the sensible and latent heat released from sea spray can be determined from the difference between the initial and final temperature and size of the droplets, neglecting all intermediate dynamics.

However, the question of whether or not these are reasonable assumptions has not been addressed, which could be the reason for continued discrepancies between measurements and theory. For example, by parametrizing the “spray-mediated” and “interfacial” routes of heat fluxes, the recent study of Andreas et al. (2015), based on earlier work (Andreas, 1990, 1992, 1995), provides an improved bulk air-sea flux algorithm to that in Andreas (2005). The study finds that the spray route of the air-sea scalar transfer becomes a significant fraction of the total at modest wind speed, and that the spray-mediated sensible and latent heat fluxes overcome the interfacial fluxes at  $19 \text{ m s}^{-1}$  and  $26 \text{ m s}^{-1}$  respectively. In contrast to the bulk model, the results from observations (DeCosmo et al., 1996; Drennan et al., 2007; Zhang et al., 2008) and certain experiments (Jeong et al., 2012) indicate a lack of dependence of the heat and moisture transfer coefficients  $C_K$  and  $C_E$  on wind speed. Other experimental data, however, show that there may be a significant increase in the

transfer coefficients due possibly to spray (Komori et al., 2018; Troitskaya et al., 2018a,b). These disagreements emphasize the necessity of understanding the details of air-spray turbulent coupling, and the difficulties associated with formulating bulk models and making detailed measurements.

The other two modeling approaches (Eulerian-multiphase and Lagrangian) have increased complexity, attempting to account for the vertical transport of the droplets as they interact with the air flow. When sea spray is treated as an additional continuum phase along with turbulent airflow, it can be modeled in an Eulerian framework, where spray's concentration, velocity, temperature, and mass are computed in same domain as the turbulent air as a separate phase (e.g., Rastigejev and Suslov (2019, 2016)). Meanwhile, the vertical transport of momentum, heat, and moisture in the atmosphere are modeled via turbulence closure schemes. Thus, the coupling of spray droplets with the air flow is included in the model as horizontally-homogeneous sources/sinks of the air, and in principle, these models can capture the effects of elevated spray sources on the vertical profiles of air temperature and humidity. For example, Rastigejev and Suslov (2019) found the difference between small droplets and large droplets in modifying the total heat flux and vertical profiles of the air temperature, and the modification of heat fluxes heavily depends on the spray concentration. However, how to properly parameterize the statistics of spray droplets within a grid remains unclear in particular when droplets are dilute and inertial, e.g., the transport of inertial droplet (e.g., concentration) in turbulence. Thus, the assumptions behind calculating the spray source/sinks on energy and moisture require careful investigation and are nearly impossible to measure directly.

An alternative approach is to estimate the accumulated impact of spray by tracking droplets individually (Edson and Fairall, 1994; Edson et al., 1996; Mueller and Veron, 2010, 2014a,b; Troitskaya et al., 2018a,b). This method is referred as Lagrangian method. For example, Edson and Fairall (1994) designed a Lagrangian

model to investigate the turbulent transport of evaporating droplets based on stochastically generated ambient MABL conditions. The model is then extended in [Edson et al. \(1996\)](#) by adding the interaction of droplets with the turbulence field as represented by a two-dimensional  $k - \epsilon$  model. The results show a substantial increase in latent heat flux along with a significant decrease in sensible heat flux for droplets released at the significant wave height. [Mueller and Veron \(2014a,b\)](#) put forward a Lagrangian stochastic model with more sophisticated and accurate droplet physics ([Mueller and Veron, 2010](#)) and an updated source function ([Veron et al., 2012](#)). The results predict that the total enthalpy coefficient quickly increases as wind speed exceeds  $20 \text{ m s}^{-1}$  (here the enthalpy flux is defined as the sum of the sensible and latent heat fluxes). Similarly, [Troitskaya et al. \(2018b\)](#) also reported a noticeable increase in the total heat flux and attributed the effect to the giant droplets. However, in typical Lagrangian stochastic models, a trade-off exists in deciding whether to treat the background flow in a simple manner (e.g. one-dimensional MO theory) or attempting to resolve the turbulence explicitly. And in the former, assumptions must again be made in treating the two-way coupling of heat and moisture between the spray and air phases.

With advances in computational capacity in the last decade, high-resolution Eulerian-Lagrangian simulations have been emerging, which is the method that best reflects the unique characteristics of sea spray droplets in turbulent air flows and resolves the physics of both air turbulence and droplets. Thus, the Eulerian-Lagrangian method directly reveals the underlying physics behind droplet-flow interaction, particularly in regards to heat and moisture fluxes when the droplets are evaporating. This kind of numerical methods had been successfully applied in the engineering context (e.g., [Bukhvostova et al. \(2014\)](#); [Russo et al. \(2014\)](#) for particle-laden Turbulent channel flow, [Helgans and Richter \(2016\)](#); [Richter and Sullivan \(2014\)](#) for the Couette flow), and it is the main investigation method used in this dissertation to better

understand surface fluxes and transport within the spray-laden MABL.

Although the high-resolution simulations implementing the framework of Eulerian-Lagrangian DNS is not designed to reproduce the real system, it is an ideal tool to reveal the details of the microphysics of spray droplets and small-scale turbulence and sensitivities of the heat fluxes to sea spray in an explicit way. In addition, this framework can also be used to assess other models (e.g., bulk models) regarding its assumptions made for spray parameterizations, which bridge the updated understandings of the spray droplets without further complications of the existing models.

#### 1.4 Objectives and structures of the dissertation

In this dissertation, with the guidance of Dr. David Richter, we design a set of numerical experiments in turbulent open-channel flow with direct numerical simulation (DNS), where Lagrangian droplets of a specified concentration are thermodynamically coupled to the surrounding flow. The primary goal of the study is to use high-resolution simulations to assist in the interpretation of existing theories and measurements related to spray feedback to the air-sea heat fluxes. We examine the fundamental influence of evaporating droplets on the heat fluxes and compare results between other spray models in an idealized and isolated setting, despite many other factors including wave breaking and droplet formation still require attention and are not considered in this dissertation.

Following the introduction in this chapter, Ch. [2](#) covers the methodology of direct numerical simulations (DNS) implementing the Eulerian-Lagrangian method for idealized droplet-laden open-channel flows used throughout the dissertation along with its numerical implementation. Three following chapters focus on the research questions that motivate the numerical experiments discussed in this dissertation.

To investigate the fundamental sensitivity of the turbulent air flows and heat fluxes to spray droplets, Ch. [3](#) discusses how spray droplets modify the sensible

and latent heat fluxes and background air temperature and humidity. A series of numerical control experiments are reported in this chapter to investigate specific relationships between heat fluxes and spray properties such as droplet size, mass concentration, and time constants of spray droplets. The following research questions are answered in this chapter: How do spray droplets modify the turbulent and total sensible heat fluxes? What are the most important parameters for modeling spray's effects on surface heat fluxes?

Ch. 4 continues to utilize the DNS framework and connect the physical-resolving DNS simulations with bulk air-sea models for spray's influence on the total heat flux. Three scientific questions are discussed in this chapter: Can the spray-mediated heat flux be directly added to the interfacial heat flux? How significant is the feedback effect of spray droplets? How can one specify effective atmospheric conditions in a simplified bulk model?

To bring more reality to the idealized DNS study, Ch. 5 revisits some fundamental questions answered in Ch. 3 with a series of spray sizes considered simultaneously (poly-dispersed) in the numerical experiments. This chapter is designed to assess another fundamental assumption in most existing spray models for the independence of spray's contribution from different size. Three scientific questions are discussed in Ch. 5 include: Does individual spray droplet have the same effects on the heat fluxes given a poly-dispersed condition comparing with the mono-dispersed case? Is there a representative spray size for droplets following a size distribution? Can bulk models still apply given the poly-dispersed DNS results?

The dissertation will be concluded in Chapter 6 with the contributions and limitations of the study in this dissertation discussed in this chapter. Suggestions for future development toward the topics that this dissertation covers are also discussed.

## CHAPTER 2

### METHODOLOGY

#### 2.1 Overview

This chapter covers the main methodology in this dissertation. First, the fundamental investigation method of the thesis – the Eulerian-Lagrangian direct numerical simulations (DNS) for evaporating spray droplets will be introduced. The following section will introduce the microphysics and characteristics of spray evaporation discussed in later chapters. In addition, the sampling method of droplet statistics and bulk algorithms of spray heat fluxes are also introduced in this chapter.

#### 2.2 The Eulerian-Lagrangian algorithm

One goal of this dissertation is to understand the thermodynamic behavior of droplets in a turbulent boundary-layer flow from both a per-droplet and statistical perspective. Here, the solver used in this study combines the advantages of several of the aforementioned Eulerian-Lagrangian algorithm and implement direct numerical simulations (DNS) to simulate the air (‘carrier’) and droplet (‘dispersed’) phases simultaneously. All scales of turbulent motion in the air phase are resolved with DNS, and no turbulence modeling is required. At the same time, we also individually track and compute the trajectory, temperature, and size of individual water droplets throughout the domain. This section will begin with the governing equations of the carrier phase and dispersed droplets and then introduce the configuration of our numerical experiments.

## 2.2.1 Governing equations

### 2.2.1.1 Carrier phase

To represent idealized shear-driven turbulence at the ASI, we simulate turbulent open-channel flow driven by a pressure gradient with various boundary conditions. We further assume (1) incompressible flow; (2) neutral stability for the carrier phase; and (3) a flat surface at the lower boundary. Thus, this system is meant to focus on the physics underlying turbulence-droplet coupling and is not meant to replicate a real air-sea interface. We also assume, due to the limited variation in temperature, that material properties such as viscosity and thermal diffusivity are constant and independent of temperature and humidity.

With the assumptions stated above, the governing equations of mass, momentum, temperature, and humidity for the air are given by

$$\frac{\partial u_i}{\partial x_i} = 0, \quad (2.1)$$

where  $u_i$  is the velocity of the air at location  $x_i$ ,

$$\frac{\partial u_i}{\partial t} + u_j \frac{\partial u_i}{\partial x_j} = -\frac{1}{\rho_a} \frac{\partial P}{\partial x_i} + \nu_a \frac{\partial^2 u_i}{\partial x_j \partial x_j}, \quad (2.2)$$

where  $P$  is the pressure,  $\rho_a$  is the air density, and  $\nu_a$  is the kinematic viscosity of air (see Table [2.1](#) for parameter values),

$$\frac{\partial T}{\partial t} + u_j \frac{\partial T}{\partial x_j} = \alpha \frac{\partial^2 T}{\partial x_j \partial x_j} + \frac{1}{\rho_a} S^h, \quad (2.3)$$

where the specific heat of air  $c_{p,a}$  and thermal diffusivity  $\alpha = \kappa_T / (\rho_a c_{p,a})$  are assumed constant ( $\kappa_T$  is the thermal conductivity of air) and  $S^h$  is the heat source due to

TABLE 2.1

## SIMULATION PARAMETERS

Parameters	Symbols	Values
Friction Reynolds number	$Re_\tau$	300
Schmidt number	$Sc$	0.615
Prandtl number	$Pr$	0.71
Density of air	$\rho_a$	1.1 kg m <sup>-3</sup>
Density of water	$\rho_w$	1000 kg m <sup>-3</sup>
Kinematic viscosity of air	$\nu_a$	$1.537 \times 10^{-5} \text{m}^2 \text{s}^{-1}$
Specific heat of air	$c_{p,a}$	1006 J K <sup>-1</sup> kg <sup>-1</sup>
Specific heat of water vapor	$c_{p,v}$	1952 J K <sup>-1</sup> kg <sup>-1</sup>
Latent heat of evaporation	$L_v$	$2.44 \times 10^6 \text{J kg}^{-1}$
Molecular weight of water	$M_w$	0.018 kg mol <sup>-1</sup>
Molecular weight of salt	$M_s$	0.0584 kg mol <sup>-1</sup>
Vertical height of domain	$\delta$	0.04 m

droplets. Also,

$$\frac{\partial q}{\partial t} + u_j \frac{\partial q}{\partial x_j} = D_v \frac{\partial^2 q}{\partial x_j \partial x_j} + \frac{1}{\rho_a} S^q, \quad (2.4)$$

where the diffusivity of vapor  $D_v$  is also assumed constant, the specific humidity  $q$  is defined as the ratio of local vapor density to dry air density  $q = \rho_v/\rho_a$ , and the source  $S^q$  is the droplet source of humidity.

### 2.2.1.2 Dispersed phase

We employ the point-particle approach based on the fact that the diameters of most droplets near the air-sea interface are smaller than the Kolmogorov length scale  $\eta_K$  which is the smallest scale in a turbulent flow. Therefore, droplets are modeled as infinitesimal points exhibiting their own velocity, temperature, and radius. Under the point-particle approximation, we introduce the following Lagrangian equations governing the location, velocity, temperature, and radius of each particle based on conservation of mass, momentum, and energy.

The diameters of most droplets near the air-sea interface are smaller than the Kolmogorov length scale  $\eta_K$ , the smallest scale in the turbulent flow. Therefore we employ the point-particle approach, which represents droplets as infinitesimal points exhibiting their own velocity, temperature, and radius. Under the point-particle approximation, we introduce the Lagrangian equations governing the location, velocity, temperature, and radius of each particle based on the conservation of mass, momentum, and energy. The evolution of a droplet's location is computed via its velocity

$$\frac{dx_{p,i}}{dt} = v_{p,i} \quad (2.5)$$

where  $x_{p,i}$  is the location of a particle (this does not necessarily coincide with the grid used to solve the air-phase equations), and  $v_{p,i}$  is the velocity of an individual droplet. The droplet velocity is governed by momentum conservation assuming Stokes drag with a small Reynolds number correction (Clift et al., 1978)

$$\frac{dv_{p,i}}{dt} = (1 + 0.15Re_p^{0.687}) \frac{1}{\tau_p} (v_{f,i} - v_{p,i}) - g_z \delta_{i3}, \quad (2.6)$$

where the particle Reynolds number is defined as  $Re_p = d_p |v_{f,i} - v_{p,i}| / \nu_a$ , and  $\tau_p = \rho_p d_p^2 / (18\nu_a \rho_a)$  is the acceleration time scale of the particle, which is a function of the droplet diameter  $d_p$  and droplet density  $\rho_p$ . The term  $g_z$  is the magnitude of

acceleration due to gravity in the  $z$ -direction. Equation 2.6 indicates that a particle is accelerated both by hydrodynamic drag and gravity. The former is based on the difference of the particle velocity and the local fluid velocity  $v_{f,i}$ , and  $v_{f,i}$  must be interpolated to the particle location from the velocity  $u_i$  in Eq. 2.2 at the surrounding grid points.

The thermodynamic evolution of a droplet includes both mass and temperature changes. The microphysical model used to describe droplet evaporation is based on Andreas (1992), Andreas et al. (1995), Pruppacher and Klett (1996), and Mueller and Veron (2010). A full description can be found in Helgans and Richter (2016).

We have the following equations for the mass ( $m_p$ ) and radius ( $r_p$ ) of a spherical droplet,

$$\frac{dm_p}{dt} = 4\pi r_p^2 \rho_w \frac{dr_p}{dt}, \quad (2.7)$$

$$\frac{dr_p}{dt} = \bar{h}_m \frac{\rho_a}{\rho_w} (q_f - q_p), \quad (2.8)$$

where  $\rho_w$  is the density of pure water. The term  $\bar{h}_m$  is the convective mass transfer coefficient of evaporative droplets

$$\bar{h}_m = \frac{1}{9} \frac{Sh_p \rho_p r_p}{Sc \rho_a \tau_p}, \quad (2.9)$$

where  $Sh$  is the Sherwood number  $Sh = 2 + 0.6Re_p^{1/2} Sc^{1/3}$  (Ranz and Marshall, 1952), and  $Sc = \nu_a/D_v$  is the Schmidt number that relates the viscosity and vapor diffusivity (the values are given in Table 2.1.)

Equation 2.8 shows that the change in particle mass (radius) is dependent on the difference between the local air humidity  $q_f$  (interpolated from the grid) and the humidity near the droplet surface  $q_p$ . The value of  $q_p$  is based on the saturation vapor pressure at the droplet temperature  $T_p$ , the surface curvature, and the droplet

salinity. The detailed expression can be found in [Helgans and Richter \(2016\)](#), and is the same as that used in [Mueller and Veron \(2010\)](#).

Energy conservation governs the temperature of the droplet, which we assume uniform throughout its interior. Temperature evolution is based on the air-droplet sensible and latent heat transfer exchange rates  $\dot{Q}_{conv}$  and  $\dot{Q}_{latent}$ , the former being driven by the difference between the droplet temperature  $T_p$  and the surrounding air temperature  $T_f$ . The latter is associated with evaporation/condensation

$$\begin{aligned} \frac{dT_p}{dt} &= \frac{1}{\rho_w V_d c_L} \left[ \dot{Q}_{conv} + \dot{Q}_{latent} \right] \\ &= \left[ -\frac{1}{3} \frac{Nu_p}{Pr} \frac{c_{p,a}}{c_L} \frac{\rho_p}{\rho_w} \frac{1}{\tau_p} (T_p - T_f) \right] + \left[ 3L_v \frac{1}{r_p c_L} \frac{dr_p}{dt} \right], \end{aligned} \quad (2.10)$$

where  $V_d$  is the volume of the spherical water droplet,  $\rho_p$  is the bulk density of the saline droplet (nearly equal to the pure water density  $\rho_w$ ),  $c_L$  is the specific heat of liquid water (assumed constant), and  $L_v$  is the latent heat of evaporation. Sensible heat transfer between the droplet and surrounding air is treated as a convective process with a heat transfer coefficient given in non-dimensional form by an empirical relation for the Nusselt number ([Ranz and Marshall, 1952](#)):  $Nu_p = 2 + 0.6 Re_p^{1/2} Pr^{1/3}$ . Here,  $Pr = \nu_a / \alpha = 0.71$  is the Prandtl number of air, which is the ratio of the viscosity and thermal diffusivity.

### 2.2.1.3 Two-way coupling

A key feature of the current model is that it captures two-way coupling between the droplets and air simultaneously — a process that nearly all past Lagrangian studies lack ([Edson and Fairall, 1994](#); [Edson et al., 1996](#); [Mueller and Veron, 2014a,b](#)). The momentum-coupling is not considered in this study and is isolated from the formulation to specifically focus on the thermodynamic coupling in a turbulent flow. In fact, reported by [Richter and Sullivan \(2014\)](#), the influence of momentum coupling

from inertial particles on the total momentum flux in a shear-driven turbulent flow is nearly negligible due to the compensating effect between increased particle stress and near-wall vortical activity. Therefore, throughout the study in this dissertation, we remove the air-droplet momentum exchange for simplicity.

The two-way exchange of heat and moisture is found in the terms  $S^h$  and  $S^q$  in Eqs. 2.3 and 2.4. These source terms are computed at a grid node as the summation of weighted contribution from all particles that reside in the eight surrounding computational grid volumes. Detailed expressions of  $S^h$  and  $S^q$  are given in the following equations. For the latent heat (vapor moisture) coupling term  $S^q$  is calculated by summing all nearby droplets on one Eulerian grid, i.e.,

$$S^q = - \sum_{i=1}^{N_p} \frac{w_i}{\Delta V} \left( \frac{\dot{m}_p}{\rho_a} \right)_i, \quad (2.11)$$

where  $i$  represents the index for an individual droplet,  $N_p$  is the total particle number,  $w_i$  represents the weight of droplets based on the distance of the droplets to nearby grid points,  $\dot{m} = \frac{dm_p}{dt}$  are the exchange rate of droplets and calculated based on Eq. 2.7. The coupling term for the sensible heat  $S^h$  has two components: one from heat convection and another from evaporation, so that

$$S^h = S^{h,conv} + S^{h,evap}, \quad (2.12)$$

where details of  $S^{h,conv}$  and  $S^{h,evap}$  are listed in the following equations:

$$S^{h,conv} = - \sum_{i=1}^{N_p} \frac{w_i}{\Delta V} (\dot{Q}_{conv})_i, \quad (2.13)$$

and

$$S_{h,evap} = - \sum_{i=1}^{N_p} \frac{w_i}{\Delta V} (\dot{m}_p (c_{p,v} T_f - c_{p,v} T_p))_i \quad (2.14)$$

## 2.2.2 Numerical set-up

### 2.2.2.1 Simulation domain

The underlying code is succeed from previous studies (Helgans and Richter, 2016; Richter, 2015; Richter and Sullivan, 2014) for solving Eqs. 2.1 – 2.10. The solver for the carrier phase uses a pseudospectral spatial discretization with anti-aliasing in the periodic streamwise ( $x$ ) and spanwise ( $y$ ) directions, and uses a second-order finite difference method in the wall-normal ( $z$ ) direction. Incompressibility is enforced by solving a pressure Poisson equation, while time integration is performed with a low-storage third-order Runge-Kutta method (Spalart et al., 1991) for both phases.

The domain is set up to simulate pressure-driven, turbulent open-channel flow over a flat plate. The domain has dimensions of  $[2\pi\delta, 2\pi\delta, \delta]$  using a corresponding grid of  $[128, 256, 128]$  grid points, where  $\delta = 0.04$  m. The friction Reynolds number  $Re_\tau = u_*\delta/\nu = 300$  throughout, where the friction velocity  $u_* = \sqrt{\tau_w/\rho_a}$  is defined using the total stress  $\tau_w$  at the bottom boundary. All simulations are initialized with a previously obtained particle-free turbulent flow field. A no-slip condition at the bottom surface and a no-stress (full-slip) condition at the top surface are enforced for the air velocity. The air temperature and humidity are specified at both the top and bottom boundaries, where the baseline condition is such that the top boundary is cooler and drier ( $T_{top} = 25^\circ\text{C}$ ,  $RH_{top} = 90\%$ , where  $RH$  is the relative humidity) while the lower boundary is warmer and saturated ( $T_{bot} = 28^\circ\text{C}$ ,  $RH_{bot} = 100\%$ ), in order to represent a turbulent boundary layer over a smooth water surface. See Fig. 2.1a for a schematic, and Fig. 2.1b for an instantaneous temperature and humidity distribution.

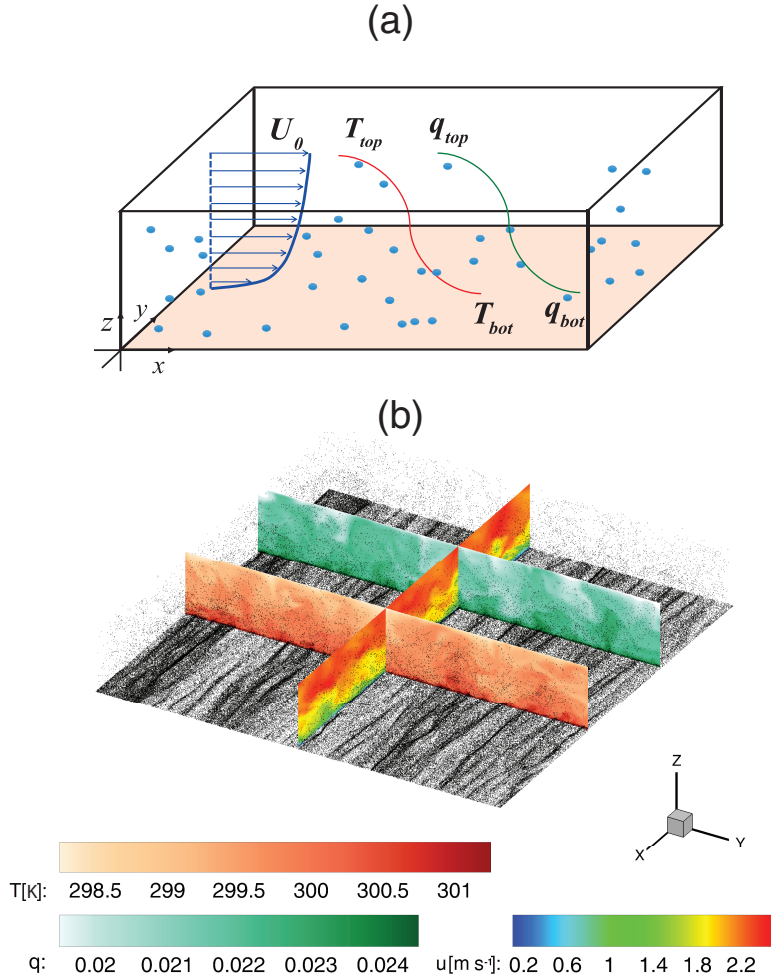


Figure 2.1. (a) A schematic of the domain, (b) an instantaneous snapshot of the domain, where the open-channel flow is driven by a pressure gradient in the  $x$ -direction that generates shear-driven turbulence. Contours of velocity, temperature, and humidity are plotted with the presence of water droplets (black dots) interacting with turbulent temperature and humidity fields. The number of droplets is held constant by the re-injection mechanism.

### 2.2.2.2 Boundary and initial conditions

The current study, rather than replicating a real system, aims to use DNS to test whether or not the parameterizations of spray properly capture the complex physics. Thus, we design the following boundary and initial conditions to fulfill the goals.

The system is initialized with a fully developed, horizontally-homogeneous turbulent flow field with a random distribution of spray droplets in the domain. At the top boundary, droplets reflect elastically in order to keep them contained within the computational domain (this is equivalent to a no-flux condition), and since particles undergo gravitational settling, they are removed from the system when they fall beneath the bottom surface. We maintain a constant loading of droplets by re-injecting a droplet for the ones that are removed. The new droplets are introduced at a random location across the bottom surface and given a random initial velocity chosen from a uniform distribution between zero and the velocity that would allow the droplet to reach a maximum height of  $\delta_{inj}$  defined in Table. [2.2](#) in quiescent conditions. This process mimics a high-concentration “spray-layer” near the bottom surface, and is sufficiently deep such that turbulence can entrain droplets from within this layer and transport them throughout the domain. Particles above a height of  $z = \delta/8$  have necessarily been carried there by turbulent motions.

As the turbulence develops, we obtain a statistically steady droplet production flux, which gives a steady mean  $F$  (e.g.,  $F$  ranges from  $8 \times 10^3 \text{ s}^{-1}$  to  $5 \times 10^6 \text{ s}^{-1}$  for various spray sizes when  $Re_\tau = 300$ ), and we get a steady mean number concentrations above  $\delta_{inj}$  ranging from  $3.176 \times 10^7 \text{ m}^{-3}$  for  $20 \mu\text{m}$  droplets to  $152.6 \text{ m}^{-3}$  for  $200 \mu\text{m}$  droplets.

Finally, we note several important considerations regarding the dimensional quantities used. Since DNS cannot be used to simulate the true MABL, our goal here is to match as many essential non-dimensional quantities as possible. For instance, the baseline Reynolds number of  $Re_\tau = 300$ , while necessarily low to resolve all scales

TABLE 2.2

SIMULATION GRID SETUP UNDER DIFFERENT  $Re_\tau$ 

$Re_\tau$	$N_x$	$N_y$	$N_z$	$g_z$ [m s <sup>-2</sup> ]	$\delta$ [m]	$\delta_{inj}$ [mm]
300	128	256	128	0.8027	0.04	5.000
700	256	512	256	1.0302	0.08	4.286
1500	512	1024	512	1.1398	0.16	4.008

Note:  $(N_x, N_y, N_z)$  represent grid numbers in  $(x, y, z)$  directions,  $g_z$  is the gravity scaled for the DNS,  $\delta$  is the dimensional height of the domain, and  $\delta_{inj}$  is the maximum height that droplets with initial velocity can reach.

of motion, is sufficiently high to provide insight into the consequences of turbulent suspension and thermodynamic coupling between droplets and air. We also considered and tested another two different values of  $Re_\tau$  (700 and 1500) to ensure that the results from the baseline DNS are robust with varying turbulence intensities.

### 2.2.2.3 Selection of other droplet parameters

Other quantities, such as the gravitational acceleration  $g_z$ , are chosen to provide the same non-dimensional quantities as found in the true MABL. To ensure that the droplets settle with the same tendency relative to turbulence intensity,  $g_z$  is chosen such that the non-dimensional settling velocity  $w_s/w'$ , where  $w'$  is the root-mean-square of the vertical velocity fluctuations (on the order of 1 m s<sup>-1</sup> in the atmosphere) and  $w_s = \tau_p g_z$  is the terminal velocity of droplets (on the order of 1 m s<sup>-1</sup> for a 100  $\mu$ m droplet in quiescent air, see [Veron \(2015\)](#)), is the same as that outside. Thus, we set  $g_z = 0.84$  m s<sup>-2</sup> in the present simulations.

Within the broad spectrum of spray droplet and aerosol sizes, which ranges from

TABLE 2.3

## BOUNDARY CONDITIONS OF DNS SIMULATIONS

BC Groups	$T_{bot}$ [K]	$T_{top}$ [K]	$RH_{bot}$	$RH_{top}$	$\Phi_w = m_w/m_a$	$Re_\tau$
M1	301.15	298.15	100%	90%	1%, 5%, 10%	300
M2	301.15	301.15	100%	90%	5%	300
M3	301.15	298.15	100%	100%	5%	300
M4	301.15	296.15	100%	90%	5%	300
M5	301.15	298.15	100%	80%	5%	300
M6	298.15	301.15	100%	100%	5%	300
M7	304.15	301.15	100%	90%	5%	300
R1	301.15	298.15	100%	90%	1%	700
R2	301.15	298.15	100%	90%	1%	1500

Note:  $T_{bot}$  and  $T_{top}$  represent the temperature at bottom and top boundaries,  $RH_{bot}$  and  $RH_{top}$  represent relative humidities at two boundaries,  $r_{p,0}$  represents the initial spray size,  $\Phi_w$  represents the spray mass ratio to the air, and  $Re_\tau$  represents friction Reynolds number of the domain.

sub-micron to several millimeters (see e.g. [de Leeuw et al. \(2011\)](#) or [Veron \(2015\)](#)), the radii listed above fall in the range of medium to large. Therefore references to “small”, “medium”, and “large” herein refer to the relative size of droplets within the upper portions of the full spectrum. Previous studies ([Mueller and Veron, 2014a](#); [Richter and Sullivan, 2014](#)) indicate that the dynamics and thermodynamics of spray are related to its size and its ability to change size and temperature. Droplets (e.g. spume droplets) in this range not only occur at the peak of the volume spectra at high wind speeds ([Fairall et al., 2009](#)), but also dominate the heat and mass transfer. According to spray-mediated flux models ([Andreas, 1992](#); [Andreas et al., 2008, 2015](#)), the peaks of sensible and latent heat fluxes at high wind speed are located near  $r_p \approx 50 \mu\text{m}$  and  $100 \mu\text{m}$  respectively.

For the non-dimensional perspective, the droplet sizes and densities are chosen to match the dimensionless Stokes numbers of real spray droplets,  $St = \tau_p/\tau_K$ , where  $\tau_K$  is the vertically-averaged Kolmogorov time scale of the flow.  $St$  indicates on how rapidly the droplet adjusts to the local air velocity. The present simulations are configured so that the Kolmogorov time scale in the simulations roughly matches that of the true MABL (2 ms is selected as a reference value while  $\tau_K$  ranges from 0.2 ms to 6.5 s ([Thorpe, 2005](#))). Therefore the droplet sizes and density are chosen to match those of realistic spray as well ( $\rho_p = 1000 \text{ kg m}^{-3}$ , with  $r_p$  ranging between  $25 \mu\text{m}$  and  $200 \mu\text{m}$ ). Therefore, the selection of droplets in this dissertation covers the range that most significantly influences heat and mass transfer.

#### 2.2.2.4 Droplet size and size distributions

Considering one size in a simulation is an idealized scenario, but it provides a unique perspective for isolating the influence from a specific size from others. In practice, spray is generated with a wide range of size, and the generation of spray is related to wind speed and other parameters at the air-sea interface.

When there is only one size of droplets, we refer it as a mono-dispersed case, which is discussed in Ch. 3 and 4. Otherwise, cases with multiple sizes are referred to as poly-dispersed cases, which is discussed in Ch. 5. Details of configurations on droplet size will be discussed these chapters.

### 2.2.3 Timescales of evaporating spray droplets

Three types of timescales are associated with moving droplets that are evaporating in a turbulent field. First, the residence time,  $t_L$ , that is determined by both spray droplets and turbulent intensity, denotes the duration between the generation of a droplet and the moment droplets deposit to the ocean surface. Second, the droplet temperature response time,  $\tau_T$ , which is governed by Eq. (2.10), shows how fast temperature is exchanged with the ambient air by spray droplets. Third, the droplet radius response time, which is associated with the evaporation, is governed by Eqs. (2.8) and (2.10). Figure 2.2 shows a schematic example for these three timescales. There are discussions on the definition and theoretical expressions of these three timescales (e.g. Andreas (1992, 2005); Holterman (2003); Lewis and Schwartz (2004)), and in this dissertation, we adopted a simple expression from these studies to illustrate the microphysics associated with spray droplets.

For the residence time ( $t_L$ ), the DNS solver is designed to count the time for each spray droplets. For the two thermodynamic timescales ( $\tau_T$  and  $\tau_r$ ), based on Eqs. (2.10) and (2.8) and given a common range of temperature (288.15K to 330.15K) and relative humidity (70% to 100%), the numerical results of Eqs. (2.10) and (2.8) shows the temperature and radius evolution of a droplet during evaporation can be characterized by different time scale for each equation. An example of theoretical solutions of droplet evaporation in a quiescent environment is plotted in Fig. 2.3.

From the figure, it is clear that droplets change temperature first before a significant change in their radius due to evaporation. To characterize the speed and

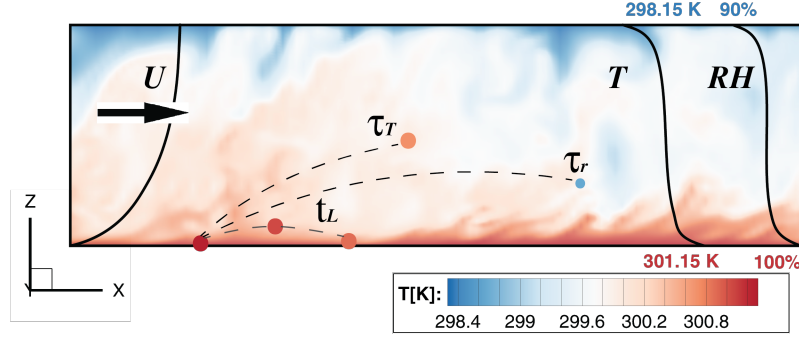


Figure 2.2. A schematic example showing spray timescales in an  $x - z$  cross-section of the domain with an instantaneous contour of simulated air temperature. Three timescales listed near dashed lines are the residence time ( $t_L$ ), temperature response time ( $\tau_T$ ), and radius response time ( $\tau_r$ ).

extent of the evaporation of droplets, two time constants of droplet evaporation is defined,  $\tau_T$  and  $\tau_r$ , where subscript ‘ $T$ ’ stands for temperature change and ‘ $r$ ’ for radius change.

In Eq. 2.10, it is clear that in an early stage, the radius changes in a slow rate, so that latent term containing  $\frac{dr_p}{dt}$  is much smaller than the convective term. If one neglects the evaporation term, given a initial radius  $r_p$ , temperature of droplets changes in an exponential way (cf. Andreas (2005)). Thus, as mentioned in Andreas (1990),  $\tau_T$  can be defined as the  $e$ -folding time for a droplet reaching its equilibrium temperature ( $T_{eq}$ ) from its initial temperature ( $T_{p,init}$ ), i.e.,

$$\frac{T_p(t) - T_{eq}}{T_{p,init} - T_{eq}} = \exp\left(-\frac{t}{\tau_T}\right). \quad (2.15)$$

To derive a detailed expression of  $\tau_T$ , we follow the dimensional analysis by Mueller and Veron (2010) ( $\tau_T$  was called  $\tau_{SH}$  there) to get the following estimation of  $\tau_T$  in our simulation,

$$\tau_T = C_T \frac{Pr}{Nu_p} \frac{c_L}{c_{p,a}} \frac{\rho_w}{\rho_p} \tau_p \propto r_p^2, \quad (2.16)$$

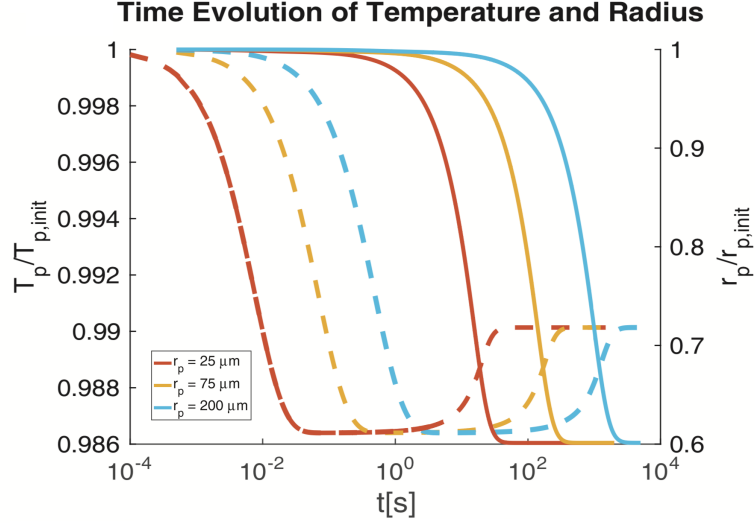


Figure 2.3. Temperature and radius evolution of droplets at a quiescent environment, where the ambient temperature is 298.15 K, and the relative humidity is set constant as 90%. Dashed lines denote temperature change, and solid line denote radius change.

where  $C_T$  is the scaling constant, and  $\tau_p$  is the Stokes relaxation time, which is proportional to  $r_p^2$ . Other terms are defined in the previous section. To combine the self-similar results from Eq. (2.16) with the definition by Andreas (1990), we define  $C_T = 1$ .

The definition of the characteristics timescale of droplet radius evolution is less conclusive among different studies. One common area that nearly all spray studies agree is that  $\tau_r$  is approximately  $O(10^3)$  larger than  $\tau_T$  (also cf. Richter et al. (2016a); Veron (2015)). Despite variant expressions of  $\tau_r$  and the fact that  $r_p$  is not necessarily scaled exponentially with time, we analyzed the theoretical solution shown in Fig. 2.3 and adopted a self-similar definition of  $\tau_r$  as its  $e$ -folding time too,

$$\frac{r_p(t) - r_{eq}}{r_{p,init} - r_{eq}} = \exp\left(-\frac{t}{\tau_r}\right), \quad (2.17)$$

where the evolution of  $r_{eq}$  is the equilibrium radius for droplets with the initial radius

$r_{p,init}$ .

Therefore,  $\tau_r$  can be estimated from  $\tau_T$  as

$$\tau_r = C_r \tau_T, \quad (2.18)$$

where  $C_r$  are scaling constants, and we fit  $C_r = 760$  based on the solution shown in Fig. 2.3.

#### 2.2.4 Heat fluxes partitioning

Heat fluxes quantify the energy transfer across the boundary layer. The components of sensible and latent heat fluxes from DNS discussed in this dissertation are defined in a similar way as Richter and Sullivan (2014) and Helgans and Richter (2016). First, define a total moist enthalpy as being the enthalpy contained by both the vapor and air phases, i.e.,

$$h_{gas} = \rho_a c_{p,a} T + \rho_a q (c_{p,v} T + h_v^0). \quad (2.19)$$

Then, with Eqs. 2.3 and 2.4, an equation for total enthalpy can be established (see Helgans and Richter (2016) for the full expression). Using this expression, we apply a Reynolds decomposition on the temperature  $T$ , moisture  $q$ , and velocity  $u_i$  of the air phase, and then average the equation horizontally. This procedure yields a total moist enthalpy flux in the vertical direction that has the form

$$H_T = H_{s,total} + H_{L,total} = \text{constant}, \quad (2.20)$$

where  $H_{s,total}$  and  $H_{L,total}$  are individually decomposed into three components representing the turbulent, diffusive, and particle-induced flux of enthalpy

$$\begin{aligned} H_{s,total} &= H_{s,turb} + H_{s,diff} + H_{s,sp} \\ &= \rho_a c_{p,a} \langle w'T' \rangle - \rho_a c_{p,a} \alpha \frac{d\langle T \rangle}{dz} - \int_0^z S^h dz, \end{aligned} \quad (2.21)$$

and

$$\begin{aligned} H_{L,total} &= H_{L,turb} + H_{L,diff} + H_{L,sp} \\ &= (c_{p,v} + h_v^0) \left[ \langle w'q' \rangle - \rho_a D_v \frac{d\langle q \rangle}{dz} - \int_0^z S^q dz \right]. \end{aligned} \quad (2.22)$$

We define positive fluxes upwards. Also, the cross-coupling terms between latent (we define here as terms with subscript “ $q$ ”) and sensible (subscript “ $a$ ”) terms are negligible and are therefore not included in the above equations (cf. [Helgans and Richter \(2016\)](#)).

### 2.3 Bulk parameterizations for spray-mediated heat fluxes

In the last section of this chapter, we introduce the method of bulk air-sea models of spray effects. This method will be assessed in Ch. [4](#) and [5](#).

#### 2.3.1 Heat fluxes in a bulk model

The fundamental framework of a bulk model is to assume the total heat flux is the direct sum of interfacial and spray-mediated components. To start with, we follow the two bulk models and define the total heat flux  $H_T$  that consists of the interfacial (subscript ‘ $int$ ’) and spray-mediated (subscript ‘ $sp$ ’) components. Each term can be further decomposed into their latent (subscript ‘ $L$ ’) and sensible (subscript ‘ $s$ ’)

components, i.e.,

$$H_T = H_{int} + H_{sp} = H_{L,sp} + H_{L,int} + H_{s,sp} + H_{s,int}, \quad (2.23)$$

and we list the descriptions for each term in Table 2.1. Thus, the estimation process for the total flux requires accurate quantification of all four components in Eq. 2.23 at the air-sea interface. For example, the sensible and latent interfacial heat fluxes can be estimated based on gradient-wind transfer laws of the (potential) temperature and specific humidity (Andreas and Emanuel, 2001; Andreas et al., 2015), which is commonly used among bulk models. However, parameterizing the spray-mediated sensible and latent heat fluxes varies across different bulk models because of different assumptions associated with the spray microphysics.

### 2.3.2 Estimates of spray-mediated heat fluxes

Specifically, the two common bulk models considered in this study, Fairall et al. (1994) (herein “F94”) and Andreas et al. (2015) (herein “A15”), estimate spray evaporation differently. F94 assumes that the temperature change will be the only effect that contributes to the total spray-mediated heat flux, i.e.,

$$H_{sp}^{<F94>} = \bar{Q}_s, \quad (2.24)$$

and

$$H_{L,sp}^{<F94>} = \bar{Q}_L, \quad (2.25)$$

so that

$$H_{s,sp}^{<F94>} = \bar{Q}_s - \bar{Q}_L. \quad (2.26)$$

Here in Eqs. 2.24 – 2.26,  $\bar{Q}_s$  and  $\bar{Q}_L$  respectively represent the nominal spray-mediated sensible and latent exchange rates — that is, the rate of net exchange of

TABLE 2.4

LIST OF SYMBOLS FOR HEAT FLUXES USED IN THIS STUDY.

Variables	Description
$H_T$	Total heat flux computed by DNS
$H_{s,sp}$	Sensible spray-mediated heat flux computed by DNS
$H_{L,sp}$	Latent spray-mediated heat flux computed by DNS
$H_{s,int}$	Sensible interfacial heat flux computed by DNS
$H_{L,int}$	Latent interfacial heat flux computed by DNS
$\bar{Q}_s^{<A15>}$ or $\bar{Q}_s^{<F94>}$	Bulk sensible spray-mediated heat exchanging rate (the nominal flux) with the model specified by the superscript (e.g., “A15” or “F94”)
$\bar{Q}_L^{<A15>}$ or $\bar{Q}_L^{<F94>}$	Bulk latent spray-mediated heat exchanging rate (the nominal flux) with the model specified by its superscript (e.g., “A15” or “F94”).
$\bar{Q}_s$	Estimates of sensible spray-mediated heat exchanging rate (the nominal flux) via Eq. (2.30) with inputs from DNS
$\bar{Q}_L$	Estimates of latent spray-mediated heat exchanging rate (the nominal flux) via Eq. (2.31) with inputs from DNS
$\Delta H_{int}$	The change of the total interfacial heat flux of spray-laden DNS simulations from the unladen simulations
$\Delta H_T$	The change of the total heat flux of spray-laden DNS simulations from the unladen simulations

sensible and latent heat by the droplets between entering and leaving the ocean.

Meanwhile, A15 assumes some degree of compensation due to evaporative cooling, i.e.,

$$H_{L,sp}^{<A15>} = \alpha \bar{Q}_L, \quad (2.27)$$

and

$$H_{s,sp}^{<A15>} = \beta \bar{Q}_s - (\alpha - \gamma) \bar{Q}_L, \quad (2.28)$$

where the fitting coefficients  $\alpha$ ,  $\beta$ , and  $\gamma$  are determined by observational data given assumptions on  $\bar{Q}_s$  and  $\bar{Q}_L$ . However, A15 explicitly assumes an increase of sensible heat components induced by spray evaporation, so  $0 < \gamma < \alpha$  represents the adjustment of interfacial heat fluxes due to the cooling effect of spray evaporation. Therefore, the total spray-mediated heat flux described by A15 is

$$H_{sp}^{<A15>} = \beta \bar{Q}_s + \gamma \bar{Q}_L. \quad (2.29)$$

Comparing Eq. [2.29](#) with Eq. [2.24](#), one notices the equivalent coefficients  $(\alpha, \beta, \gamma) = (1, 1, 0)$  in F94 model, while in A15 the three coefficients are given as  $(\alpha, \beta, \gamma) = (2.46, 15.15, 1.77)$ . Obviously, the difference in the magnitude of coefficients in the two models could eventually lead to very different influences of spray droplets predicted by the bulk models.

One of the factors that contributes to the discrepancy between the two models is the assumed form of the spray sensible and latent heat exchange rates or the nominal fluxes  $\bar{Q}_s$  and  $\bar{Q}_L$ . Written in generic terms, these take the form:

$$\bar{Q}_s = -c_p m_{p,0} \Delta T_p \frac{F}{A}, \quad (2.30)$$

and

$$\bar{Q}_L = -L_v \Delta m_p \frac{F}{A}, \quad (2.31)$$

where  $\Delta T_p$  and  $\Delta m_p$  are the mean net difference of spray temperature and radius, respectively, between the initial and final condition when entering the water surface.  $F$  is a spray renewal rate at the surface (related to the spray generation function), and  $A$  is the horizontal area of interest. Therefore, both  $\bar{Q}_s$  and  $\bar{Q}_L$  have units of [energy area<sup>-1</sup> time<sup>-1</sup>].

In F94, spray is assumed to enter the surface with a temperature equal to the air temperature at the significant wave height ( $T_f$ ), after beginning with a temperature equal to the sea surface temperature ( $T_s$ ). Thus  $\Delta T_p = T_a - T_s$ , which implies an instantaneous temperature adjustment of the spray. On the other hand, A15 assumes that the difference  $T_a - T_s$  is the maximum potential temperature difference, and  $\Delta T_p$  is limited by its residence time (“ $\tau_f$ ” in the original text of A15 and “ $t_L$ ” in this paper), so that for each size of spray  $\Delta T_p = (T_s - T_a)[1 - \exp(-\frac{t_L}{\tau_T})]$ , where  $\tau_T$  is the thermal response time of spray defined by Eq. (1.4) in [Andreas \(2005\)](#) as the  $e$ -folding time of temperature evolution given steady ambient condition.

Similarly for spray evaporation, for the spray’s mass change ( $\Delta m_p$ ), F94 assumes an instantaneous evaporative adjustment to the conditions at the significant wave height, while A15 considers the temporal evolution due to a evaporation timescale ( $\tau_r$ , also defined as an  $e$ -folding time in [Andreas \(2005\)](#)) which is much longer than  $\tau_T$ . Using the DNS, we can calculate directly the quantities  $\Delta T_p$  and  $\Delta m_p$ , and therefore compare to the assumed forms of A15 and F94.

## CHAPTER 3

### INFLUENCE OF EVAPORATING DROPLETS IN THE LOWER MARINE ATMOSPHERIC BOUNDARY LAYER

#### 3.1 Overview

To overcome some of the limitations of the bulk or Eulerian models, in particular the difficulty of including spray feedback on the surrounding flow, we use the model described in Ch. 2. In this section, a set of numerical experiments are designed in turbulent open-channel flow with direct numerical simulation (DNS) to examine the fundamental influence of evaporating droplets on the heat fluxes in an idealized and isolated setting. The goal of this chapter is to provide a detailed investigation to the sensitivity of heat fluxes due to spray droplets, so that one could use the results to assist in the interpretation of existing theories and measurements related to spray feedback in the MABL.

Based on the methodology discussed above, we conduct three sets of numerical experiments (see Table 2.1) focusing primarily on the influence of droplet radius on overall vertical sensible and latent heat transfer (group A); additional tests are chosen to probe the sensitivity of these results to mass loading (group B) and boundary conditions (group C). Here we define the mass loading as the ratio of the mass of water and mass of air in the domain ( $\Phi_m = m_w/m_a$ ). In this section, we compare horizontally- and time-averaged quantities (e.g., heat fluxes) with respect to droplet-free flow, and use droplet lifetime statistics to comment on the behavior of droplets.

TABLE 3.1

## LIST OF SIMULATION GROUPS

Group	$r_p$	$\Phi_m$	$T_{top}$ [K]	$T_{bot}$ [K]	$RH_{top}$ (%)	$RH_{bot}$ (%)
A	varied	1%	298.15	301.15	90	100
B	fixed	varied	298.15	301.15	90	100
C	fixed	1%	systematically varied			

## 3.2 Results and discussion

## 3.2.1 Influence of droplet size

Our overall interest lies in the thermodynamic influence of droplets on mean vertical energy transfer in a turbulent boundary-layer flow. In this context, previous studies (Andreas, 1990, 1992, 1995) have provided an extensive theoretical description of droplet dynamics and thermodynamics, which have indicated that droplet size is an important quantity since it controls the droplet lifetime, inertia, settling velocity, and the time scales associated with heat transfer and evaporation. We therefore construct the first group of simulations to investigate the role of droplet size on heat-flux modification by choosing six different radii: 25  $\mu\text{m}$ , 50  $\mu\text{m}$ , 75  $\mu\text{m}$ , 100  $\mu\text{m}$ , 150  $\mu\text{m}$ , and 200  $\mu\text{m}$ . The selection of radii gives thermodynamic time scales  $\tau_T$  ranging between 7.5 ms (25  $\mu\text{m}$ ) and 478.8 ms (200  $\mu\text{m}$ ). All other parameters are set based on Table 2.1.

An overview of key mean flow quantities is given in Fig. 3.1, where it is clear that droplets can have a significantly different mean velocity than the surrounding flow at a given height. The smallest droplets (here 25- $\mu\text{m}$  radius) behave somewhat like fluid tracers, while the largest droplets (200- $\mu\text{m}$  radius) have little correspondence to

the ambient flow. This is particularly clear in Fig. 3.1b, where small droplets spread evenly throughout the upper domain, while large droplets, due to their high inertia and settling velocity, remain near the bottom. Figures 3.1c, d show that despite two-way coupling in humidity and temperature, at a mass fraction of  $\Phi_m = 1\%$  only a slight change in the average fields is found for all droplet radii compared to the unladen field. If anything, large droplets slightly increase the air temperature while small droplets decrease the temperature, a feature qualitatively consistent with other studies of spray thermodynamic effects (e.g. Bianco et al. (2011)).

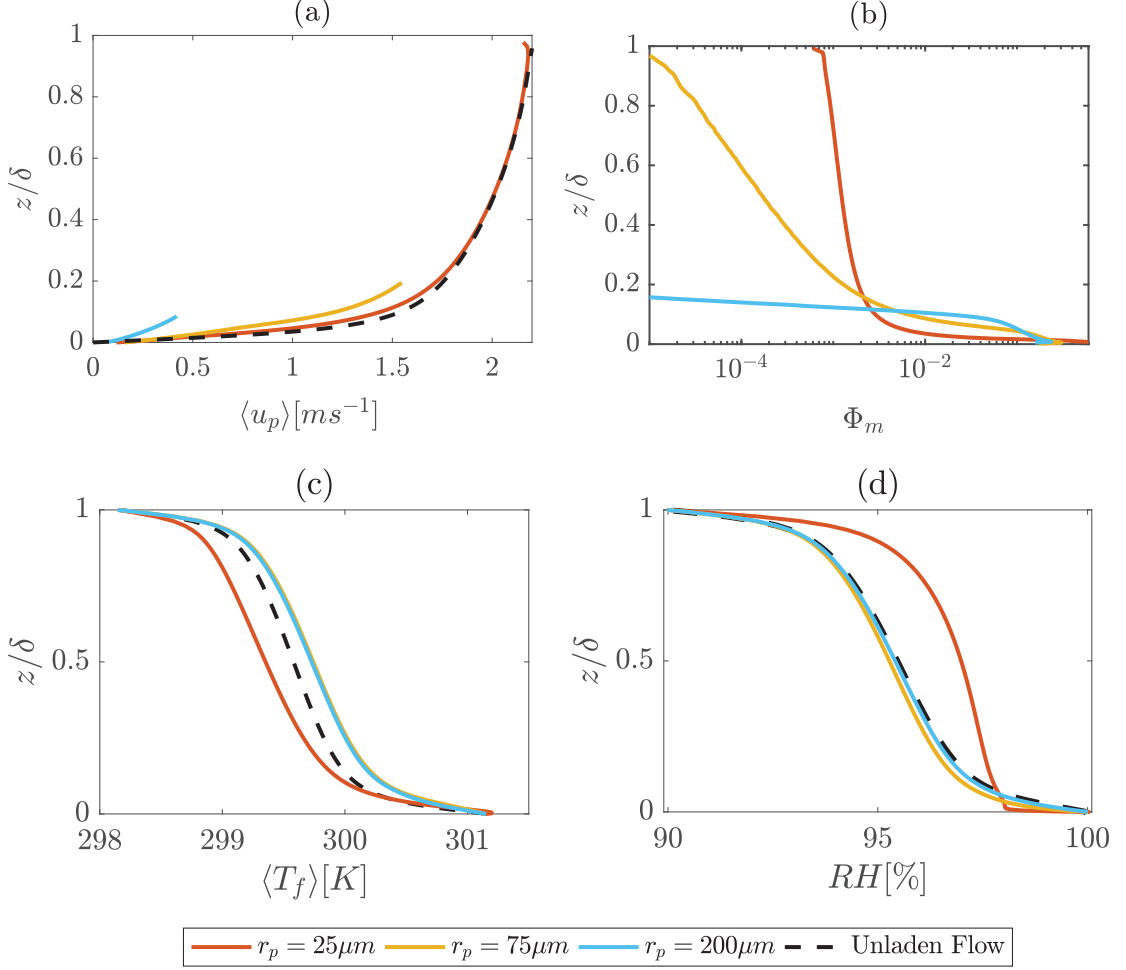


Figure 3.1. Overview of the mean flow quantities for the unladen and selected laden cases with  $\Phi_m = 10\%$ : (a) mean velocity of droplet phase (solid lines) and air phase (dashed line, which is equivalent to unladen flow); (b) horizontally averaged mass concentration,  $\Phi_m = m_w/m_a$ ; (c) mean relative humidity ( $RH$ ); (d) mean temperature. Angular brackets denote the horizontal averaging.

### 3.2.1.1 Behaviors of droplets in the turbulence

Since the droplets are evaporating, it is important to understand their thermodynamic evolution as well. To do this, we compare the dynamic and thermodynamic

evolution of representative  $25\ \mu\text{m}$  and  $200\ \mu\text{m}$  droplets in Fig. 3.2. Two scenarios are considered: one where the droplet has escaped the lower regions of the flow (this only occurs for the smaller droplet) and one where the droplet has a much shorter lifetime because it is transported immediately downwards after injection.

In the first of these two scenarios (first column), droplets experience evaporative cooling as they almost continuously find themselves cooler than their environment (second row). Additionally, droplets experience a vapour pressure deficit at the surface (third row) and thus evaporate with a 2% radius decrease (fourth row). However, other small droplets are transported back into the lower boundary and slightly condense and warm in their short lifetime, which leads to the next scenario.

In the second scenario (second and third columns), droplets are immediately removed but due to different mechanisms: gravitational settling for large droplets and turbulent advection for small droplets. Small droplets (second column), travelling within a very limited vertical distance where local humidity is high, find themselves warmer than their surroundings due to condensation in their brief lifetime. Larger droplets, on the other hand, have a longer thermodynamic response time; therefore a lag exists in their radius change. The droplets start to evaporate because the larger inertia keeps the droplets moving further, and the droplets experience a wider range of temperature and humidity differences with the surroundings. For this scenario, we note that both small and large droplets have the potential to slightly warm the ambient air (as droplets are warmer than air). This has been seen in, e.g., Edson et al. (1996), for the release of sensible heat from droplets at high relative humidity. In Bianco et al. (2011), it is also mentioned that large droplets have the potential to warm the surrounding air due to their long thermodynamic characteristic time.

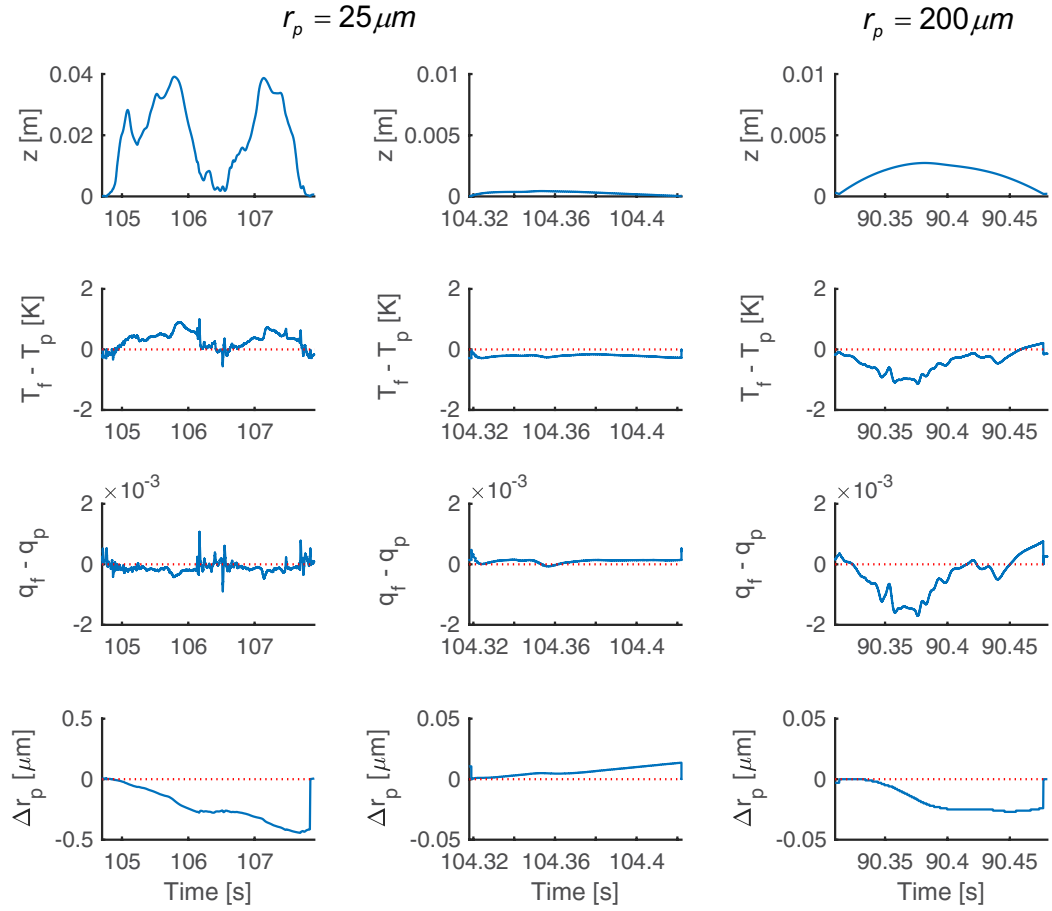


Figure 3.2. Time series evolution for  $25 \mu\text{m}$  (column 1 and 2) and  $200 \mu\text{m}$  (column 3) droplets for various quantities: vertical location (first row), particle temperature difference from ambient (second row), specific humidity difference (third row), and radius change from inception (fourth row).

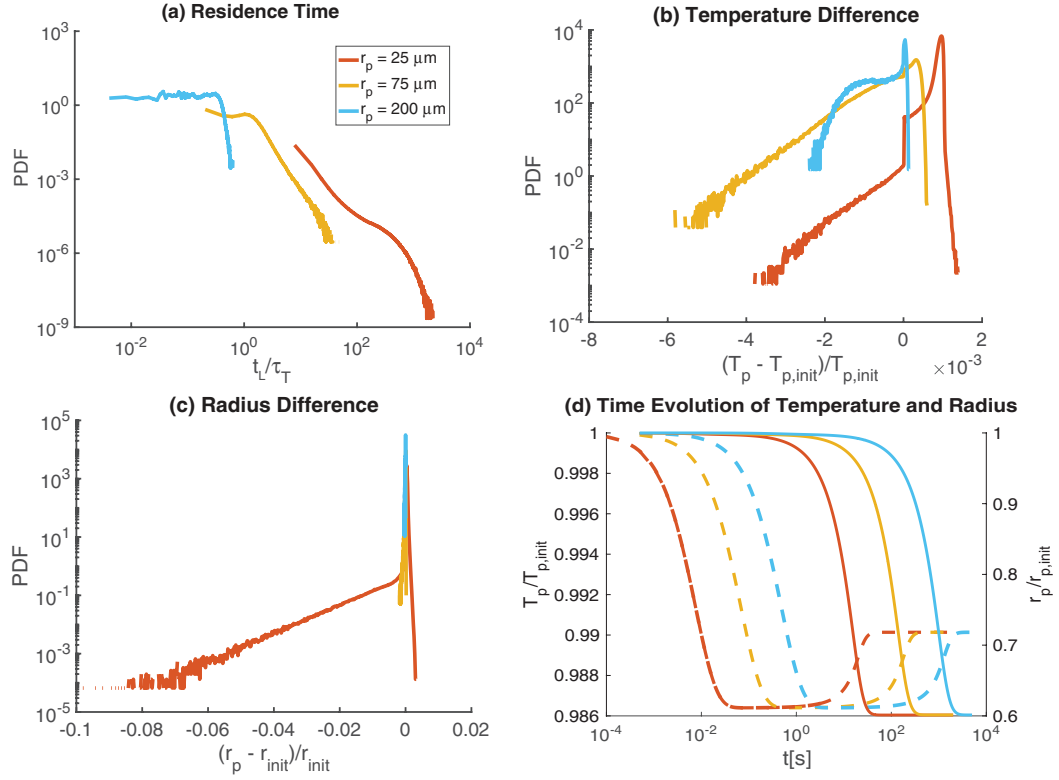


Figure 3.3. Probability density functions (PDFs) of (a) normalised residence time ( $t_L$ ), where temperature time scales  $\tau_T$  for droplets are 0.0075 s (25  $\mu\text{m}$ ), 0.0670 s (75  $\mu\text{m}$ ), 0.4788 s (200  $\mu\text{m}$ ), (b) temperature difference (normalized by its initial temperature), and (c) radius difference (normalized by its initial radius) through their lifetime, compared with (d) time evolution of temperature and radius compared to their initial values during quiescent evaporation ( $T_f = 298.15$  K,  $T_{p,init} = 301.15$  K,  $RH = 90\%$ ). Three types of droplets are presented: small (25  $\mu\text{m}$ , red), medium (75  $\mu\text{m}$ , yellow), and large (200  $\mu\text{m}$ , blue)

### 3.2.1.2 A statistical view

For a better understanding of the collective effect of droplets, we track several key statistics related to the initial and terminal states. Figure 3.3 describes the probability density functions (PDFs) of, (a) the normalized residence time  $t_L$ , (b) temperature change, and (c) radius change throughout the lifetime of small ( $25 \mu\text{m}$ ), medium ( $75 \mu\text{m}$ ), and large ( $200 \mu\text{m}$ ) water droplets. We also plot the solutions for the temporal evolution of temperature (dashed) and radius (solid) (Eqs. 2.15 and 2.17) for the three radii in Fig. 3.3d in quiescent ambient conditions. The gaps between solid and dashed lines of the same colour show the discrepancy between  $\tau_T$  and  $\tau_r$ .

We find in Fig. 3.3a that the droplet residence time ( $t_L$ ) sharply decreases with radius. Since  $\tau_T \propto r_p^2$ , small droplets have sufficient time to change temperature ( $T_p$ ) during their lifetime and adjust themselves to the ambient temperature ( $T_f$ ). In contrast, large droplets only experience very early stages of the evolution depicted in Fig. 3.3d, where the temperature changes relative to the initial temperature ( $T_{p,init}$ ) stay within a narrow range due to their short residence time and large thermal inertia. Specifically, in Fig. 3.3b, the discontinuity around the point where  $T_p - T_{p,init} = 0$  demonstrates the rapid adjustment for small droplets, showing that small droplets either cool due to evaporation or warm from condensation when colliding with the boundary. However, large droplets essentially are all cooled by a small amount from evaporation, as noted in Fig. 3.2.

Regarding the change in droplet radius, Fig. 3.3c shows an agreement with Fig. 3.3b that the majority of small droplets re-enter the lower boundary at a slightly larger radius than their initial radius (also see Fig. 3.2), while the exponential tail of  $25 \mu\text{m}$  describes the longer suspension by turbulence entrainment. This results in up to a  $2 \mu\text{m}$  decrease in radius throughout their lifetime due to evaporative cooling.

### 3.2.1.3 Heat fluxes

To understand how droplets modify the total heat transfer, we are particularly interested in fluxes of both sensible and latent heat. Therefore based on Eqs. [2.20](#)-[2.22](#), we plot the heat fluxes in Fig. [3.4](#). Figures [3.4a](#), [b](#) compare the six components and total heat flux profiles for an unladen flow and a laden case with  $25\ \mu\text{m}$  droplets. Due to the no-penetration conditions at the top and bottom boundaries ( $w = 0$ ), the turbulent fluxes are zero at these two locations. Likewise the particle fluxes are zero at the top boundary because the concentrations approach zero. Furthermore, the total heat flux  $H_T$  is uniform with height, as are the total sensible and latent fluxes, respectively  $H_{s,total}$  and  $H_{L,total}$ . Compared with the unladen case, several terms are modified by  $25\ \mu\text{m}$  droplets, including  $H_{s,sp}$ ,  $H_{L,sp}$ , and  $H_{L,turb}$ , while the overall modification on total heat flux is not as significant as its components.

Figure [3.4c](#) presents the evolution of the the total heat flux as a function of the droplet radius. Although the total heat flux is uniform with height, in the following discussions, it is convenient to describe the magnitude of various flux components at a specific height. For this purpose we use the height at  $z = \delta/8$ , since this is the maximum height droplets can reach without turbulent transport by our particle re-injection scheme. In a qualitative sense, this height is meant to mimic the so-called droplet evaporation layer (e.g. [Andreas et al. \(1995\)](#)). The total heat flux at  $z = \delta/8$  increases with droplet radius and then exhibits a weak non-monotonic shape at large radius with a 1% mass loading. Additionally, the figure shows a limited modification with the largest change (decreasing by 2% from the unladen flow) occurring for smallest droplets ( $25\ \mu\text{m}$ ). Note that since the mass fraction is the same, smaller droplets are more numerous than large droplets in the domain.

It is instructive, however, to look beyond the total heat flux and consider the sensible and latent components individually. Figure [3.5](#) illustrates how the total sensible heat flux  $H_{s,total}$  and its two dominant components  $H_{s,turb}$  and  $H_{s,sp}$  vary

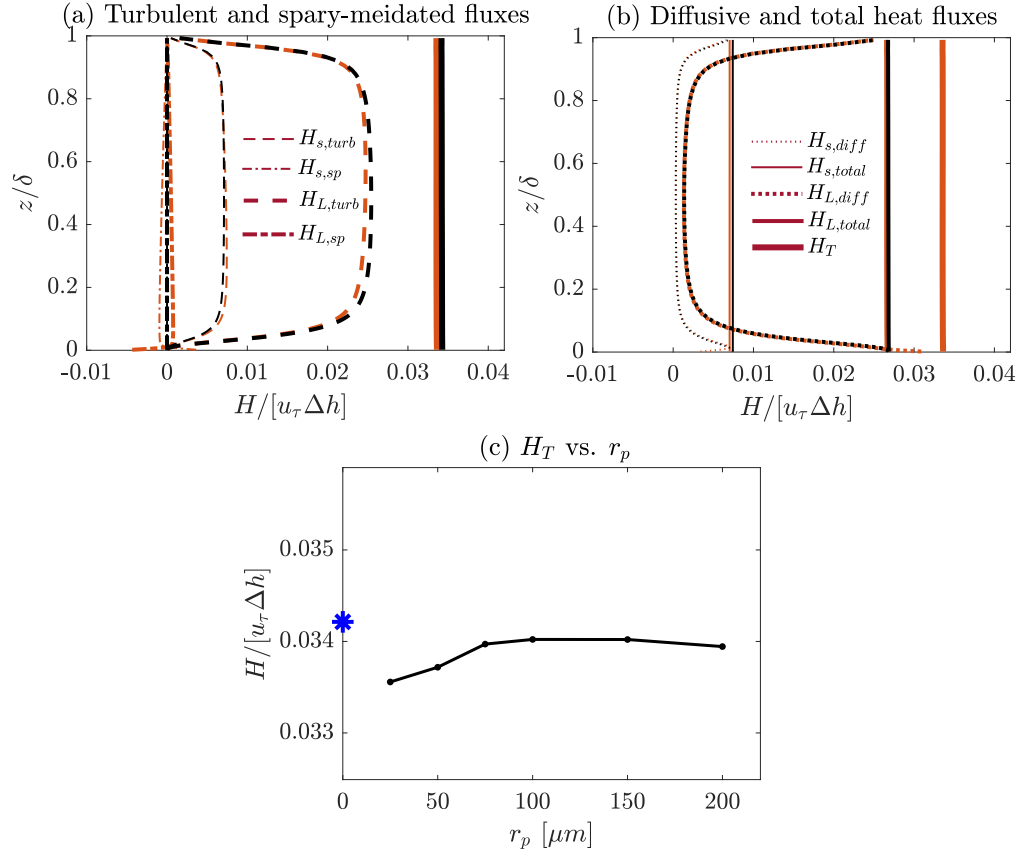


Figure 3.4. Normalized vertical heat fluxes for the  $25 \mu m$  case (brown) and unladen case (black): (a) Turbulent and particle heat fluxes, (b) diffusive and total heat fluxes. Components of heat flux are normalized by  $u_*(h_{bot} - h_{top})$ , where  $h_{bot}$  and  $h_{top}$  are calculated based on Eq. 2.19 given the specific humidity and temperature, and  $u_*$  is the friction velocity at lower boundary. (c) total heat flux extracted at the top of the spray layer versus particle radii. Asterisk indicates the unladen value.

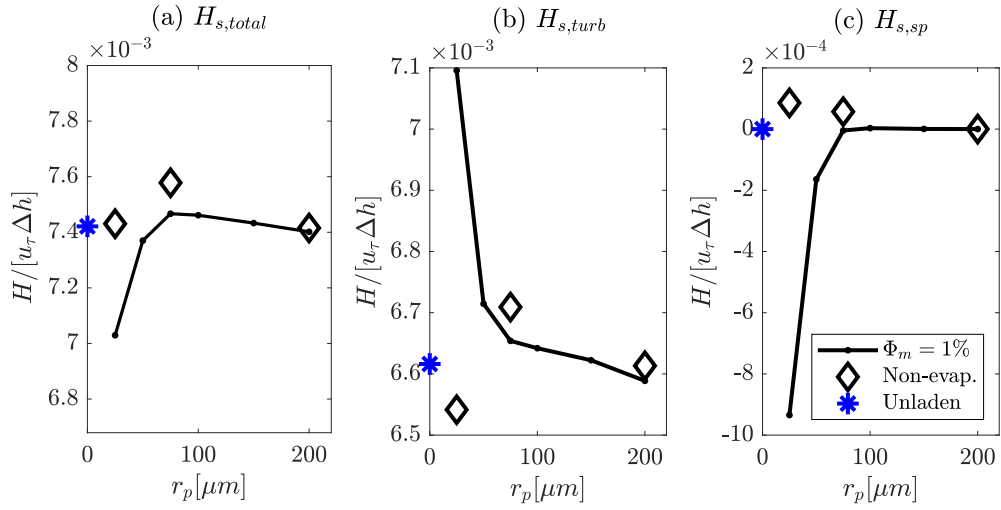


Figure 3.5. Sensible heat flux components versus droplet radius extracted at  $z = \delta/8$ , compared with non-evaporative droplets (diamond), and unladen flow (blue asterisk). Components of heat flux are normalized by the total heat flux between two boundaries in  $z$  direction. (a) Total sensible heat flux  $H_{s,total}$ , (b) turbulent component of sensible heat flux  $H_{s,turb}$ , (c) particle direct sensible flux  $H_{s,sp}$ .

with radius. Compared to the total heat flux shown in Fig. 3.4c,  $H_{s,total}$  has a more pronounced non-monotonic trend with radius, where it has a peak around a radius of  $100 \mu\text{m}$ . The largest magnitude of modification compared to unladen flow is 5.4%, and the peak is 7.1% greater than the minimum at  $25 \mu\text{m}$ . We find that the turbulent and particle-induced components are also heavily influenced by droplet size, and that the modification becomes less sensitive above roughly  $75 \mu\text{m}$ . Comparing the sensible flux with its counterparts from non-evaporative droplets (hollow diamonds) with the same initial and boundary conditions, small evaporating droplets influence  $H_{s,turb}$  and  $H_{s,sp}$  opposite to non-evaporating particles, highlighting the importance of evaporative cooling. However, larger droplets (e.g.  $\geq 100 \mu\text{m}$ ) behave very similar to non-evaporating droplets (consistent with radius statistics shown in Fig. 3.3c); i.e., all three curves, especially  $H_{s,turb}$ , in Fig. 3.5 tend to converge towards the non-evaporative cases with increasing radius. This is in agreement with the results from Sect. 3.2.1.2 and Fig. 3.3a, and suggests that the sensible heat flux corresponding to large droplets is not sensitive to evaporation.

In the present system, vertical latent heat transfer dominates sensible heat transfer (see for example Fig. 3.4a, b), so Fig. 3.5 is only part of the story. Figure 3.6 therefore provides similar quantities as in Fig. 3.5 for latent heat flux components varying with droplet size. Compared to the pronounced modification in sensible flux, modification of total latent heat transfer (Fig. 3.6a) is not as large, ranging within 2% for all radii. The particle-induced latent flux  $H_{L,sp}$  converges to zero at large radii at the top of ejection layer, which is similar to  $H_{s,sp}$ . Likewise, we note that  $H_{L,turb}$  generally increases with radius, but slightly decreases near  $200 \mu\text{m}$ . We also find that the increase for  $H_{L,turb}$  is of the same order of the decrease of  $H_{L,sp}$ , which leads to the relatively flat curve in Fig. 3.6a.

The relation between  $H_{L,turb}$  and  $H_{L,sp}$  demonstrates a cancellation between turbulent and particle-induced heat fluxes. A similar result is found in Fig. 3.5 for

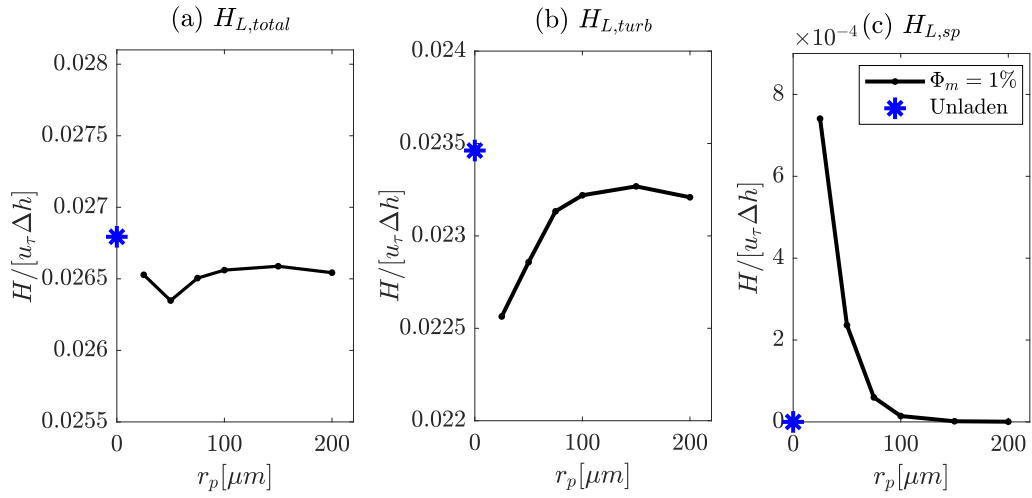


Figure 3.6. Latent heat flux components versus droplet radius, compared with unladen flow (blue asterisk) at the top of ejection layer ( $z = \delta/8$ ). Components of heat flux are normalized by the total enthalpy difference between the two boundaries in the  $z$  direction. (a) Total latent heat flux  $H_{L,total}$ , (b) turbulent component of latent heat flux  $H_{L,turb}$ , (c) particle direct latent flux  $H_{L,sp}$ .

$H_{s,turb}$  and  $H_{s,sp}$ . In addition, the latent components evolve opposite to their sensible counterparts: the two particle-induced terms,  $H_{L,sp}$  and  $H_{s,sp}$ , are of opposite sign, which indicates that droplets travelling upwards are releasing moisture and cooling the surrounding air, and the opposite is true for downward travelling droplets. We also find that  $H_{L,turb}$  has a qualitatively opposite evolution with radius to  $H_{s,turb}$ . Similar evidence of this cancellation between latent and sensible heat flux has been documented in previous numerical studies (Edson et al., 1996; Fairall et al., 1994), where the decrease of sensible heat for droplet released at wave height offsets the increase of latent heat flux. In the current simulation, the multiple cancellation effects not only lead to an overall small heat flux modification, but also make the total heat flux relatively insensitive to droplet radius (see Fig. 3.4b).

Therefore, we summarize that droplet size influences the balance of residence time scale ( $t_L$ ) and thermodynamics time scale ( $\tau_T$  or  $\tau_r$ ), which leads to different combined behavior, although the total modification on heat flux is modest. We mainly focus on droplets in the small and large limits, because the transition between the two behaviors is relatively narrow. Small droplets with shorter thermodynamic response times have more flexibility to interact with the environment. Due to the longer suspension time, evaporative cooling of small droplets leads to a self-cancelling effect, where sensible and latent components of heat flux are modified but compensated, yielding a limited total modification. Large droplets have ballistic inertial motions near the lower boundary and remain almost unchanged in temperature and radius, exhibiting different behavior from small droplets. While each evaporating drop still releases a small amount of latent heat during preliminary stage of evaporation (see Fig. 3.3d), the cumulative effect on the total latent heat flux is trivial once averaged across the domain. This eventually leads to a very slight modification of the total heat flux.

### 3.2.2 Influence of mass loading

In the previous section, the focus was mainly on the role of droplet radius on thermodynamic evolution and feedback at a fixed droplet loading  $\Phi_m = 1\%$ . We now comment on the influence from droplet mass loading by extending the mass loading of droplets to  $\Phi_m = 5\%$  and  $10\%$  while keeping boundary conditions the same. Three different radii are selected,  $25\ \mu\text{m}$ ,  $75\ \mu\text{m}$ , and  $200\ \mu\text{m}$ , representing small, medium, and large droplets. We focus mainly on how the total heat flux and its components change with increasing mass fraction.

Figure 3.7 displays the vertical profiles of the total heat flux and its components for  $25\ \mu\text{m}$  and  $200\ \mu\text{m}$  at  $\Phi_m = 10\%$ , as a counterpart of Figs. 3.4a, b at  $\Phi_m = 1\%$ . For  $H_T$ , large droplets provide a stronger modification than small droplets. The increase of large droplets is almost solely from the two turbulent fluxes,  $H_{s,turb}$  and  $H_{L,turb}$ , and part of latent heat flux  $H_{L,sp}$  near lower boundary. However, in Fig. 3.7a for small droplets, all sensible and latent components are modified and continue to cancel each other, yielding a total heat flux which remains nearly unchanged from both the unladen and  $\Phi_m = 1\%$  cases. For example, Fig. 3.8 shows that this is generally true up to a mass loading of  $10\%$ , since in all cases the particle flux components and the modifications to the turbulent fluxes all cancel each other.

Regarding the total heat flux  $H_T$ , large droplets tend to be slightly more sensitive to mass fraction, which is also shown in Fig. 3.8. In Fig. 3.8a, from  $\Phi_m = 1\%$  to  $10\%$ , the magnitude of  $H_T$  increases by  $6\%$  for the  $75\ \mu\text{m}$  and  $200\ \mu\text{m}$  droplets but decreases by  $1.6\%$  for  $25\ \mu\text{m}$  droplets. However, Figs. 3.8c, e show that large droplets are insensitive to mass fraction for heat flux directly from the droplet feedback,  $H_{s,sp}$  and  $H_{L,sp}$ . In particular, the sensible heat flux  $H_{s,sp}$  is very insensitive to droplet mass fraction up to  $\Phi_m = 10\%$  (note that  $75\ \mu\text{m}$  and  $200\ \mu\text{m}$  have overlapping curves). Considering that large droplets are confined within the ejection layer (as shown in Fig. 3.2) and have short lifetimes, the added contribution to the sensible heat flux

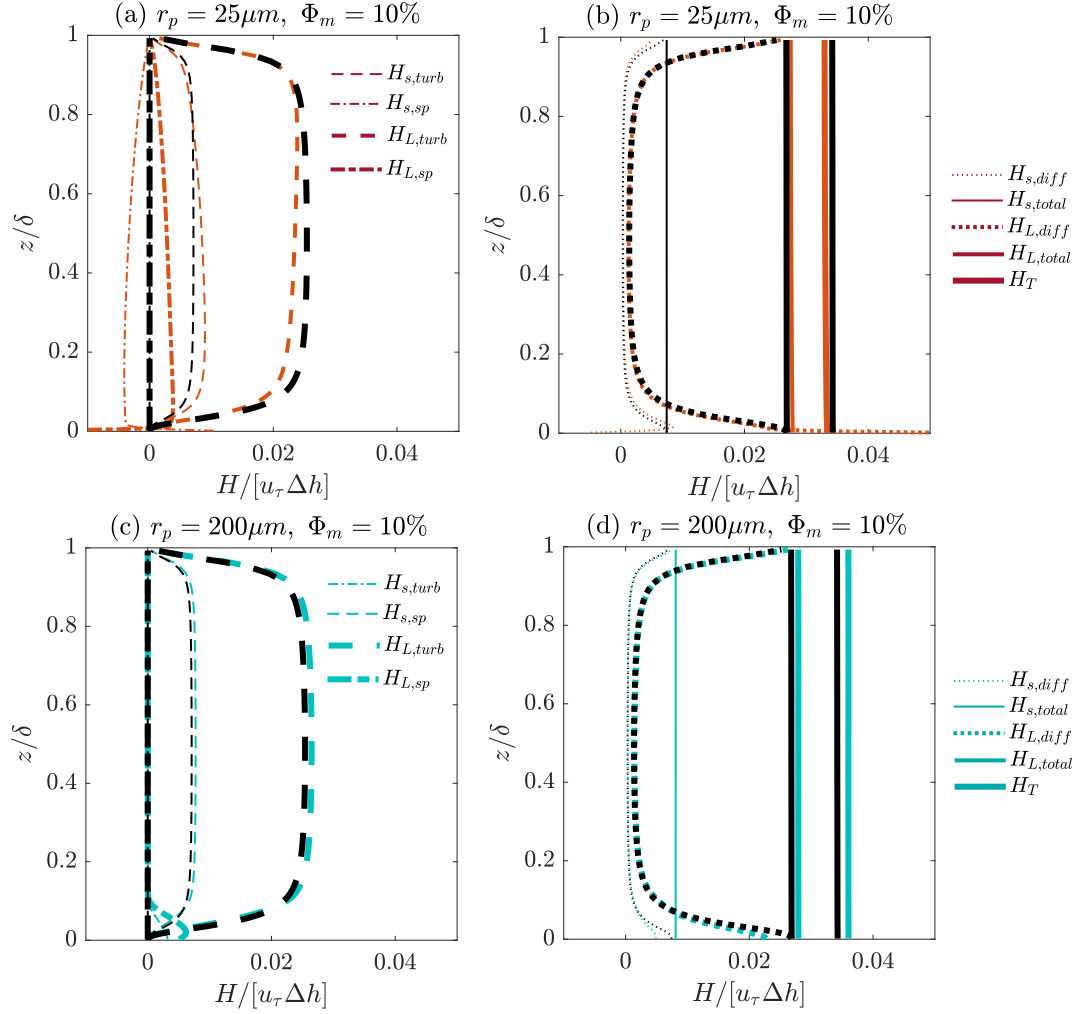


Figure 3.7. Normalized total heat flux  $H_T$  for a mass loading of  $\Phi = 10\%$  for  $25\mu m$  case (brown),  $200\mu m$  case (blue) and unladen case (black). (a) (c) Turbulent and particle heat fluxes, and (b) (d) diffusive and total heat fluxes. Heat fluxes are normalized by the total enthalpy difference between the two boundaries in the  $z$  direction.

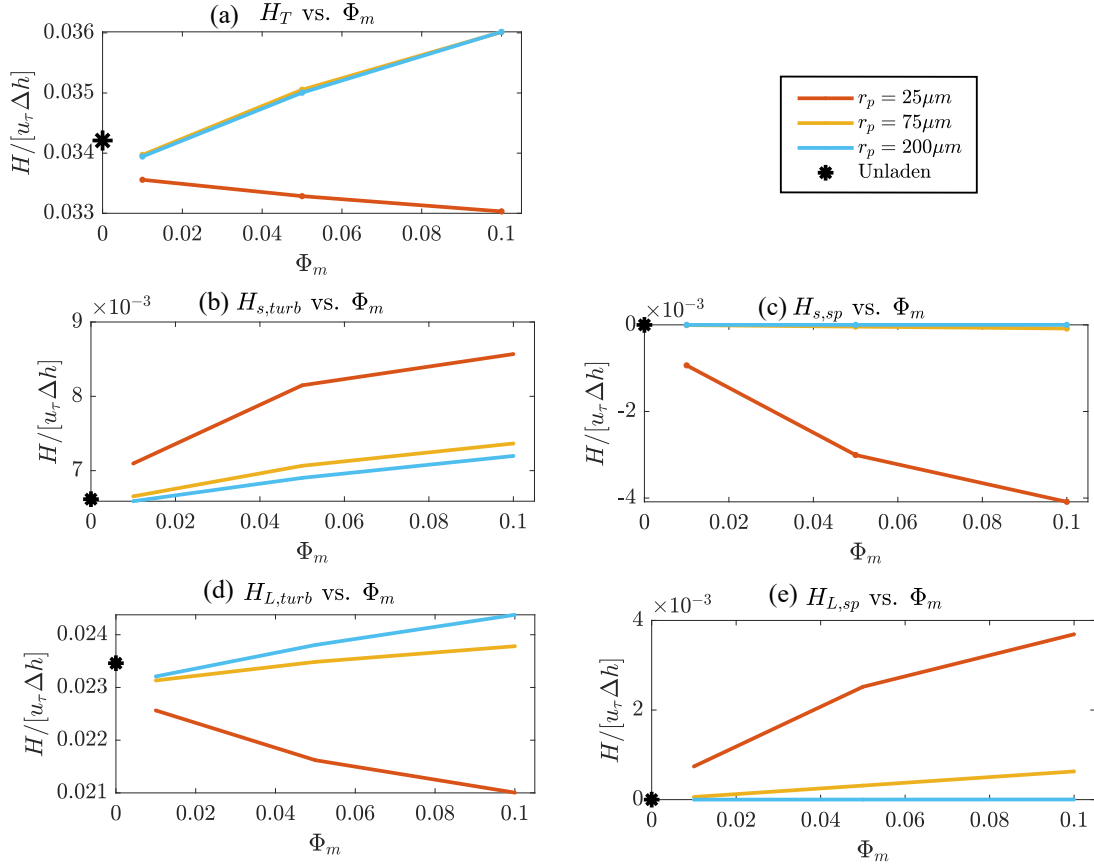


Figure 3.8. Sensible and latent heat fluxes at a height of  $z = \delta/8$  versus droplet mass fraction  $\Phi_m$ , compared with unladen flow (blue asterisk): (a) Total heat flux  $H_T$ , (b) turbulent component of sensible heat flux  $H_{s,total}$ , (c) particle sensible flux  $H_{s,sp}$ , (d) turbulent component of latent heat flux  $H_{L,turb}$ , (e) particle latent flux  $H_{L,sp}$ . Note: in (a) and (c), 75  $\mu m$  and 200  $\mu m$  have overlapped curves.

does not cancel in the same way as for smaller droplets which essentially do not participate in the evaporation process.

Therefore, the influence from mass loading is more important when considering heat flux from large droplets than small droplets, though the flux modification for both small or large droplets at  $\Phi_m = 10\%$  is still not very pronounced.

### 3.2.3 Influence of boundary conditions

Here, we probe the effect of boundary conditions in order to better characterize how well our idealized simulation set-up can be extended to understand more realistic conditions. Hence we systematically vary both the top and bottom temperatures and relative humidities; the details of the four different cases are given in the Table [2.3](#) where the “benchmark” condition is the “M1” set-up in Table [2.3](#). The five boundary conditions (“M1”, “M2”, “M4”, “M5”, and “M7”) represent different enthalpy gaps between the two boundaries distributed in various ways between sensible and latent heat. For example case “M2” would only yield a latent heat flux and no sensible heat flux since the top and bottom temperatures are held equal. Similarly, we expect stronger sensible heat transfer in group “M4” than the “M1” (benchmark) group.

Figure [3.9](#) shows that regardless of the boundary conditions, however, when normalized by the total enthalpy difference between the top and bottom boundaries, the total heat flux and its combined diffusive, particle-induced, and turbulent components remain nearly unchanged. This is likewise true for both small (Fig. [3.9a](#)) and large (Fig. [3.9b](#)) droplets, indicating that the consequent feedback of droplets from the thermodynamic evolution onto the surrounding flow identified in the previous sections is a robust effect that remains identical with changing boundary conditions (given proper normalization).

This insensitivity to boundary conditions, much like the influence of mass loading, is due largely to the aforementioned cancellation between the particle flux compo-

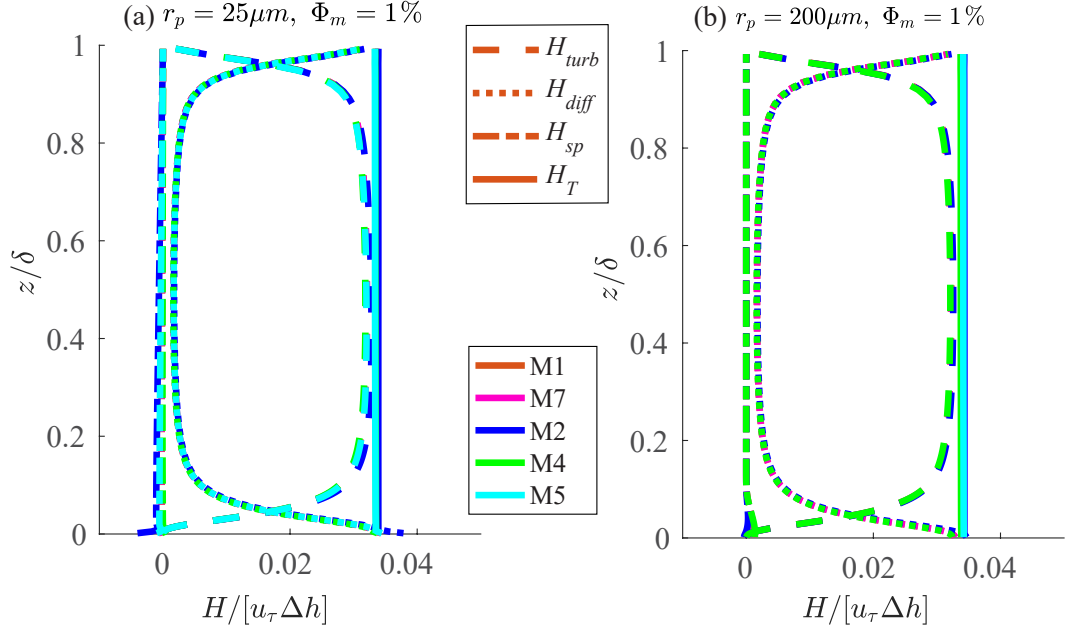


Figure 3.9. Normalized vertical heat flux for different boundary conditions. (a) Profiles of vertical heat flux for  $25 \mu m$  droplets. (b) Profiles of vertical heat flux for  $200 \mu m$  droplets. The colors are given in the legend. Here we combine the sensible and latent heat fluxes from same physical mechanism as one term, e.g.  $H_{turb} = H_{s,turb} + H_{L,turb}$ ,  $H_{diff} = H_{s,diff} + H_{L,diff}$ , etc. Note: Lines not shown in the plot are overlapped with same terms for different BCs.

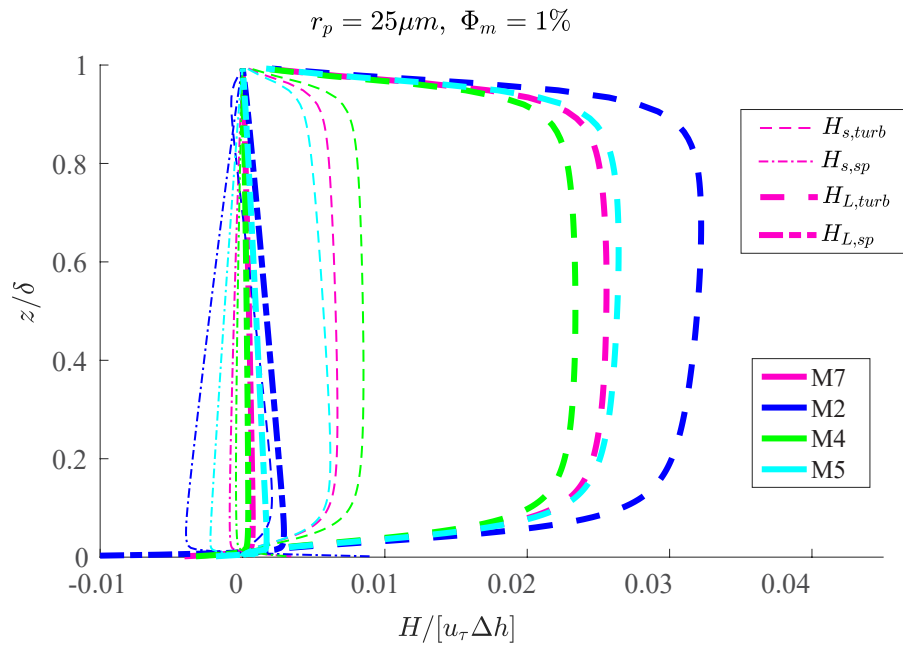


Figure 3.10. Selected normalized components of sensible and latent heat flux,  $H_{s,turb}$ ,  $H_{s,sp}$ ,  $H_{L,turb}$ , and  $H_{L,sp}$ , for the four boundary conditions given in Table [2.3](#)

nents  $H_{s,sp}$  and  $H_{L,sp}$  and the modified turbulent fluxes  $H_{s,turb}$  and  $H_{L,turb}$ . Figure 3.10 illustrates this cancellation effect for small droplets for the various boundary conditions. The modifications to sensible turbulent and particle-induced fluxes are in all cases offset by modifications to the latent turbulent and particle-induced fluxes, leading to an overall weak influence in total heat flux regardless of the boundary conditions.

Finally we note that the results presented herein are also insensitive to the initial droplet temperature ( $T_{p,init}$ ). Small droplets, which experience the most complex thermodynamic evolution in the domain, quickly adjust to their surrounding temperature and therefore forget their initial value. This has been tested in the current set-up by manually changing the initial droplet temperature to be different than the bottom boundary temperature, and minimal changes were observed (not shown here). This is consistent with the findings of Mueller and Veron (2014a) which points out that small droplets rapidly exchange heat before reentering the ocean.

### 3.3 Summary

We investigated the feedback due to evaporating droplets in the turbulent marine boundary layer via idealized numerical simulations. Particularly we focused on how droplets modify the total heat/enthalpy transfer across the domain.

We observe that the feedback and evolutionary behavior of droplets can be classified into two broad categories: “small” and “large” droplets, whose definitions are based on the balance between the droplet residence time and its thermodynamic time scales. Small droplets are more susceptible to entrainment into turbulent motions and transported throughout the domain and thus have a longer residence time, and at the same time have a more rapid thermodynamic response time than large droplets. This combination of scales for small droplets, however, leads to a cancelling feedback effect between modifications to sensible and latent heat fluxes, which results in a

limited overall modification to the total heat flux across the boundary layer. Large droplets with longer thermodynamic time scales, however, do not have sufficient time to significantly change both temperature and radius. Therefore, large droplets behave somewhat as non-evaporating droplets, but also have small modifications to the total heat flux. See Fig. 3.11 for a schematic.

While the direct numerical simulations performed are an idealized representation of the spray-laden MABL, we have demonstrated a robust insensitivity of this overall picture to both mass loading and boundary conditions. Increased mass loading affects small and large droplets slightly differently, since large droplets barely change the temperature and radius during evaporation and therefore have an incomplete feedback mechanism compared to the small droplets. Thus the influence of increasing mass loading is greater for larger droplets than it is for smaller ones. Likewise the boundary conditions do not affect the feedback due to small droplets but only increase the magnitude of the individual terms that ultimately cancel one another.

In the context of spray modeling in the real MABL, we emphasize that feedback between droplet modifications to sensible and latent heat fluxes are critical if the overall affect of spray is to be modelled accurately. Our results show a qualitative difference from the significant increase of the total heat flux found in previous numerical studies (Andreas and Emanuel, 2001; Andreas et al., 2015; Mueller and Veron, 2014b), but this is perhaps due to the different coupling physics of droplets and turbulence. However, we found our results are in a qualitative agreement with Edson et al. (1996) and Bianco et al. (2011) with respect to the cancellation effect and limited total flux modification. For small droplets that have the smallest thermodynamic response times, this feedback between their influence on sensible and latent heat fluxes could render them completely ineffective at increasing heat fluxes from the ocean to the atmosphere. This is perhaps the reason why all existing observations (e.g. DeCosmo et al. (1996); Drennan et al. (2007); Zhang et al. (2008)) at high

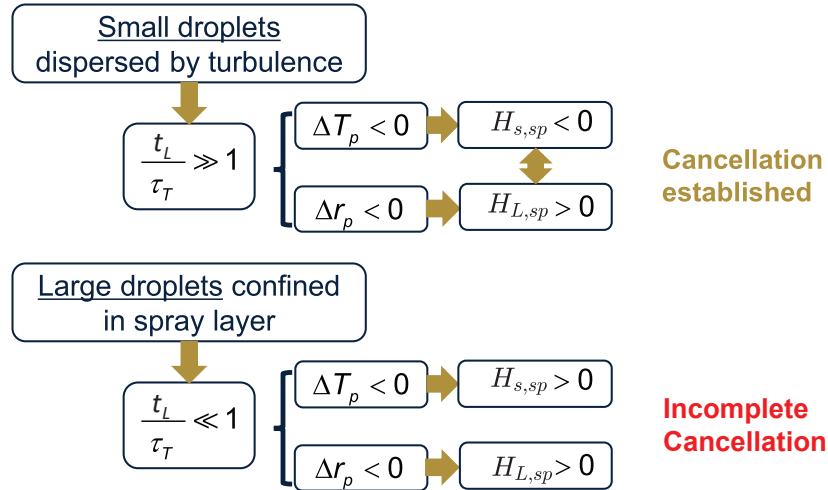


Figure 3.11. A schematic of the influences of large and small droplets on particle-induced enthalpy.

wind speeds show no significant increase of heat flux coefficients. Large droplets on the other hand, potentially enhance latent heat fluxes due to their incomplete evaporation cycle, but this enhancement is highly dependent on their concentration and suspension — physical processes that are not fully described in the present system.

## CHAPTER 4

### ASSESSING BULK ALGORITHMS OF AIR-SEA HEAT FLUXES

#### 4.1 Overview

The primary aim of this study is to use DNS to directly test certain assumptions made in bulk estimates of spray-mediated thermodynamic fluxes, and in particular those of [Fairall et al. \(1994\)](#) and [Andreas et al. \(2015\)](#). For the bulk models, we simplify the details (e.g. spray generation), and focus instead on the fundamental hypotheses made for the total heat flux and spray microphysics that can be assessed by DNS.

For DNS, we use the same numerical scheme of droplet-laden turbulent flows as our previous study (PR17) that is adapted from [Helgans and Richter \(2016\)](#). We treat turbulent air flows and spray droplets separately. Hence there are two phases in the model: a carrier phase (air) and a dispersed phase (droplets). For the carrier phase, we use the DNS model to resolve turbulence in an open-channel flow. For spray droplets, we compute the dynamics and thermodynamics of each droplet individually from Lagrangian perspective, and treat them as point particles which respond to the local fluid velocity, temperature, and humidity. In this section, we will introduce both the bulk and DNS models as well as the methodology for testing the bulk models using DNS.

In our DNS model, the open-channel turbulent flow provides a uniform total vertical heat flux. This constant vertical heat flux is consistent with what bulk models commonly assume and allows for us to compare the two types of models for

the thermodynamic coupling between phases and the role of droplet microphysical processes. We compute each component of heat flux found in Eq. (2.23) explicitly via Eqs. (2.1)-(2.10) in DNS. Therefore, we can attempt to reconstruct the DNS-obtained fluxes via the bulk model formulations and provide physical interpretations behind the fitting coefficients. In addition, for the bulk estimation of spray-mediated fluxes, all variables in Eqs. (2.30) and (2.31) are known or can be measured from the Lagrangian solutions of DNS.

We firstly examine the how well F94 and A15 predict the spray-mediated heat fluxes given by Eqs. (2.24) to (2.29). Then, we test the magnitude of spray’s feedback term ( $\gamma$ -term) to predict the total heat flux given only an interfacial heat flux without spray droplets and the mean difference of spray’s temperature ( $\Delta T_p$ ) and radius ( $\Delta r_p$ ). Finally, we will discuss the approximation of  $\Delta T_p$  and  $\Delta r_p$  as well as spray’s overall influence on the total heat flux  $H_T$ .

## 4.2 Results and discussion

### 4.2.1 Predicting spray-mediated heat fluxes

We start the assessment with the spray-mediated heat fluxes. First, we follow the expressions of F94 via Eqs. (2.24) to (2.26), which in A15’s notation use  $\alpha = \beta = 1$  and  $\gamma = 0$  according to Eqs. (2.27) to (2.29). Thus for F94, the latent spray-mediated heat flux is approximated by the nominal flux  $\bar{Q}_L$ , and the sensible spray-mediated heat flux is expressed as the difference between the total and the latent fluxes,  $\bar{Q}_s - \bar{Q}_L$ . To test the estimates given by Eqs. (2.25) and (2.26), we plot in Fig. 4.1 the DNS-computed spray fluxes  $H_{s,sp}$  and  $H_{L,sp}$  against  $\bar{Q}_s - \bar{Q}_L$  and  $\bar{Q}_L$ , respectively, where based on Eqs. (2.30) and (2.31) we calculate  $\bar{Q}_s$  and  $\bar{Q}_L$  from droplet statistics  $\Delta T_p$  and  $\Delta m_p$  known from the DNS. Spray radii in the plot range from  $20\mu m$  to  $200\mu m$ , and we include all three Reynolds numbers and boundary conditions. We normalize

the heat fluxes by the product of friction velocity ( $u_\tau$ ) and total enthalpy difference ( $\Delta h = h_{bot} - h_{top}$ ) between the top and bottom boundaries.

Fig. 4.1 shows that spray behaves differently as a function of droplet size. For example, in panel [b] for the latent heat flux  $H_{L,sp}$ , 200  $\mu\text{m}$  droplets provide a positive contribution of latent heat to the system ( $H_{L,sp} > 0$ ) although the amount is small. As radius decreases, the magnitude of  $H_{L,sp}$  increases, and spray actually extracts latent heat from the air when the bottom surface exhibits a warmer and more humid condition. However, both panels in Fig. 4.1 show that F94 has drawbacks of predicting heat fluxes of smaller droplets (25  $\mu\text{m}$  or less), in particular for the sensible spray-mediated heat flux  $H_{s,sp}$ , where deviations are observed for the smaller droplets (shown by asterisks and dots). Specifically, points beneath the reference line in panel [a] indicate an overprediction of spray-mediated sensible heat flux calculated by the F94 model for small droplets. Meanwhile, panel [b] suggests a slight underprediction of latent spray-mediated heat flux via the F94 model for small droplets, although this effect is smaller. Nevertheless, the different directions of deviations indicate an internal reallocation of sensible and latent spray-mediated heat flux due to spray evaporation/condensation, which is related to the cancellation and feedback effects documented in PR17. Thus, if the deviations for smaller droplets are due solely to the internal reallocation of sensible and latent heat fluxes, we would expect F94 to predict the total spray-mediated heat flux more accurately than its sensible/latent components.

Therefore Fig. 4.2 plots the total spray-mediated heat flux as calculated by the DNS ( $H_{sp}$ , vertical axis) and the F94 model (Eq. 2.24, horizontal axis). As seen in the figure, F94 indeed does predict the total spray-mediated heat flux fairly accurately, which confirms that the deviations in Fig. 4.1 are due to reallocation of sensible and latent heat fluxes. In addition, the clustering around the reference lines in Fig. 4.2 confirms the assumption by F94 that the total heat exchanged with spray is reflected

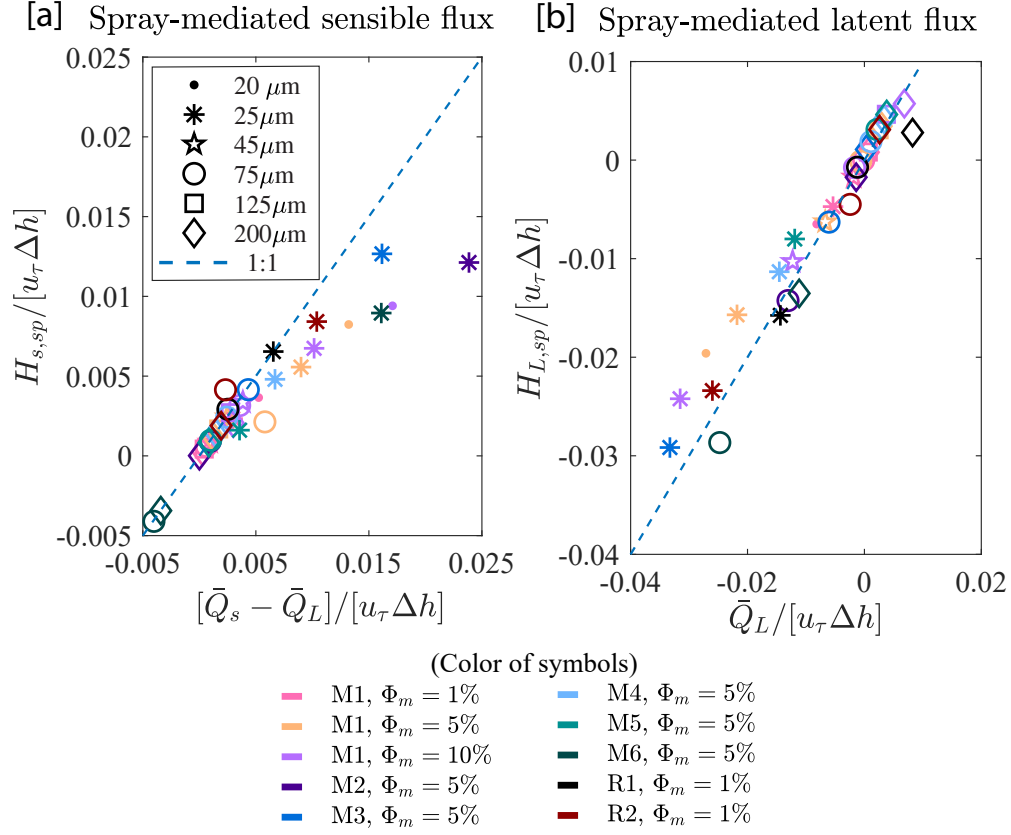


Figure 4.1. Estimated spray-mediated heat fluxes vs. DNS computed results: [a] spray-mediated sensible heat flux ( $H_{s,sp}$  vs.  $\bar{Q}_s$ ), and [b] spray-mediated latent heat flux ( $H_{L,sp}$  vs.  $\bar{Q}_L$ ). The product of the friction velocity ( $u_\tau$ ) and the vertical enthalpy difference of the domain ( $\Delta h$ ) is used to normalize heat fluxes.

in its temperature change (via  $\bar{Q}_s$ ). This is because the changes of droplet radius and temperature are separate processes occurring at disparate response timescales — see for example Fig. 1 in [Andreas and Emanuel \(2001\)](#).

In the above discussion, we verify that the F94 model works well at predicting total and latent spray-mediated heat fluxes when applying the known statistics of spray microphysics directly retrieved from DNS. Similar conclusions can be drawn for the A15 model. Based on Fig. [4.1](#), we can confirm that the coefficient  $\alpha$  for latent flux  $H_{L,sp}$  in the A15 model (Eqs. [\(2.27\)](#) and [\(2.28\)](#)) is indeed  $O(1)$ . However,

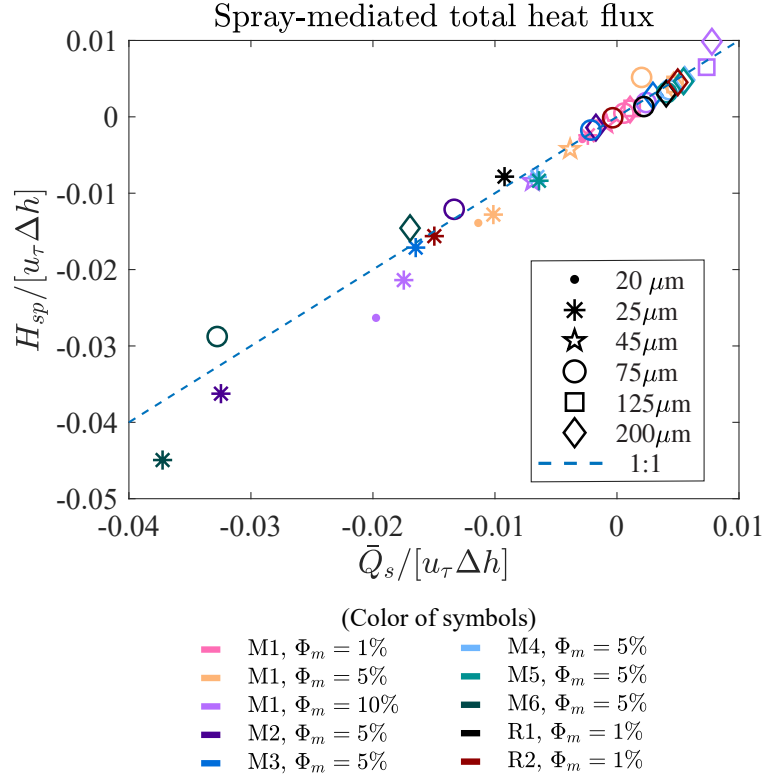


Figure 4.2. DNS-computed spray-mediated total heat flux  $H_{sp}$  vs. nominal sensible heat flux ( $\bar{Q}_s$ ), showing spray-mediated heat fluxes are reflected in its internal energy change. Heat fluxes are normalized by the product of the friction velocity ( $u_\tau$ ) and the vertical enthalpy difference of the domain ( $\Delta h$ ). Various simulations with different  $Re_\tau$ ,  $\Phi_m$ , and size are denoted by color and marker in the legends. See Table [2.3](#) for simulation settings.

the value of  $\beta$  based on the DNS for the spray-mediated sensible heat flux is not as large as what the A15 model predicts. According to A15,  $\beta = 15.15$ , while the DNS results suggest that  $\beta \approx 1$ , as evidenced by symbols clustering near the reference line in the left panel of Fig. 4.1. Furthermore, to predict the spray-mediated  $H_{s,sp}$ , we find that the feedback coefficient  $\gamma$  is negligible if we assume  $\alpha = 1$ . Therefore, the implied values  $\alpha = \beta = 1$  in the F94 model are a good approximation of the total spray-mediated heat flux given a correct estimate of spray microphysics (i.e.  $\Delta m_p$  and  $\Delta T_p$ ), and the A15 model may overestimate the sensible heat flux by an order of magnitude due to the large value of  $\beta$ . The question of whether or not a nonzero  $\gamma$  is required to describe interplay between spray-mediated and interfacial fluxes is considered next.

#### 4.2.2 The feedback effect of spray evaporation

The above analysis demonstrates that one can obtain reasonably accurate predictions for the total spray-mediated flux  $H_{sp}$  with an accurate prediction of  $\bar{Q}_L$  and  $\bar{Q}_s$ . However, it remains to be verified whether or not the spray-mediated fluxes can simply be added to the spray-free interfacial fluxes to yield the total heat flux. In the F94 model, the total heat flux is  $H_T = H_{int} + H_{sp}$ , which makes no attempt to account for any reductions in the interfacial flux due to the presence of the spray-mediated component. In contrast, the A15 model considers a feedback effect between the two, which is associated with the latent heat released from the spray by the  $\gamma$  parameter in Eq. 2.28. The parameter  $\gamma$  takes into account the fact that latent spray-mediated heat flux from the droplet phase can modify the corresponding interfacial flux, presumably by moistening the near-surface air and increasing the temperature gradient by evaporative cooling (e.g., when  $\gamma > 0$ ). Since we calculate each term in Eq. (2.23) explicitly in DNS, we shift our focus to the total heat flux  $H_T$  and discuss whether the bulk models provide a reasonable estimate for the total heat flux as well.

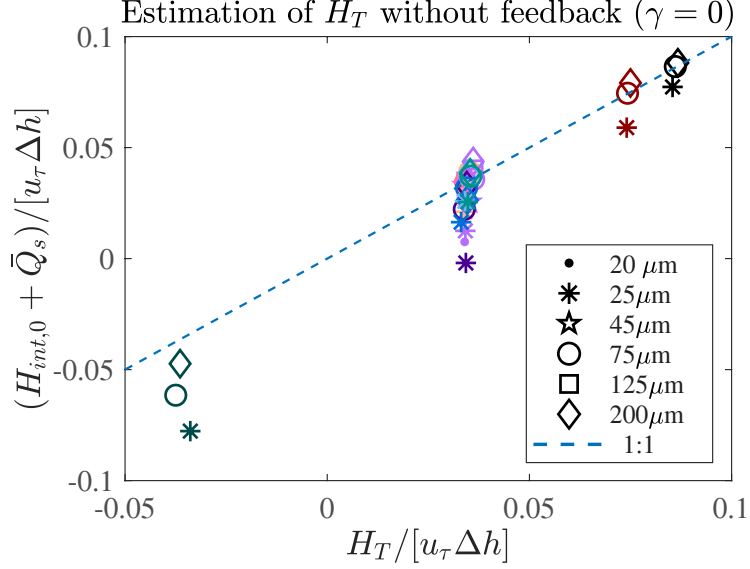


Figure 4.3. DNS-computed total heat flux ( $H_T$ ) versus the estimated total heat flux ( $H_{sp} + H_{int,0}$ ) by adding the DNS-computed spray-mediated flux with the corresponding unladen total interfacial heat flux. The heat fluxes are normalized by  $u_\tau \Delta h$ . Color of symbols and marker styles in the legends match Fig. 4.2

We first evaluate whether or not one can add the spray-mediated heat fluxes to the interfacial heat fluxes estimated from spray-free conditions as F94 suggests. To test this assumption, we compute an unladen case (with subscripts ‘0’) from DNS where the total heat flux consists solely of the interfacial flux  $H_{int,0}$ . Then, we add  $H_{int,0}$  to the bulk estimate of the total spray-mediated flux  $H_{sp}$  by F94 via Eqs. (2.24) and (2.30) for the corresponding spray-laden cases, and we plug them in Eq. (2.23), i.e.  $H_T = H_{int,0} + \bar{Q}_s$ .

Fig. 4.3 shows that the DNS-calculated  $H_T$  versus the estimates given by the F94 model do not always agree. In particular, the estimates for smaller droplets ( $r_p < 25\mu\text{m}$ ) can deviate by up to 120% from the corresponding DNS-calculated values, although the predictions of F94 are more acceptable for larger droplets ( $r_p > 75\mu\text{m}$ ) especially with warmer bottom surface. Thus, according to Fig. 4.3, how well F94

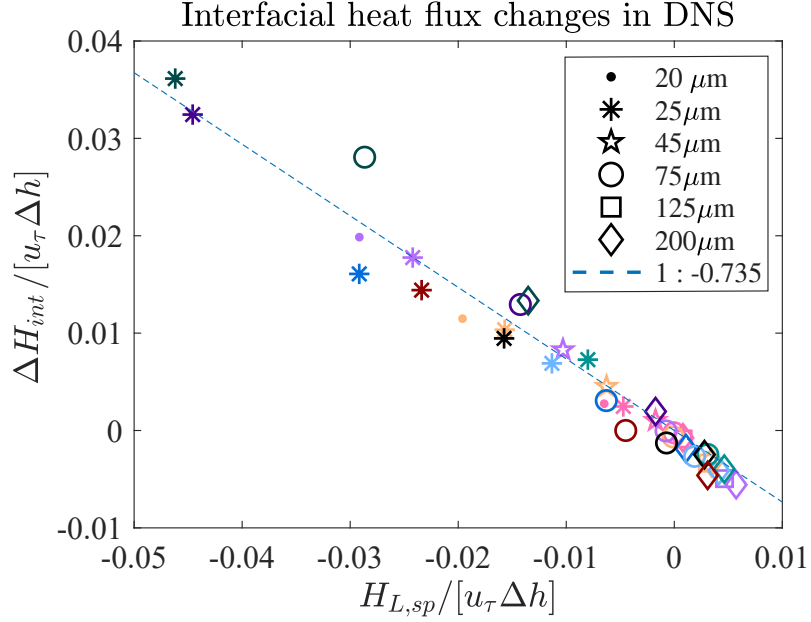


Figure 4.4. Modification of total interfacial heat flux ( $\Delta H_{int}$ ) versus nominal latent heat flux  $\bar{Q}_L$ , showing that evaporation of spray induces a modification of the total interfacial heat flux. Color of symbols and marker styles in the legends match Fig. 4.2.

predicts the  $H_T$  depends on the droplet size.

Along the lines of A15, we assume the error in Fig. 4.3 is due to the feedback effect between spray and interfacial fluxes. We test this assumption by defining the change of interfacial flux ( $\Delta H_{int}$ ) from the unladen case after loading spray droplets in Eq. (4.1),

$$\Delta H_{int} = H_T - (H_{sp} + H_{int,0}). \quad (4.1)$$

If the feedback is negligible, the  $\Delta H_{int}$  should be approximately zero. Otherwise,  $\Delta H_{int}$  in Eq. (4.1) quantifies the net feedback between spray and interfacial heat fluxes that is missing in bulk models.

In Fig. 4.4, we plot  $\Delta H_{int}$  versus the DNS-calculated spray-mediated latent heat flux  $H_{L,sp}$ . Interestingly, comparing the net feedback  $\Delta H_{int}$  with  $H_{L,sp}$  in Fig. 4.4, we find that  $\Delta H_{int}$  is *inversely* proportional to  $H_{L,sp}$ . The negative linear trend

in Fig. 4.4 is in contrast to the feedback effect assumed by A15, which indicates a negative feedback effect induced by spray. Hence the interfacial heat flux will adjust itself to attenuate the influence from spray evaporation rather than being enhanced by spray droplets. We can describe this linear relationship as

$$\Delta H_{int} = \gamma H_{L,sp}, \quad (4.2)$$

where the coefficient is determined as  $\gamma = -0.7349$  with  $R^2 = 0.9895$  by linear regression.

As we have shown that the bulk estimates of spray-mediated latent heat flux,  $\bar{Q}_L$ , agree reasonably well with the DNS-calculated  $H_{L,sp}$  in Fig. 4.1[b], we arrive at an approximation for the total heat flux:

$$H_T \approx H_{int,0} + \bar{Q}_s + \gamma \bar{Q}_L, \quad (4.3)$$

where  $\gamma = -0.7349$ ,  $H_{int,0}$  is the unladen total interfacial heat flux, and  $\bar{Q}_s$  the approximation of the total spray-mediated heat flux  $H_{sp}$  shown in Fig. 4.2

With the correction of the negative feedback term from DNS results, we plot the two sides of Eq. (4.3) using bulk estimates of spray-mediated heat fluxes in Fig. 4.5. It is obvious that the errors are significantly reduced to a range around 5% compared to Fig. 4.3, especially for smaller droplets. Therefore, the negative feedback term ( $\gamma < 0$ ) in Eq. (4.3) suggests that both F94 and A15 models can overestimate the influence of spray on the total heat flux when there is a substantial amount of latent heat flux released by spray, although the F94 model works when the spray-mediated latent flux  $\bar{Q}_L$  is small. Moreover, the A15 model can further overestimate it by imposing a positive feedback term ( $\gamma > 0$ ). We briefly summarize the main comparisons of the bulk algorithms with DNS in Table 4.1.

Based on Eq. (4.3), one can see that the quality of estimating  $\bar{Q}_s$  and  $\bar{Q}_L$  deter-

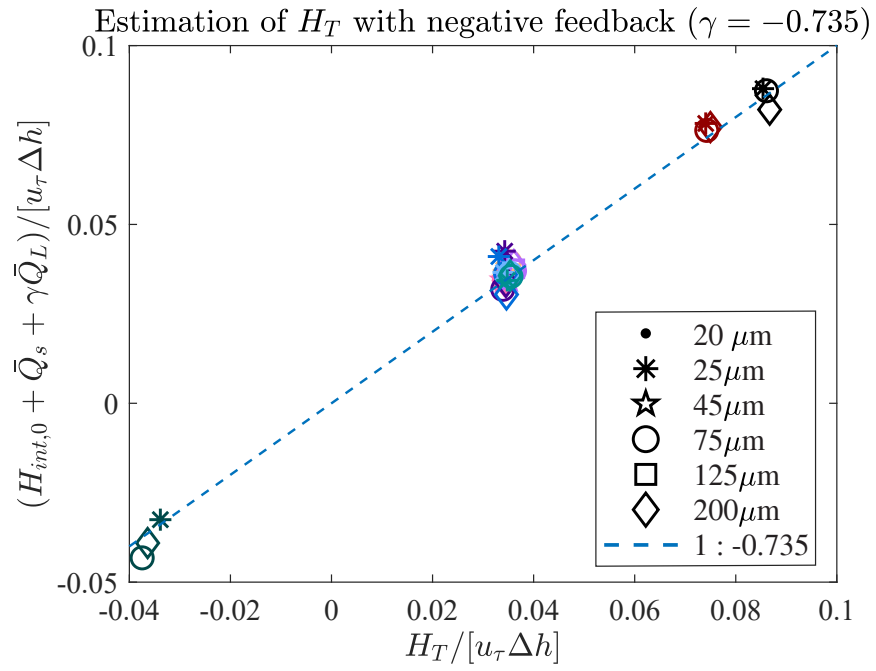


Figure 4.5. DNS-computed total heat flux ( $H_T$ ) versus the estimated total heat flux by Eq. (4.3) with a negative feedback term from the spray-mediated latent heat flux  $\bar{Q}_L$ . Color of symbols and marker styles in the legends match Fig. 4.2

TABLE 4.1

COEFFICIENTS OF BULK MODELS AND DNS-FIT RESULTS

	F94	A15	DNS
$\alpha$	1	2.46	1
$\beta$	1	15.15	1
$\gamma$	0	1.77	-0.74

Note:  $H_{L,sp} = \alpha \bar{Q}_s$ ,  
 $H_{s,sp} = \beta \bar{Q}_s - (\alpha - \gamma) \bar{Q}_L$ ,  
and  $H_T = H_{int} + \beta \bar{Q}_s + \gamma \bar{Q}_L$

mines the accuracy of the final prediction of  $H_T$ , and  $\bar{Q}_s$  and  $\bar{Q}_L$  are calculated via spray’s microphysics (i.e.,  $\Delta T_p$  and  $\Delta r_p$ ). In the above discussion, we directly apply  $\Delta T_p$  and  $\Delta r_p$  from our DNS model to the bulk algorithms, so the next step is to examine the assumptions behind how bulk models quantify  $\bar{Q}_s$  and  $\bar{Q}_L$ .

#### 4.2.3 Spray evaporation in turbulent air and its temporal dependence

In bulk models, the evaporation for all spray droplets occurs with an assumed constant ambient condition (e.g., the 10-m temperature and  $RH$ ) that is usually drier and cooler than the lower part of the ASI, as we have shown in Sec. [2.3](#). In this section, we use the Lagrangian statistics of spray droplets in the DNS to investigate the characteristics of spray evaporation, specifically to test the behavior of  $\Delta T_p$  and  $\Delta r_p$  and compare with solutions given by constant ambient conditions as per bulk models.

### 4.2.3.1 Influence of spray timescales

We have illustrated three timescales involved in spray evaporation in turbulent air in Fig. 2.1: the residence time  $t_L$ , and the thermodynamic evolution timescales,  $\tau_T$  for temperature and  $\tau_r$  for radius. In this section, we will discuss how these timescales are associated with the relationship between the net differences  $\Delta T_p$  and  $\Delta r_p$  with  $t_L$ . In Fig. 4.6, we plot the joint probability density function (JPDF) of these quantities for droplets with  $r_p = 25, 75, \text{ and } 200 \mu\text{m}$  for  $Re_\tau=1500$ . Since all spray droplets in the DNS are initialized with same temperature and radius, the JPDFs in Fig. 4.6 are equivalent to the distributions of the re-entrance temperature and radius, which varies on spray initial size.

As seen in Fig. 4.6, the maximum of the residence time  $t_L$  (shown in vertical axes) decreases as the initial droplet size increases. This phenomenon is because both the settling velocity and inertial effects increase with  $r_p$ . We also find two qualitatively distinct types of distribution of spray temperature and radius change with  $t_L$  observed in Fig. 4.6. The first is a strong correlation between  $\Delta T_p$  or  $\Delta r_p$  and  $t_L$  (e.g. panels [b], [d], [e], and [f]), i.e., the longer the residence time, the greater magnitude in the change of spray temperature or radius. This relationship is similar in principle to what A15 assumes. The second type of distribution features a high-density area at small values of  $t_L$  and a much weaker correlation between  $\Delta T_p$  and  $t_L$  (e.g., panel [a]), while panel [c] appears to be a transition between the two. This is similar in principle to F94's assumption that spray immediately adjusts to the ambient air temperature, and it is observed that the high-density area is independent of residence time (parallel to the vertical axis). Therefore, only assuming one temporal relationship for spray temperature change does not appear to cover all scenarios for various spray sizes, and the various timescales associated with a droplet's thermodynamic evolution and lifetime should be carefully considered when parameterizing their radius and temperature change for use in bulk models.

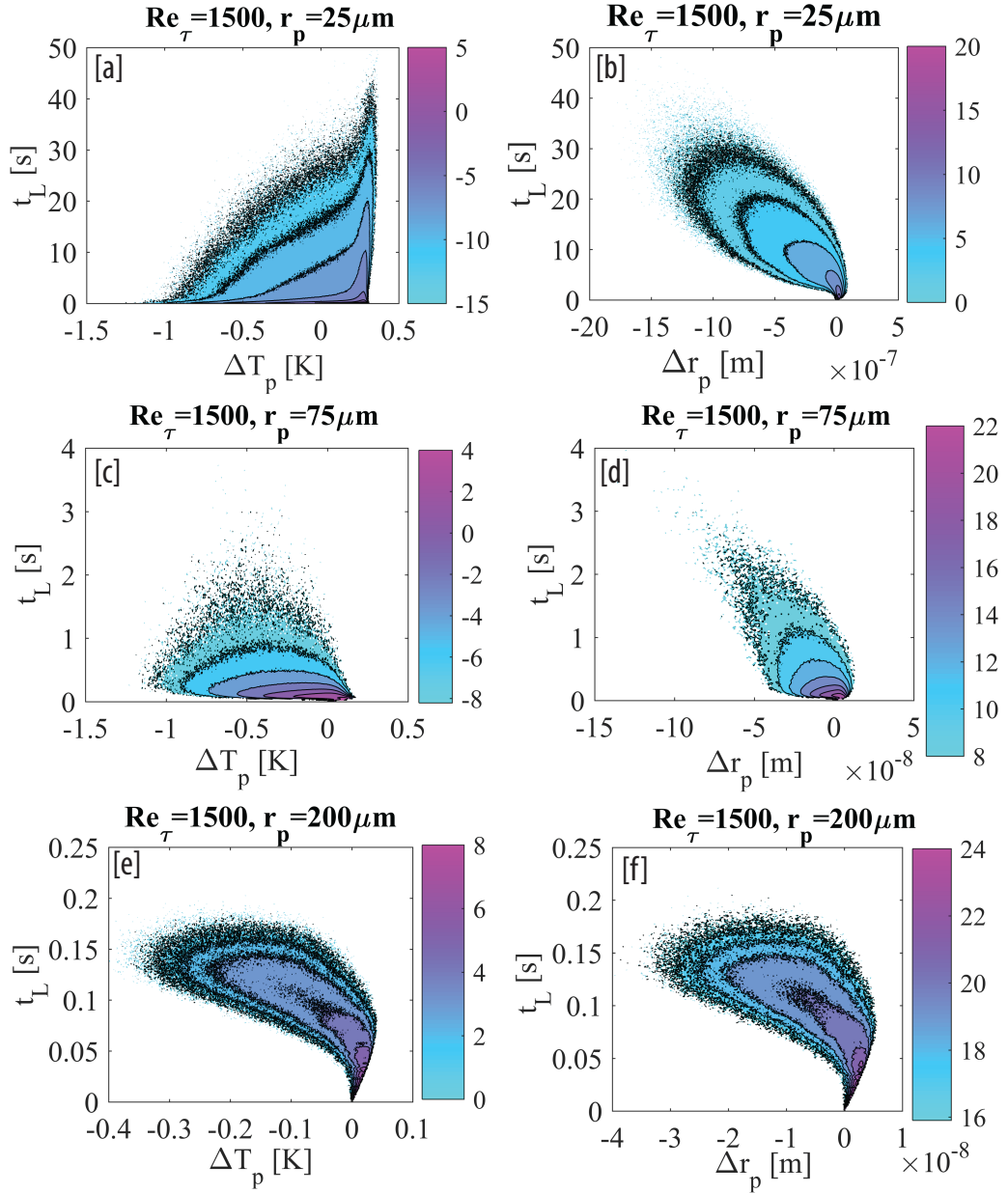


Figure 4.6. Joint PDFs of residence time ( $t_L$ ) and droplet temperature change ( $\Delta T_p$ , left column) and radius change ( $r_p$ , right column) at  $Re_\tau=1500$ . Three radii are presented:  $25\mu\text{m}$  (first row),  $75\mu\text{m}$  (second row),  $200\mu\text{m}$  (third row). Color bars represents the density of the JPDFs in log-scale.

How  $\Delta T_p$  and  $\Delta r_p$  are associated with  $t_L$  depends on their timescales  $\tau_T$  and  $\tau_r$ . Andreas (2005) defines  $\tau_T$  as the time required for changing to a factor of  $e^{-1}$  of the initial temperature. Thus,  $\tau_T$  is proportional to  $r_p^2$  since it is based on the exposed surface area for heat transfer. Based on Eqs. (2.8) and (2.10), one can notice that temperature and radius change are strongly correlated with time within  $\tau_T$  or  $\tau_r$  respectively (Andreas, 1992; Veron, 2015). For example, given the top boundary condition of M1 in Table 2.3,  $\tau_T$  for 25- $\mu\text{m}$  droplets is 7.3 ms, while  $\tau_r$  is 47 ms for 200  $\mu\text{m}$ . The response time for radius,  $\tau_r$ , is defined either by the  $e$ -folding time (used in the A15 model) or a linear decay rate (e.g. Lewis and Schwartz (2004)), and is also proportional to  $r_p^2$ . Thus, Fig. 4.6a shows an increased probability density concentrated at a specific temperature for all  $t_L$ , suggesting that the near-surface environment would play a dominant role governing the re-entrance temperature regardless of the residence time. In this scenario,  $t_L$  is not a good indicator for  $\Delta T_p$ .

As  $\tau_r$  is greater than  $\tau_T$  by three orders of magnitude (Andreas, 2005; Veron, 2015), radius change with the ambient air is a much slower process than temperature adjustment. Thus, we expect radius to present a strong correlation for a wide range of  $t_L$  because  $\tau_r > t_L$  for most droplets. For this reason, we select the shorter timescale  $\tau_T$  to non-dimensionalize  $t_L$  and define a non-dimensional timescale as

$$\tilde{t}_L = \frac{t_L}{\tau_T}. \quad (4.4)$$

By definition, if  $\tilde{t}_L \leq O(1)$ , the limiting timescale for the evaporation is the residence time  $t_L$ , and spray cannot finish the initial temperature adjustment and is less likely to experience a wide range of temperature and humidity, so  $\Delta T_p$  should retain a strong correlation with  $t_L$ . However, when  $\tilde{t}_L > O(1)$ , the limiting timescale is  $\tau_T$ , so spray tends to establish a new equilibrium with the ambient air.

Thus, if  $\tilde{t}_L > O(1)$ , using its initial conditions would lead errors in estimating the spray’s returning temperature based on its residence time given a stationary ambient condition, because spray will “forget” its initial state. For example, when F94 assumes that spray instantaneously adjusts to the air temperature at the representative location (the 10-m condition), we would expect a peak of  $\Delta T_p$  which is always clustered at negative values due to evaporative cooling. Figure 4.6[a] shows, however, that  $\Delta T_p$  in the high-density regions of the JPDFs for small droplets (especially for 25  $\mu\text{m}$ ) is positive, i.e., the spray is warmed due to condensation effect near surface. Therefore, given a different timescale balance, a model should distinguish the parameterizations of spray evaporation based on  $\tilde{t}_L$ .

As  $r_p$  increases, the ratio  $\tilde{t}_L$  decreases rapidly because  $\tau_T$  increases as  $r_p^2$  (as noted above), while  $t_L$  decreases due to an increased settling velocity and higher inertia. This suggests a sharp border between the high- and low-correlation scenarios, possibly simplifying proper modeling strategies.

#### 4.2.3.2 The ambient conditions of spray evaporation

While the JPDFs in Fig. 4.6 show two distinct types of relationship between  $t_L$  and  $\Delta T_p$  or  $\Delta r_p$ , bulk models still require specifications of the representative ambient conditions in order to predict the re-entrance radius and temperature accurately.

To further quantify the relationship between spray evaporation against its residence time, in Figs. 4.7 and 4.8 we plot the conditional mean (the expected value) of temperature and radius change given a residence time,  $E(\Delta T_p|t_L)$  and  $E(\Delta r_p|t_L)$ , for varying  $Re_\tau$  and  $r_p$ . We then compare the result with solutions which would have been retrieved from bulk models assuming a constant background ambient temperature and humidity (usually cooler and drier than the bottom surface). The idealized radius and temperature change with constant ambient background are given as curves “C1” to “C4” in the figures for different ambient conditions, with shading to repre-

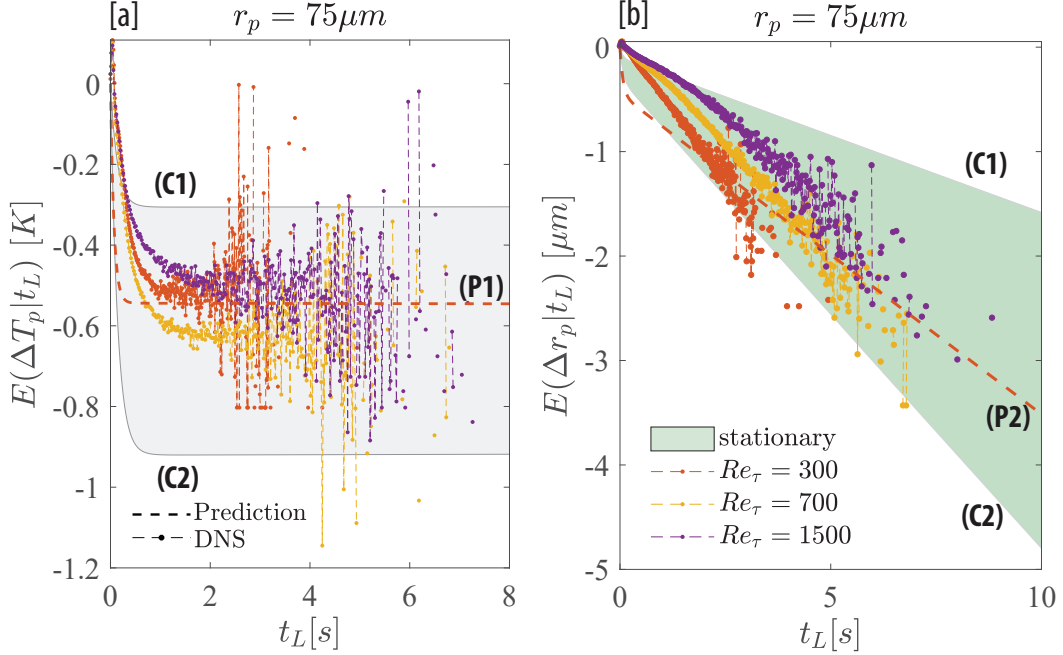


Figure 4.7. Conditional mean of temperature change ( $\Delta T_p$  [K]) and radius change ( $\Delta r_p$  [ $\mu\text{m}$ ]) given residence time ( $t_L$  [s]) for  $75\text{-}\mu\text{m}$  spray droplets. Shaded areas represent possible solutions of stationary evaporation (grey for  $\Delta T_p$  and green for  $\Delta r_p$ ) with limits from two assumed constant ambient conditions (C1 and C2): (C1)  $RH=97\%$ ,  $T_f=27.8^\circ\text{C}$ , and (C2)  $RH=95.5\%$ ,  $T_f=27.4^\circ\text{C}$ . Also included are prediction using Eq. (4.5) for specifying representative ambient conditions: (P1)  $RH=98.48\%$ ,  $T_f=27.35^\circ\text{C}$ , and (P2)  $RH=96.19\%$ ,  $T_f=26.85^\circ\text{C}$ .

sent conditions in between. Thus, in Figs. 4.7 and 4.8, if  $\Delta T_p$  and  $\Delta r_p$  given the residence time are well predicted by the bulk models, we would see them follow the solutions of spray evaporation given stationary ambient conditions.

In some scenarios, the statistical behavior of spray droplets in DNS agrees with what bulk models assume. For example, as seen in Fig. 4.7b, the evolution of radius change ( $\Delta r_p$ ) with lifetime is linear for almost all  $Re_\tau$ , which is qualitatively expected when assuming constant background conditions. This would indicate that the turbulent fluctuations felt by the droplets in the DNS in this scenario are substantially filtered out as  $\tilde{t}_L < O(1)$ . In other words, it is feasible find a possible single ambient

condition that the droplets have experienced to characterize spray’s radius change. Similarly, we also notice that the temporal evolution of  $\Delta T_p$  in Fig. 4.7a is in the range of possible steady-state solutions for spray droplets, at least for 75  $\mu\text{m}$  droplets since  $\tilde{t}_L$  is  $O(1)$  (curves lie within the gray shaded area).

On the other hand, droplets with  $\tilde{t}_L > O(1)$  have a different story (e.g.,  $\tilde{t}_L = 10.52$  for 25- $\mu\text{m}$  droplets), as seen in Fig. 4.8. The ambient conditions used for estimating the change in radius (C3 and C4) cannot apply to its temperature (C1 and C2), although the conditional mean  $\Delta T_p$  mostly follows some other stationary ambient conditions. In Fig. 4.8a, the condition C1 is the wet-bulb temperature at the bottom boundary, and C2 is the condition very close to the bottom boundary ( $RH = 98\%$ ). Neither of these causes spray to adjust to a cooler and drier ambient condition (resulting in negative  $\Delta T_p$ ) as F94 or A15 would expect. Instead, Fig. 4.8a shows a positive mean  $\Delta T_p$ , indicating that condensation occurs on these droplets (also shown in Figs. 4.2 and 4.1). This phenomenon is because of the immediate response of the droplet to the local ambient conditions before impacting the lower surface. Even though some spray may have spent most of its lifetime away from the bottom surface, its re-entrance temperature is predominately determined by the local condition due to the small  $\tau_T$  (i.e.,  $\tilde{t}_L > 1$ ). Therefore, the selection of ambient condition for assuming a constant background needs to incorporate the limiting timescale.

To summarize, our DNS results suggest that the balance of residence time and other timescales modifies the selection of representative ambient conditions when mean gradients of air temperature and humidity are present above the ASI. We observe drawbacks in both F94 and A15 in this regard, especially in predicting the re-entrance temperature. However, the results do not necessarily exclude the possibility of assuming stationary ambient conditions within bulk models. What is needed is a more accurate specification of these assumed conditions (i.e. not simply the 10-meter temperature and humidity).

Nevertheless, the question of how to specify this condition remains unanswered in real systems, and there are several necessary parameters of fluid and spray to consider. For example, as  $t_L$  increases, droplets with longer residence time experience slightly lower humidity as they are transported to a drier environment during their lifetime. Also, as  $Re_\tau$  increases in our simulations, the gradient of background temperature and humidity changes. Thus, the change in  $\Delta r_p$  with  $t_L$  behaves as though an assumed background ambient condition were becoming more humid. For example in Fig. 4.7b and 4.8b,  $\Delta r_p$  for  $Re_\tau = 300$  is nearer the C2 (or C4) line at 95% RH while  $Re_\tau = 1500$  is nearer the C1 (or C4) line at 97%.

#### 4.2.3.3 A tentative estimate of the equivalent ambient condition

Here we propose a simple, tentative estimate for these effective ambient conditions based on our DNS results. For heavy droplets (e.g. large spume droplets), spray’s evaporation is usually limited by the residence time ( $\tilde{t}_L < O(1)$ ), so both radius and temperature retain their correlation to the initial condition. Thus, we would assume the equivalent ambient conditions sit beneath the so-called “spray layer”  $z \in (0, \delta_{spray})$ , defined as the maximum height spray can reach (usually where spray concentrations are assumed uniform with height). In our DNS model, when spray exhibits inertial motions,  $\delta_{spray} = \delta_{inj}$  is the maximum height spray could reach without turbulent transport (shown in Table 2.2).

As  $\tilde{t}_L$  increases for smaller spray droplets,  $\delta_{spray}$  grows as droplets are transported more easily by turbulence across, and eventually reaches  $\delta_{spray} = \delta$ ; i.e., spray is distributed evenly across the domain (or perhaps the surface layer in real systems). Meanwhile, the surface conditions become more dominant as  $\tau_T$  decreases. Therefore, the assumed location to extract the equivalent ambient condition needs to be a function of the limiting timescales,  $\tau_T$  or  $\tau_r$ . Otherwise, it would lead to inaccurate predictions of  $\Delta T_p$  and  $\Delta r_p$ .

To improve this issue, we assume that spray droplets travel with a mean vertical settling velocity  $w_s$ , leading to the following expression for the height  $z_{evap}$  at which to extract the mean ambient conditions:

$$z_{evap,\phi} = \frac{1}{2} \min(\delta_{spray}, w_s \tau_\phi), \quad (4.5)$$

where  $\delta_{spray}$  is the height of the spray layer (when  $\tilde{t}_L \gg 1$ , it is assumed to be the height of the domain of interest), and  $\tau_\phi$  represents timescales for  $\phi = r_p, T_p$ . Then, the constant ambient conditions for temperature and humidity to be used in the bulk models would be  $T_a(z_{evap,\phi})$  and  $RH_a(z_{evap,\phi})$ , where  $T_a$  and  $RH_a$  are the mean ambient air temperature and relative humidity.

For instance, we plot solutions based on the ambient condition predicted by Eq. (4.5) in Figs. 4.7 and 4.8 (“P1” for  $\Delta T_p$  and “P2” for  $\Delta r_p$  in both figures), where we assume  $z_{evap,T} = 0$  and  $z_{evap,r} = \frac{1}{2}\delta$  for 25  $\mu\text{m}$  droplets and  $z_{evap,T} = \frac{1}{4}\delta_{inj}$  and  $z_{evap,r} = 0.3\delta$  for 75  $\mu\text{m}$  droplets. Although this estimation is only based on the hypothesis of the one-way coupling, we find that Eq. (4.5) overall provides a reasonable ambient condition for both cases and can significantly improve the error for  $\Delta T_p$  (hence  $\bar{Q}_s$ ) for the smaller spray with  $\tilde{t}_L > O(1)$  than the conventional assumption.

#### 4.2.4 The importance of spray timescales on estimating spray feedback

Different treatments of spray heat flux in bulk models cause significant differences in predicting the influence of the spray and thus the total heat flux. For example, when applying both F94 and Andreas and Decosmo (1999) (a predecessor of the A15 model with same framework) to hurricane models (Wang et al., 2001), it is reported that the F94 model results in an increase by 8% of the intensity of the tropical cyclone, while A15 gives an increase by 25% and generates a physically unrealistic

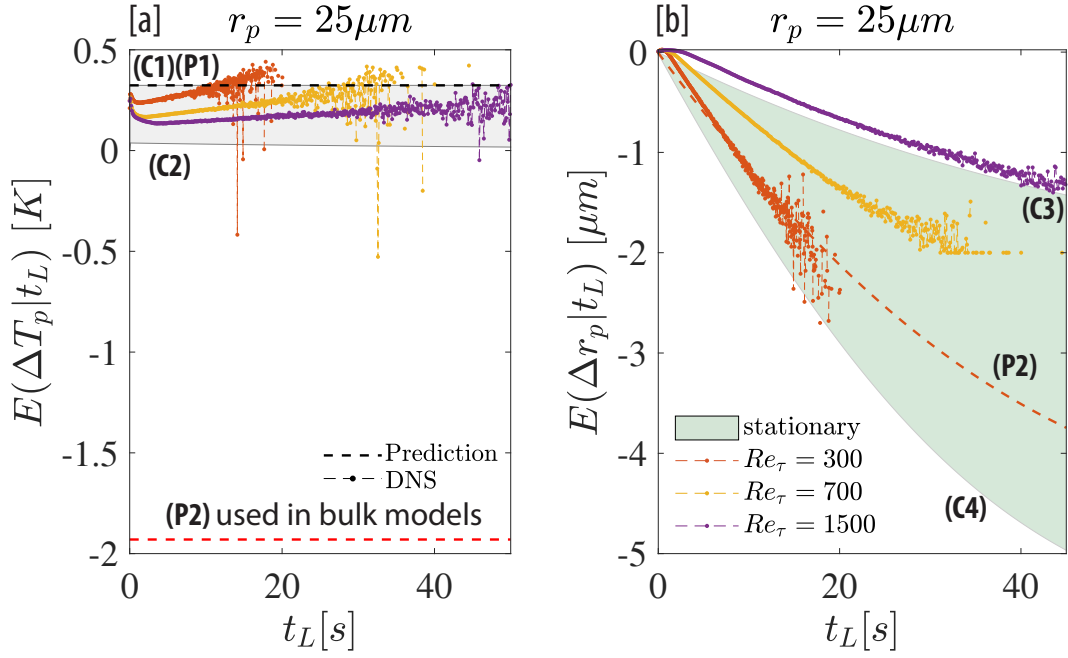


Figure 4.8. Conditional mean (expectation) and predictions of [a] temperature change ( $\Delta T_p$  [K]), and [b] radius change ( $\Delta r_p$  [ $\mu\text{m}$ ]) given residence time ( $t_L$  [s]) for 25- $\mu\text{m}$  spray droplets. The predictions (dashed lines) with equivalent ambient conditions are given by Eq. (4.5). The ambient conditions used for temperature are different from radius: (C1) & (P1) the quasi-equilibrium evaporation temperature of the spray at  $RH=100\%$ ,  $T_f=28^\circ\text{C}$ , (C2)  $RH=98\%$ ,  $T_f=28^\circ\text{C}$ , (C3)  $RH=98\%$ ,  $T_f=27.8^\circ\text{C}$ , (C4)  $RH=95\%$ ,  $T_f=27.4^\circ\text{C}$ , (P2)  $RH=95.74\%$ ,  $T_f=26.35^\circ\text{C}$

near-core environment. Previous discussions suggest that spray timescales are the key to accurately quantify the spray-mediated fluxes. Thus, in this section, we revisit the bulk estimations of total heat flux  $H_T$  and discuss the influence of spray timescales on estimating spray feedback.

We have shown in PR17 that two types of cancellation were identified in a turbulent system with evaporating spray droplets: one between spray-mediated sensible and latent heat fluxes, and the other between spray-mediated and turbulent (i.e. interfacial) heat fluxes. These cancellation effects prevent the spray droplets from enhancing the total heat flux without constraint. However, in their bulk models, F94 does not include an explicit form of the feedback effect on the interfacial heat flux, while A15 predicts this feedback effect as positive by stating that  $\gamma > 0$  due to the assumption that spray cools the surface air. We have mentioned that both formulations would overestimate the influence of spray droplets.

As spray evaporation induces a change in the total heat flux  $H_T$ , we define the change of total heat flux,  $\Delta H_T$ , as the difference between the spray-laden and unladen cases:  $\Delta H_T = H_T - H_{T,0}$ . With bulk estimates, we can connect  $\Delta H_T$  with the net change of spray's temperature and radius directly. Combining this with Eqs. (2.25) and (2.26), one gets

$$\Delta H_T \approx \bar{Q}_s + \gamma \bar{Q}_L, \quad (4.6)$$

with  $\gamma < 0$ , which relates  $\Delta H_T$  to the nominal spray-mediated heat fluxes,  $\bar{Q}_s$  and  $\bar{Q}_L$ . Since  $\bar{Q}_s$  and  $\bar{Q}_L$  are defined as proportional to  $\Delta T_p$  and  $\Delta r_p^3$ ,  $\Delta H_T$  can be approximated as a linear function of  $\Delta T_p$  and  $\Delta r_p^3$  given a specific spray generation rate  $F$ . Therefore in principal, one can predict the change of total heat flux based on the temperature and radius of the re-entering spray. Based on the previous discussion on  $\Delta T_p$  and  $\Delta r_p$ , we have two major scenarios for spray feedback effects.

The first scenario occurs for spray with  $r_p > 50\mu m$  when spray evaporation is limited by its residence time (e.g. spume drops), i.e.,  $\tilde{t}_L \ll 1$ , where we expect

$\bar{Q}_s > \bar{Q}_L > 0$  as the radius change is small (cf. Fig. 4.7), and thus  $\Delta H_T > 0$ . Note in Fig. 4.2 that we confirm that  $\bar{Q}_s$  is a good estimate for the total spray-mediated heat flux  $H_{sp}$ , so we expect  $\bar{Q}_s > \bar{Q}_L$ . Therefore, spray in this regime enhances  $H_T$ , and the enhancement grows with the generation rate.

In Fig. 4.9, we plot the relative modification of total heat flux ( $\Delta H_T/H_{T,0}$ ) for different  $Re_\tau$  and  $\Phi_m$  with respect to droplet size  $r_p$ . We observe a low sensitivity of  $\Delta H_T$  to  $Re_\tau$  but a fairly high sensitivity to  $\Phi_m$ , and the enhancements of  $\Delta H_T$  by 75 $\mu\text{m}$  and 200 $\mu\text{m}$  droplets in Fig. 4.9 demonstrate the potential of the enhancement of  $H_T$  by spray with  $\tilde{t}_L \ll 1$ , especially under high spray-generation rate  $F$ . In addition,  $-\gamma\bar{Q}_L$  is very small because  $\Delta r_p$  is small, so the interfacial feedback is insignificant in this scenario. Thus, the framework that F94 presents (with no negative feedback term) can physically represent  $H_T$  for spray with  $\tilde{t}_L \ll 1$ .

The second scenario occurs when the residence time no longer limits spray's temperature adjustment, i.e.,  $\tilde{t}_L > 1$ . Fig. 4.8 indicates that  $\bar{Q}_L < \bar{Q}_s < 0$  at the bottom surface, i.e., small droplets condense near the surface (cf. Fig. 4.6), which is not considered in most bulk and 1-D models. In addition, the combination of  $\bar{Q}_s$  and  $\bar{Q}_L$  makes  $\Delta H_T/H_{T,0} \leq O(0.01)$  as one can see in Fig. 4.9. We also observe that as the mass fraction increases by a factor of 10 (solid lines vs. diamonds in Fig. 4.9), 25  $\mu\text{m}$  droplets show an overall insensitivity to  $\Phi_m$ . Based on Eqs. (2.31) and (2.30), the insensitivity on mass fraction indicates that  $\bar{Q}_s$  and  $\bar{Q}_L$  would be less dependent on the spray generation rate in real systems. Since there is a weak dependence on  $Re_\tau$  for  $\Delta H_T$  in Fig. 4.9, we argue that the dominant influence on  $\bar{Q}_L$  and  $\bar{Q}_s$  for 25  $\mu\text{m}$  or smaller droplets is the local boundary condition when spray re-enters the bottom surface. Therefore, the discrepancy of the spray modification on the total heat flux between DNS and bulk models comes from the direction of the latent heat flux at the bottom surface.

Although the condensation effect that is determined by the boundary condition

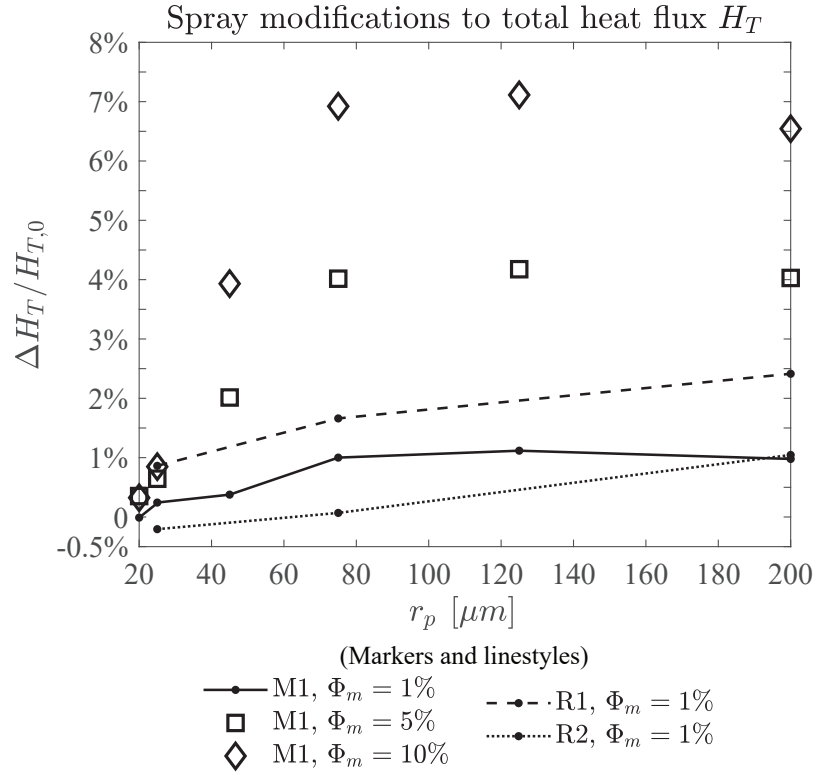


Figure 4.9. Modification of total heat fluxes  $H_T$  of different initial spray radii  $r_p$  compared with no-spray scenario for each  $Re_\tau$  with same boundary conditions indicated in Table 2.3. “M1” has  $Re_\tau = 300$ , “R1” has  $Re_\tau = 700$ , and “R2” has  $Re_\tau = 1500$ , and markers specify the spray mass fraction.

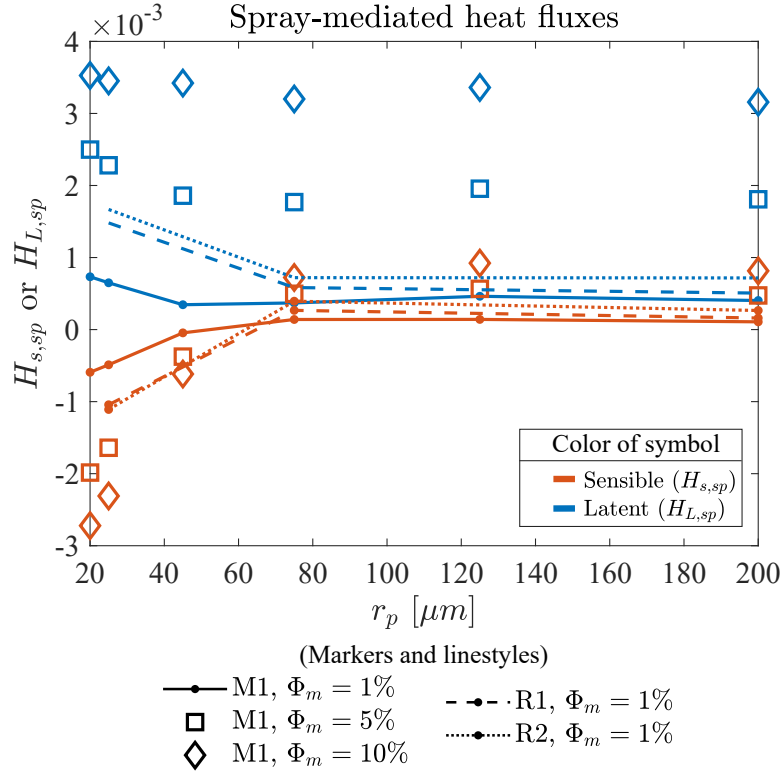


Figure 4.10. Spray-mediated sensible ( $H_{s,sp}$ ) and latent ( $H_{L,sp}$ ) fluxes averaged in the spray layer  $z \in [0, \delta_{inj}]$ . The heat fluxes are normalized by  $u_\tau \Delta h$ . Colors specify the sensible or latent components, and line and marker styles are same as Fig. 4.9.

sounds counter-intuitive, the fact that small droplets can condense ( $\bar{Q}_L < 0$  thus  $H_{L,sp} < 0$ ) near the bottom surface does not conflict with their potential to evaporate hence increase the local humidity and decrease evaporation away from the surface. In fact, the two phenomena are consistent if one can interpret the timescales of spray properly per their corresponding ambient conditions, although we only focus on the bulk models at the bottom surface in the current study.

For the lower part of the domain ( $z \in [0, \frac{1}{8}\delta]$ ), we plot in Fig. 4.10 the averaged spray-mediated sensible and latent heat fluxes computed by DNS,  $H_{s,sp}$  and  $H_{L,sp}$ . The DNS heat fluxes are normalized by the product of friction velocity ( $u_\tau$ ) and total enthalpy difference ( $\Delta h = h_{bot} - h_{top}$ ) between the top and bottom boundaries respectively. The positive spray-mediated latent heat flux  $H_{L,sp}$  in Fig. 4.10 represents an upward latent heat flux from spray evaporation. For the sensible heat flux  $H_{s,sp}$ , we find that spray with  $r_p < O(50\mu m)$  has a sensible heat flux  $H_{s,sp}$  with opposite sign to the latent flux, which indicates that the evaporative cooling effect cancels out the latent heat flux released from the spray. This leads to a smaller estimation of  $\bar{Q}_s$  than the estimate without considering cancellation and thus yields the limited enhancement in Fig. 4.9. Spray with  $r_p > O(50\mu m)$ , instead, has positive  $H_{s,sp}$  and cannot cancel  $H_{L,sp}$ , which results in a larger value of  $\bar{Q}_s$  and thus has a net positive contribution to the total heat flux that is discussed in sect. 4.24.2.3.

Whether or not the spray exhibits this cancellation of spray-mediated fluxes depends on its timescales. The quick adjustment to the fluctuating temperature and humidity by spray allows the spray to reach the equilibrium temperature at a highly localized position (e.g. PR17). Here, as we can see from Fig. 4.10, cancellation occurs when  $\tilde{t}_L > O(1)$  when spray is away from surface. At the bottom surface, the cancellation effect still occurs as we have seen in Fig. 4.1 since  $H_{s,sp}$  and  $H_{L,sp}$  have different signs. Therefore, from both perspectives, the cancellation effect or the condensation at the surface, show that bulk model can overestimate the spray-mediated

heat fluxes.

To summarize, timescales of spray play an important role in predicting the total heat flux besides spray-mediated heat fluxes based on Eq. (4.6), which needs be incorporated in bulk models. As a result, the bulk estimation could have better parameterizations of  $\Delta T_p$  and  $\Delta r_p$ , and the influence of spray, in particular given its different dependence on  $\tilde{t}_L$ , can be better understood.

### 4.3 Summary

In this study, we investigate how total heat flux responds to sea-spray via high-resolution Eulerian-Lagrangian simulations, where we use DNS to represent turbulent airflow in the lower atmospheric boundary layer at the air-sea interface with neutral stability. We apply the principles from air-sea bulk models that estimate total heat transfer from the water surface and compare to our DNS results. Under our current idealized settings, we find spray might not necessarily enhance the total heat flux in turbulent flow with constant vertical heat flux. Also, the current study suggests the importance of spray timescales on parameterization of spray-mediated heat fluxes. We find a non-monotonic relationship between spray's enhancement to the total heat flux and its residence time so that models like F94 and A15 can overestimate the influence of spray droplets for several reasons.

First, previous understanding of the feedback mechanisms of spray is not complete. Our DNS results suggest that the total heat flux cannot always be expressed as the sum of an interfacial and a spray mediated component directly, especially for droplets with small size (e.g.,  $r_p \leq 25\mu m$ ). We find an additional negative feedback mechanism for total interfacial heat flux that is proportional to the spray-mediated heat flux at the surface (negative  $\gamma$  term in Eq. (4.1)). This negative feedback effect limits the overall influence of spray regarding the total heat flux from the water surface, which is not included in either F94 or A15. In particular, A15 argues that

spray-mediated latent heat flux would insert positive feedback to the total heat flux, which is not observed in our DNS results (see Table 4.1 for a comparison). Therefore, we would suggest further implementation on the negative feedback effects and investigations on its tuning coefficient for bulk models in practical use.

Second, inaccurate estimates of spray evaporation could also cause bulk models to fail to capture the cancellation effect between spray sensible and latent heat flux for smaller droplets. The failure is due to the different timescales involved in droplet evaporation when evaluating the spray evaporation via assumed-stationary ambient solutions, particularly when the droplet experiences a wide range of environmental conditions during its lifetime.

We find that the balance between the residence time and temperature response time of spray ( $\tilde{t}_L$ ) is a good indicator for determining whether or not a stationary ambient condition can be assumed for the droplet. When the residence time is longer than temperature timescales,  $\tilde{t}_L > O(1)$ , the re-entrance temperature and radius of spray lose their correlation with the initial condition, and are determined by the local condition at the water surface. Therefore, the assumption that spray re-enters the water surface with substantially decreased temperature (e.g., ones determined by 10-m conditions) would not apply and would introduce further over-estimations to the spray-mediated sensible heat flux.

When the residence time is shorter than the correlation timescales of evaporation, i.e.,  $\tilde{t}_L < O(1)$ , spray retains a correlation with its initial condition. Therefore,  $\Delta T_p$  and  $\Delta r_p$  follows the solutions with an assumed-stationary ambient condition like bulk models. As a consequence, spray in this regime has the potential to enhance the total heat flux, and the enhancement will be magnified by higher generation rates. However, the equivalent ambient condition is not uniform but a function of spray timescales and is related to  $\tilde{t}_L$ . Since the spray temperature response time  $\tau_T \approx 10^{-3}\tau_r$ , further assumptions are required for bulk models to approximate the

equivalent ambient for re-entrance temperature and radius, and we propose an estimate of the equivalent ambient condition in Eq. (4.5) based on our DNS results.

Although our idealized study contains many simplifications regarding the surface processes (especially those associated with waves, such as wave-breaking, droplet formation, etc.) and atmospheric variability, this study provides clear evidence that the spray effects are dependent on their thermodynamic timescales, and highlights physical processes (e.g. feedback) that are not properly accounted for in bulk models. Therefore, given a reasonable assumption for residence times across all sizes of spray, one could potentially improve the prediction of the total heat flux via bulk models without further complicating the model itself.

## CHAPTER 5

### FEEDBACK IN THE POLY-DISPERSED SYSTEM

#### 5.1 Introduction

In previous chapters, the investigations on spray effects have focused on the specific spray properties on the heat fluxes. We have learned that how spray droplets evaporate and interact with turbulence is different based on the ratio between their residence time and thermal timescales. However, in conventional spray models, contributions from each size of droplets are usually summed up directly, which implicitly assumes no interaction between droplets of different sizes. Whether or not neglecting this kind of interaction between different droplet sizes is eligible is not yet answered when the interactions between droplets become significant. In particular, we are concerned whether or not assuming droplets are independent could impede the quality of bulk-model estimations. In this chapter, we focus on the effects of sea-spray droplets with multiple sizes and assess this fundamental assumption on treating each droplet as an independent source.

##### 5.1.1 Background

Spray droplets are generated with a wide range of sizes. The distribution of the spray sizes is usually expressed by a size-distribution function to represent the concentration of droplets generated given a size range. In practice, the size-distribution is converted to a sea-spray generation function (SSGF), which yields the number flux of droplets generated per incremental size at the ocean surface (Veron, 2015). SSGF

is usually parameterized by wind speeds or whitecap fraction empirically due to the difficulties in the direct measurements of the number flux. In particular, the SSGF on larger droplets (e.g., spume droplets with radius peaked at 100  $\mu\text{m}$  but extended to more than 2000  $\mu\text{m}$ ) is still under debate. For example, difference relationships of SSGF on the droplet initial size  $r_0$  are reported in [Ortiz-Suslow et al. \(2016\)](#); [Veron et al. \(2012\)](#).

A safer approach is to assume the influence of spray is independent of the size distribution, considering the uncertainty in SSGFs. In other words, the contribution from a specific size does not affect droplets in other sizes. For example, in a bulk model (e.g. [Andreas and Mahrt \(2015\)](#)), the nominal sensible heat flux mediated by spray ( $\bar{Q}_{s,sp}$ ) can be written as,

$$\bar{Q}_{s,sp} = \int_{r_1}^{r_2} q(r_0) \frac{dF}{dr_0} dr_0 \quad (5.1)$$

where  $r_1$  and  $r_2$  are the size limit considered in a model,  $q(r_0)$  represents the heat contributed from droplets with the initial size  $r_0$ , and  $\frac{dF}{dr_0}$  is the SSGF. For example, in the bulk spray models of [Fairall et al. \(1994\)](#) and [Andreas et al. \(2015\)](#),  $q(r_0)$  is calculated *a priori* separately based on the hypothesis on spray evaporation regardless of the SSGF. A similar treatment is also applied to the Lagrangian models by [Edson and Fairall \(1994\)](#); [Mueller and Veron \(2014a,b\)](#); [Troitskaya et al. \(2018b\)](#), where the total effect is the sum of the contributions from each size together for a wide range of spray droplets.

By assuming droplets have independent influences, many Eulerian or Eulerian-Lagrangian studies only consider mono-dispersed spray droplets to simplify the investigation on the sensitivity of the air-sea fluxes from a specific spray size (e.g., [Helgans and Richter \(2016\)](#); [Peng and Richter \(2017, 2019\)](#); [Rastigejev and Suslov \(2019, 2016\)](#); [Richter and Sullivan \(2014\)](#); [Richter et al. \(2016a\)](#)). In fact, only a few

studies, in particular with an Eulerian-Lagrangian framework, consider spray with more than one size coupled with the air phase. For example, a poly-dispersed size distribution is considered in Richter et al. (2016b) to evaluate the momentum coupling. For the thermal influence, Edson et al. (1996) uses a 2-D Eulerian-Lagrangian model to simulate the influence of spray droplets on the atmospheric boundary layer with a  $k - \epsilon$  turbulence closure. However, assessments on the influence between droplet sizes using a high-fidelity model are merely found, which leaves another kind of uncertainties in addition to the strong assumption on droplet microphysics.

In Ch. 3, we discover that the role of droplets vary with different droplet sizes, and we also found that the feedback effects become stronger when the mass fraction increases. Thus, in this chapter, we assume that the interaction between spray droplets depends on both the mass fraction and size of spray droplets.

Nevertheless, in an operational model where spray effects are parameterized, considering multiple size is indeed a difficult task for large-scale numerical models such as Bao et al. (2011) and Chen et al. (2013). To simplify the computation, Andreas et al. (2008, 2015) put forward the concept of a representative size for sensible and latent heat fluxes to simplify the computation procedures. In his studies, the representative size are selected *a posteriori* from the size where droplets contribute most sensible and latent heat flux. In Eq. (5.1), this idea is equivalent to looking for the maximum of  $q(r_0) \frac{dF}{dr_0}$ , the contribution from a single droplet multiplied with its generation strength (SSGF, represented by  $\frac{dF}{dr_0}$ ). By using a stochastic Lagrangian model, this concept was qualitatively demonstrated by Mueller and Veron (2014b) (c.f. Fig. 6), but the peak changes accordingly to different SSGFs selected. Hence, how to select the characteristic size still remains obscure, and the limitation of using a single characteristic size needs to be identified.

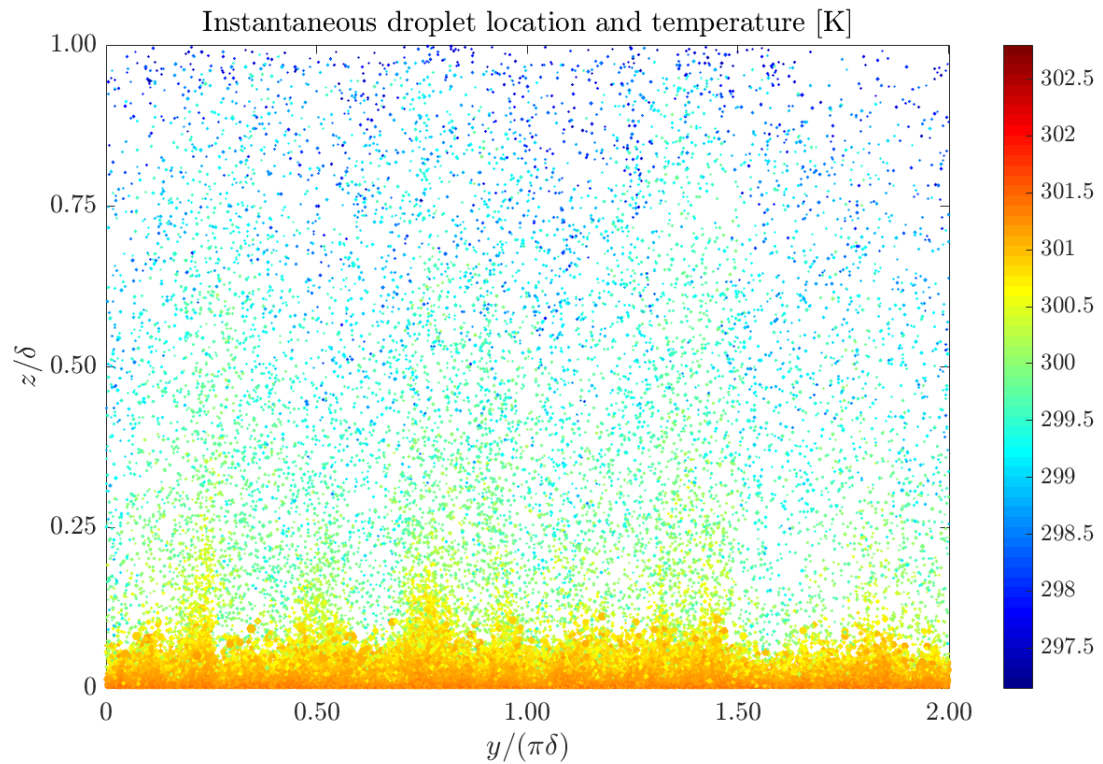


Figure 5.1. Instantaneous temperature and location of droplets (projection from  $x$ -axis, i.e. the stream-wise direction). Mass fraction is here 5%, and half of droplets are plotted for a schematic. Color represents the droplet temperature, and the size of dots is scaled by the instantaneous droplet radius.

### 5.1.2 Goals of this chapter

In this chapter, we continue to take advantage of the Eulerian-Lagrangian framework with direct numerical simulations (DNS) to resolve the evaporating spray droplets poly-dispersed in turbulent air. While spray droplets of multiple sizes are computed individually, their thermal influences from spray are two-way coupled with the air phase via the governing equations (c.f. Eqs. (2.2) and (2.3) for the expressions and Fig. 5.1 for a schematic).

The first group of questions discussed in this chapter is the feasibility of the superposition of the fields of air temperature, humidity, and heat fluxes from mono-dispersed cases to make up a poly-dispersed case. To simplify the scenario, we implemented bi-dispersed simulations of different combinations of droplet sizes, and these bi-dispersed cases are compared with the corresponding mono-dispersed cases for the same mass fraction in each component. Droplet sizes are chosen based on different regimes of non-dimensional residence time ( $\tilde{t}_L = \frac{t_L}{\tau_T}$ ) defined in Ch. 4. Thus, from this set of experiments, we also look into how droplets interact with others in a different size class.

Following the idealized simulations of multiple spray sizes, poly-dispersed droplet concentration distributions are evaluated. Specifically, our goal is to test whether feasible one can add the spray-mediated heat fluxes directly in a bulk model and to find a reasonable method to calculate the representative size.

For the feasibility of bulk spray estimations on two-way coupled poly-dispersed simulations, we estimated the individual spray-mediated fluxes related to each size class using the bulk model and the statistics sampled from DNS, and compare with the corresponding DNS values directly computed in the DNS solver. Thus, a direct one-on-one comparison shows the size regimes where the bulk model succeeds. Moreover, we also compare the total heat flux ( $H_T$ ) computed from DNS and the improved bulk model (e.g., Eq. (4.3) in Ch. 4) to assess the underlying hypothesis of the spray heat

fluxes used in all bulk models.

For the representative size, we consider three representative sizes averaged by its radius, surface area, and volume. We compare the poly-dispersed simulation with the mono-dispersed cases with representative size. Specifically, we assess the mean temperature and humidity of the carrier air and the vertical profiles of mean spray-mediated and turbulent heat fluxes.

### 5.1.3 Simulation configurations

The framework of the methodology in this chapter is consistent with previous chapters and is discussed in Ch. 2, where the difference is the change in droplet size class ( $N_{r_0}$ ). Since only one-way coupling is considered for the momentum coupling in the current study, the settling effect and number concentration of droplets in each class are identical to the mono-dispersed cases. In other words, the statistics of droplets such as the mean droplet velocity, the rate of being reintroduced to the system per droplets as well as the residence time remains the same for each size class, and so does the mean flow velocity. For example, Fig. 5.2 shows normalized droplet number concentration for selected radii from 20 to 200  $\mu\text{m}$ , which is supposed to be applied for the same size in all simulations regardless of the size distribution. In this chapter, both simplified droplet size configurations and full-spectrum SSGF are considered. Details of the size distributions are described in the corresponding sections.

### 5.1.4 Partitioning spray-mediated fluxes by size

The goal of this chapter is to assess the assumptions in the bulk spray model regarding poly-dispersity, so we compute the components of spray-mediated heat fluxes by spray size. To do so, Eqs. (2.11) to (2.14) are expanded based on a specific spray size class, so that spray-mediated heat flux in Eqs. (2.21) and (2.22) can be

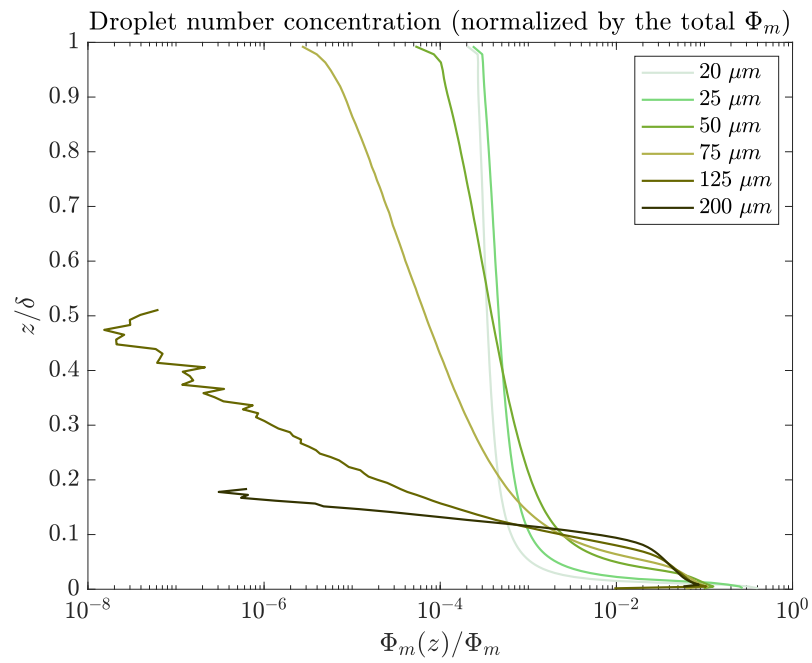


Figure 5.2. Normalized droplet mass concentration. For each curve, the total mass fraction  $\Phi_m$  is same. Legends show the initial size of droplets ( $r_0$ ).

written as

$$H_{s,sp} = \sum_{i=1}^{N_{r_0}} H_{s,sp}(r_{0,i}) = \sum_{i=1}^{N_{r_0}} \left[ - \int_0^z S^h(r_{0,i}) dz \right], \quad (5.2)$$

where  $H_{s,sp}(r_{0,i})$  is the spray-mediated sensible heat flux computed by DNS for droplets with an initial size  $(r_{0,i})$  based on Eqs. (2.12) and (2.14). Similarly, the latent spray-mediated heat flux can be computed as:

$$H_{L,sp} = \sum_{i=1}^{N_{r_0}} H_{L,sp}(r_{0,i}) = \sum_{i=1}^{N_{r_0}} \left[ - \int_0^z S^q(r_{0,i}) dz \right]. \quad (5.3)$$

Correspondingly, one can also calculate the components of bulk estimates of spray exchange rate of the sensible and latent heat (the nominal fluxes) in Table 2.4 that are denoted as  $\bar{Q}_s$  and  $\bar{Q}_L$ , so that

$$\bar{Q}_s = \sum_{i=1}^{N_{r_0}} \bar{Q}_s(r_{0,i}) = \sum_{i=1}^{N_{r_0}} -c_p m_{p,i} \Delta T_{p,i} (F_i/A), \quad (5.4)$$

and

$$\bar{Q}_L = \sum_{i=1}^{N_{r_0}} \bar{Q}_L(r_{0,i}) = \sum_{i=1}^{N_{r_0}} -L_v \Delta m_{p,i} (F_i/A), \quad (5.5)$$

where  $\bar{Q}_s(r_{0,i})$  and  $\bar{Q}_L(r_{0,i})$  are the components from droplets with the size class  $i$ , the subscript “ $i$ ” represents the droplet size class.

Therefore, the bulk estimates (“F94” in Table 4.1) based to the spray-mediated heat fluxes for each size class “ $i$ ” can be written as:

$$\hat{H}_{s,sp}(r_{0,i}) = \bar{Q}_s(r_{0,i}) - \bar{Q}_L(r_{0,i}), \quad (5.6)$$

and

$$\hat{H}_{L,sp}(r_{0,i}) = \bar{Q}_L(r_{0,i}), \quad (5.7)$$

where the hat on  $\hat{H}$  denotes the bulk-estimated values of heat fluxes comparing with

the corresponding one with DNS calculated values.

## 5.2 Bi-dispersed cases: A test on the superposition of mono-dispersed distributions

### 5.2.1 Bi-dispersed droplet size distribution

In this section, we present results from bi-dispersed simulation, where only two sizes are considered in a simulation. We then compare the bi-dispersed cases with the corresponding mono-dispersed simulations of the components of each bi-dispersed simulations. We select three droplet sizes from different timescale ratios shown in Fig. 5.12(b), which are  $25 \mu\text{m}$ ,  $50 \mu\text{m}$ , and  $200 \mu\text{m}$ . The three radii represent the small, medium, and large spray droplets, which give the ratio  $\tilde{t}_L = t_L/\tau_T$  in a decreasing order of  $O(10)$ ,  $O(1)$ , and  $O(0.1)$  respectively. For each combination, three total mass fractions  $\Phi_m$  of 1%, 5%, and 10% are considered. The details are listed in Table 5.1.

Since the size of droplets plays a vital important role in determining their feedback effects in turbulence, in this section, we focus on the potential consequence that droplets influence the other size via modification of air humidity and temperature. First, we test the vertical profiles of the temperature and humidity fields as well as heat fluxes directly computed in DNS and compare the results with the mono-dispersed case. Then, we apply the bulk estimation to the bi-dispersed simulations. We select a relatively high mass fraction at  $\Phi_m = 5\%$  as a benchmark level to present results in this chapter for the strength of spray effects.

### 5.2.2 Responses in air temperature and humidity

To begin with, we compare the response of air temperature ( $T_f$ ) and relative humidity ( $RH$ ) to the bi-dispersed cases and corresponding mono-dispersed cases, where each corresponding mono-dispersed case has half the initial mass of those in bi-dispersed simulations. In Fig. 5.3 the results are plotted in red solid lines (with

TABLE 5.1

## BI-DISPERSED CASES

Group	$r_{0,1}$ [ $\mu\text{m}$ ]	$r_{0,2}$ [ $\mu\text{m}$ ]	$\Phi_{m,1}/\Phi_m$	$\Phi_{m,2}/\Phi_m$	$\Phi_m$
S+M	25	50	50%	50%	
S+L	25	200	50%	50%	1%,5%,10%
M+L	50	200	50%	50%	

Note:  $\Phi_{m,1} + \Phi_{m,2} = \Phi_m$ .

legend “mixed”), while dashed lines represent the mono-dispersed simulation.

In Fig. 5.3, one observes that the temperature and the relative humidity are dominated by the small droplets when they are present. These small droplets cool and humidify the ambient air (the right column). This response is in accordance with the finding in Ch. 3 that smaller droplets are more efficient in modifying the ambient field due to the shorter thermal response time for evaporation. In contrast, the modification of medium (50  $\mu\text{m}$ ) and large droplets on the temperature is not as significant as smaller droplets, and air tends to be slightly warmed by these droplets (third row), and the warmed air slightly decreases the  $RH$  near the lower boundary where large droplets reside.

One also notices that, in Fig. 5.3, the temperature and humidity of a bi-dispersed case can be made by simply adding the differences between the temperature of each component and the unladen case to the unladen case, i.e.

$$\langle T_f^{(s.p.)} \rangle = \langle T_{f,0} \rangle + \sum_{i=1}^{N_{r_0}} \{ \langle T_{f,i} \rangle - \langle T_{f,0} \rangle \}, \quad (5.8)$$

where  $N_{r_0} = 2$ , and subscript ‘0’ represents the unladen case, and the angular bracket

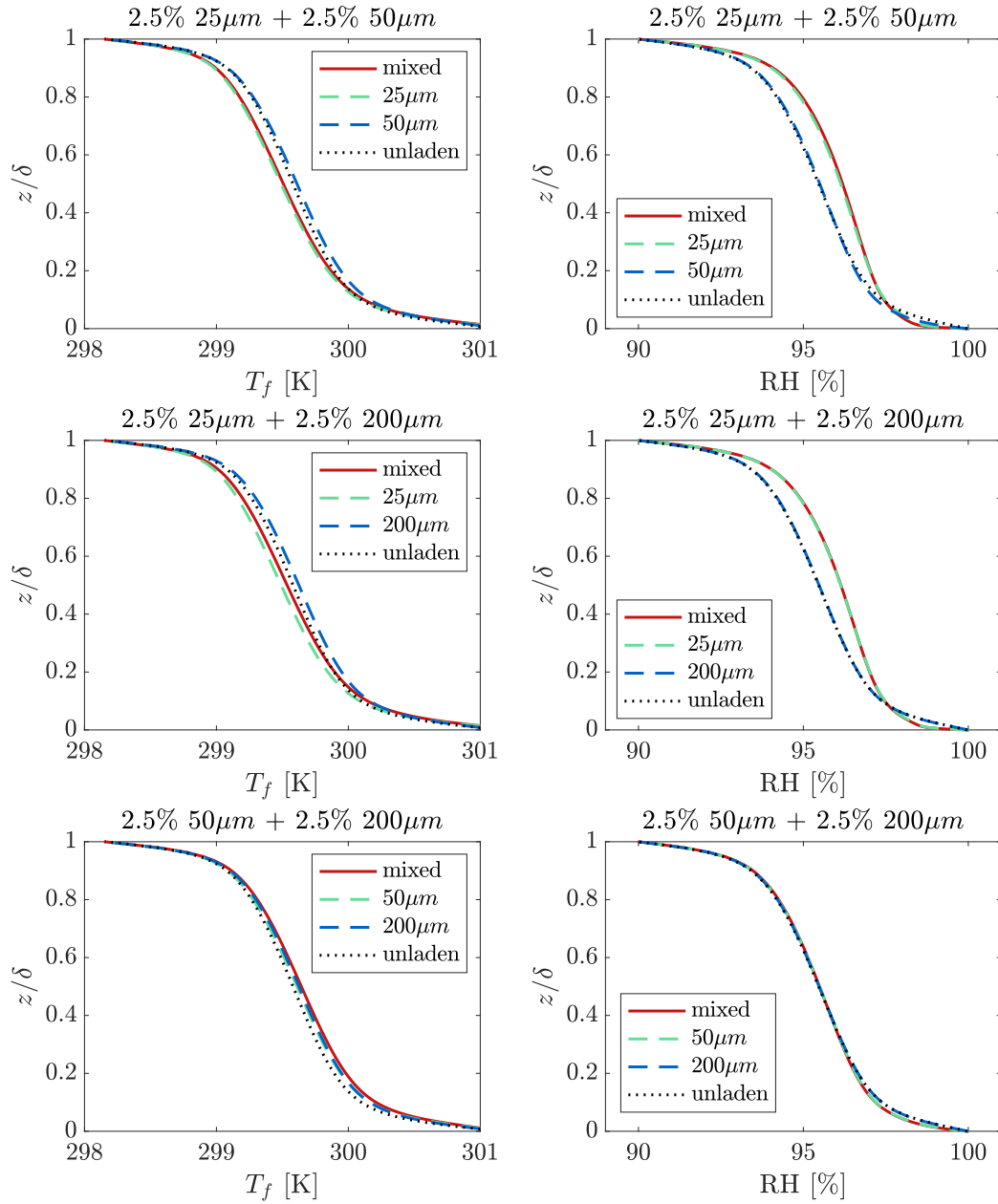


Figure 5.3. Air temperature ( $T_f$ ) and relative humidity ( $RH$ ) of different combinations of spray droplets. Solid lines represent the poly-dispersed cases, and dashed lines are the components from corresponding mono-dispersed cases.

represents the horizontal and temporal average. Similarly, one can write the equation for the specific humidity  $q_f$  (c.f. Eq. (2.4)). As a result, we plot the comparison between the bi-dispersed cases and the super-positioned results from mono-dispersed cases in Fig. 5.4.

From Fig. 5.4 for all three size combinations, one observes that in a simple bi-dispersed simulation, the super-positioned values from mono-dispersed cases predict the temperature and the specific humidity profiles very well. We also find a similar result for other mass fraction. This indicates that, statistically, spray maintains a similar air-spray difference of temperature and radius to the surrounding air comparing with the mono-dispersed cases, while the mean profiles are modified in a different way from the mono-dispersed cases.

### 5.2.3 Responses of heat fluxes

For the focus of this dissertation – heat fluxes: we first evaluate the overall sensitivity of the total heat flux ( $H_T$ ) to the mass fraction ( $\Phi_m$ ) and compare it to the mono-dispersed cases. As seen in Fig. 4.9 from Ch. 4, small droplets have multiple cancellation effects that diminish its sensitivity of  $H_T$  to  $\Phi_m$  due to its very short temperature response time. However, larger droplets show increased sensitivity to  $\Phi_m$ , and the increase tends to stop when the ratio of residence time and temperature response time reaches  $O(10)$ .

For the bi-dispersed case, in Fig. 5.5, we compare the modification of  $H_T$  (in vertical axis) from the bi-dispersed simulations (solid lines) with the mono-dispersed cases (dashed lines) versus  $\Phi_m$  (in horizontal axis), where the mass fraction of mono-dispersed cases is matched to the total mass fraction of the corresponding bi-dispersed cases. As can be seen in Fig. 5.5,  $H_T$  modified by bi-dispersed cases is generally bounded by the corresponding mono-dispersed cases of their components, but not a perfect average of the mono-dispersed cases.

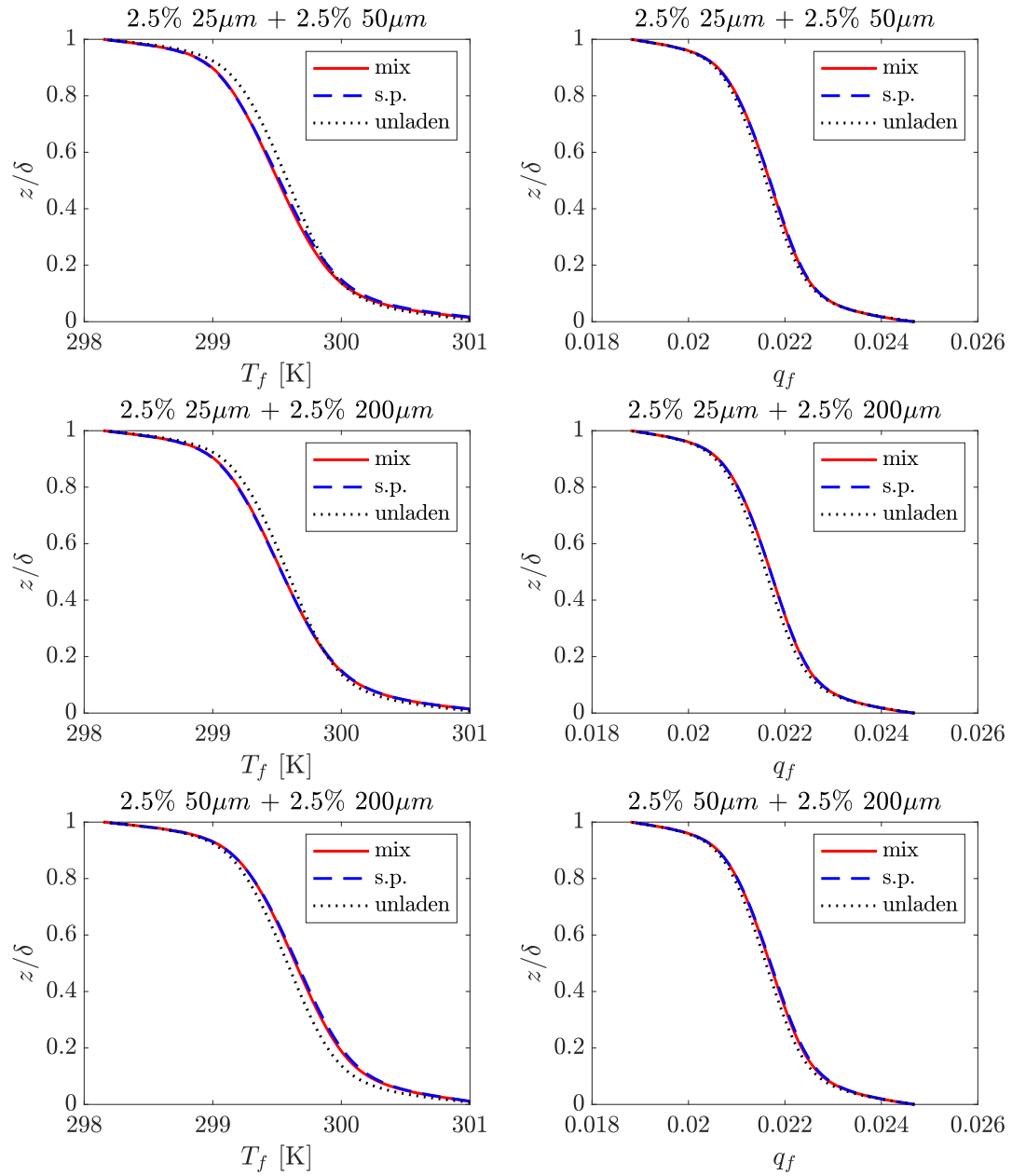


Figure 5.4. Air temperature ( $T_f$ ) and specific humidity ( $q_f$ ) of different combinations of spray droplets. Solid lines represent the poly-dispersed cases, and dashed line is the superposition of corresponding mono-dispersed cases.

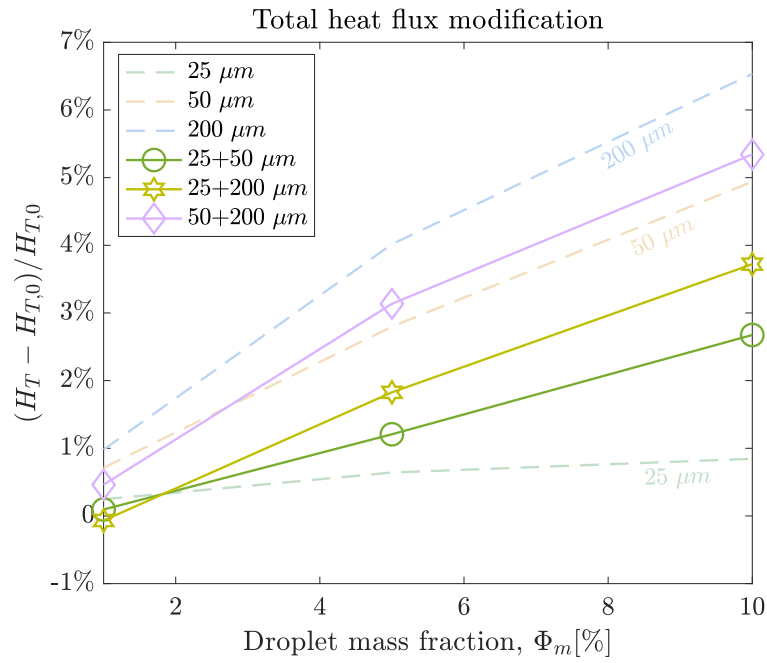


Figure 5.5. Modification of the total heat fluxes by droplets: bi-dispersed (solid lines) vs. mono-dispersed cases (dashed lines).

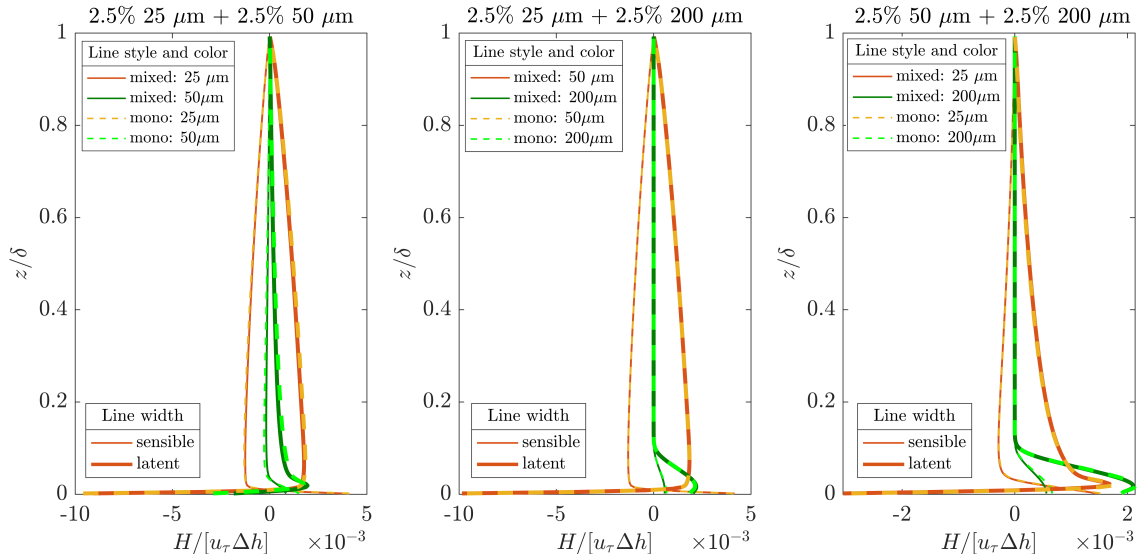


Figure 5.6. Sensible and latent spray-mediated heat fluxes,  $H_{s,sp}$  (thin lines) and  $H_{L,sp}$  (thick lines) respectively, of different combinations of spray droplets. Solid lines represent the poly-dispersed cases, and dashed line is the components from corresponding mono-dispersed cases.

We then break down the total heat flux ( $H_T$ ) into its sensible and latent spray-mediated (with subscript ‘part’) and turbulent heat fluxes (with subscript ‘turb’) (c.f. Eq. (2.20)). In Fig. 5.6, we plot the heat fluxes that are associated with each size class from the bi-dispersed cases (solid lines) and from the corresponding mono-dispersed cases (dashed lines) with a 50% of the total mass of bi-dispersed cases (c.f. Eq. (5.2) and (5.3)). Note, the comparison is different from Fig. 5.5 where the total  $\Phi_m$  is matched between individual mono- and bi-dispersed cases.

By definition, the spray-mediated heat fluxes are computed based on the source terms in Eqs. (2.12) to (2.14), which are functions of temperature or humidity difference between the air and droplet at the droplet surface. For all three size combinations, we observe that the dashed lines almost overlap with the solid line except for a slight error near the lower boundary, indicating the spray-mediated heat fluxes are not significantly influenced by other sizes.

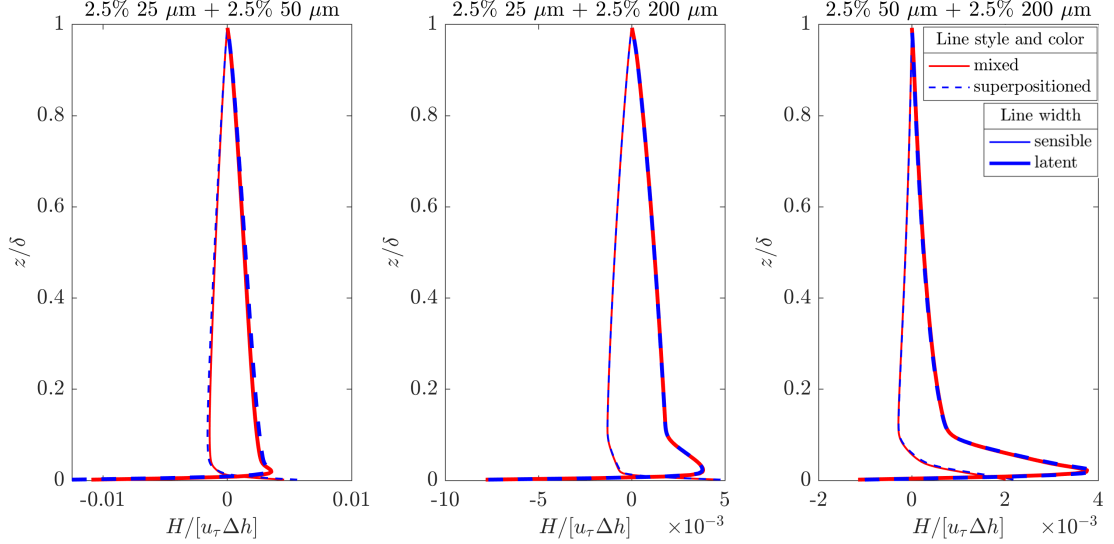


Figure 5.7. Sensible and latent spray-mediated heat fluxes,  $H_{s,sp}$  (thin lines) and  $H_{L,sp}$  (thick lines) respectively, for different combinations of spray droplets. Solid lines represent the poly-dispersed cases, and dashed lines represent the superposition of corresponding mono-dispersed cases.

Given the minimal difference between the mono-dispersed and bi-dispersed cases in the spray-mediated heat fluxes for each component, we again compare the combined results of  $H_{s,sp}$  and  $H_{L,sp}$  from bi-dispersed cases with the super-positioned heat fluxes in Fig. 5.7 in a similar manner shown in Eq. (5.8). As expected based on Fig. 5.3, adding the spray-mediated flux from mono-dispersed cases well predicts the spray-mediated heat fluxes in bi-dispersed cases, although slight errors occur for the 25+50  $\mu\text{m}$  case for the sensible spray-mediated flux  $H_{s,sp}$ .

In terms of the sensible and latent turbulent fluxes, we also test if we can add the differences between the two mono-dispersed cases and the unladen case to infer the heat flux in a bi-dispersed system similar to Eq. (5.8). In Fig. 5.8,  $H_{s,turb}$  and  $H_{L,turb}$  are plotted for both super-positioned and bi-dispersed DNS results. We find that super-positioning turbulent heat fluxes also predict the bi-dispersed system pretty well. Especially, when small (25 $\mu\text{m}$ ) or medium (50 $\mu\text{m}$ ) droplets are mixing with the

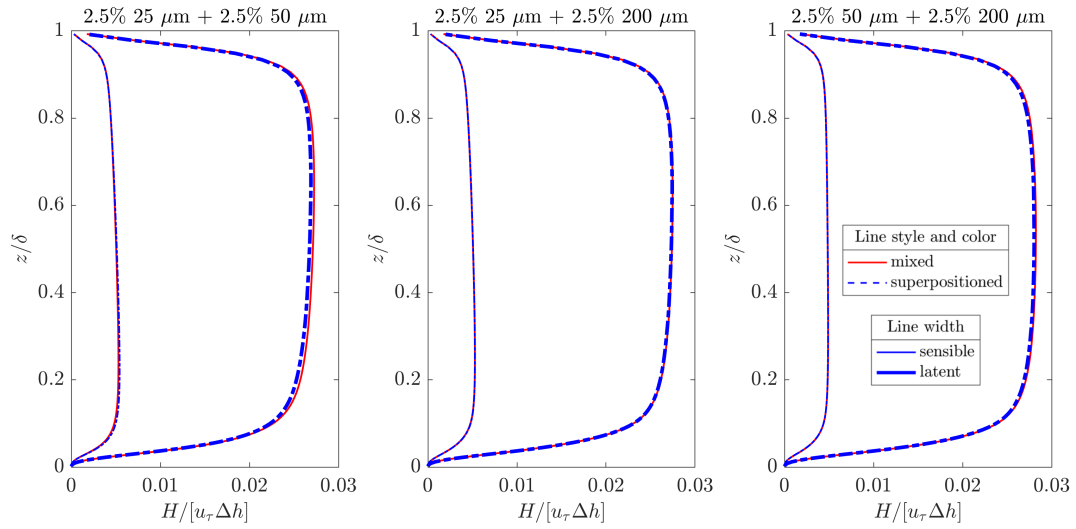


Figure 5.8. Sensible and latent turbulent heat fluxes,  $H_{s,turb}$  (thin lines) and  $H_{L,turb}$  (thick lines) respectively, for different combinations of spray droplets. Solid lines represent the poly-dispersed cases, and dashed line is the superposition of corresponding mono-dispersed cases to the unladen cases to the unladen case.

large droplets (200  $\mu\text{m}$ ), the fact that large droplets cannot be easily transported by turbulence due to relatively large inertia makes the prediction a bit more accurate. However, for the case with 25+50  $\mu\text{m}$  droplets (the first panel), the result shows a slight under-prediction in the turbulent latent heat flux in the lower half of the domain where 50- $\mu\text{m}$  droplets have a substantial local concentration.

To summarize for all cases, we plot the error of super-positioning heat fluxes from mono-dispersed cases in Fig. 5.9, and the error is calculated as

$$\text{err} = \frac{1}{\delta} \int_0^z [H(z) - \hat{H}(z)] dz, \quad (5.9)$$

where the hat indicates the super-positioned estimates and  $\delta$  is the domain height. Thus, a positive error indicates an underestimate by super-position, while a negative value indicates an overestimate. For the total heat flux ( $H_T$ , panel (f)), as we can see, increasing mass fraction leads to a transition from a slight underestimation to an overestimation by super-positioning mono-dispersed cases, although the error for all scenarios are confined within  $\pm 2\%$  for  $H_T$ .

For the individual flux components, the errors are more significant. In particular, the magnitude of errors for small-medium droplets on the sensible and latent spray-mediated heat fluxes increase to about 10%, which indicates that simply adding heat fluxes from mono-dispersed case exaggerates both sensible and latent spray-mediated heat fluxes. As we have seen in Ch. 3, small droplets not only redistribute the heat fluxes for the two routes (sensible-latent and spray-turbulent). Thus, errors in the total spray-mediated flux ( $H_{sp} = H_{s,sp} + H_{L,sp}$ ) are much more confined (but still negative) compared with the larger errors in individual spray-mediated heat-flux components. Otherwise, we would expect a similar magnitude of error for  $H_{sp}$  as its sensible component  $H_{s,sp}$ . On the other hand, when there are no small droplets (pink lines), a consistent pattern of how errors evolve with mass fraction  $\Phi_m$  is present for

all flux components. This pattern agrees the previous discussions on the potential of independent contributions from droplets when the timescale ratio  $\tilde{t}_L$  is smaller than  $O(1)$ .

In Fig. 5.8, we also notice that the latent turbulent flux ( $H_{L,turb}$ ) dominates other heat-flux components. Hence, the error of  $H_T$  is significantly influenced by the error of  $H_{L,turb}$  under the current boundary condition. If the boundary condition varies, the leading source of the errors might change to another flux component. As seen in Figs. 3.10 and 3.9, the cancellation effects of small droplets applies to various boundary conditions, which may suggest that the error of  $H_T$  would be constrained while other components experience different scenarios of errors due to the redistribution of heat fluxes by small droplets.

#### 5.2.4 Statistics on the temperature and radius change of droplets

As discussed in Ch. 4, bulk models rely on the droplets statistics to evaluate the spray-mediated heat fluxes. Thus, the mean  $\Delta T_p$  and  $\Delta r_p$  are essential for capturing the sensible and latent heat transfer of droplets. In Fig. 5.10, we plot a set of comparisons between bi-dispersed and mono-dispersed cases for  $\Delta T_p$  (first row) and  $\Delta r_p$  (second row). In each panel, the solid lines are the result of mono-dispersed cases, and the markers represent the bi-dispersed cases. The mass fraction of all cases in each panel is also the same. For example, in panel (a), the mono-dispersed case for  $25 \mu m$  is 0.5%, which is the mass fraction of  $25\text{-}\mu m$  droplets in the bi-dispersed cases.

For small droplets like  $25 \mu m$ , a general trend among all scenarios is that  $\Delta T_p$  and  $\Delta r_p$  are kept at nearly the same value as the mono-dispersed case. This finding is similar to what Fig. 4.8 showed that  $\Delta T_p$  and  $\Delta r_p$  for small droplets are controlled by the boundary conditions because they have little memory of what they have experienced in the turbulence. The only exception is that  $\Delta T_p$  and  $\Delta r_p$  slightly increase under a high mass fraction at 10% (panel (c) and (f)) when mixed with 200-

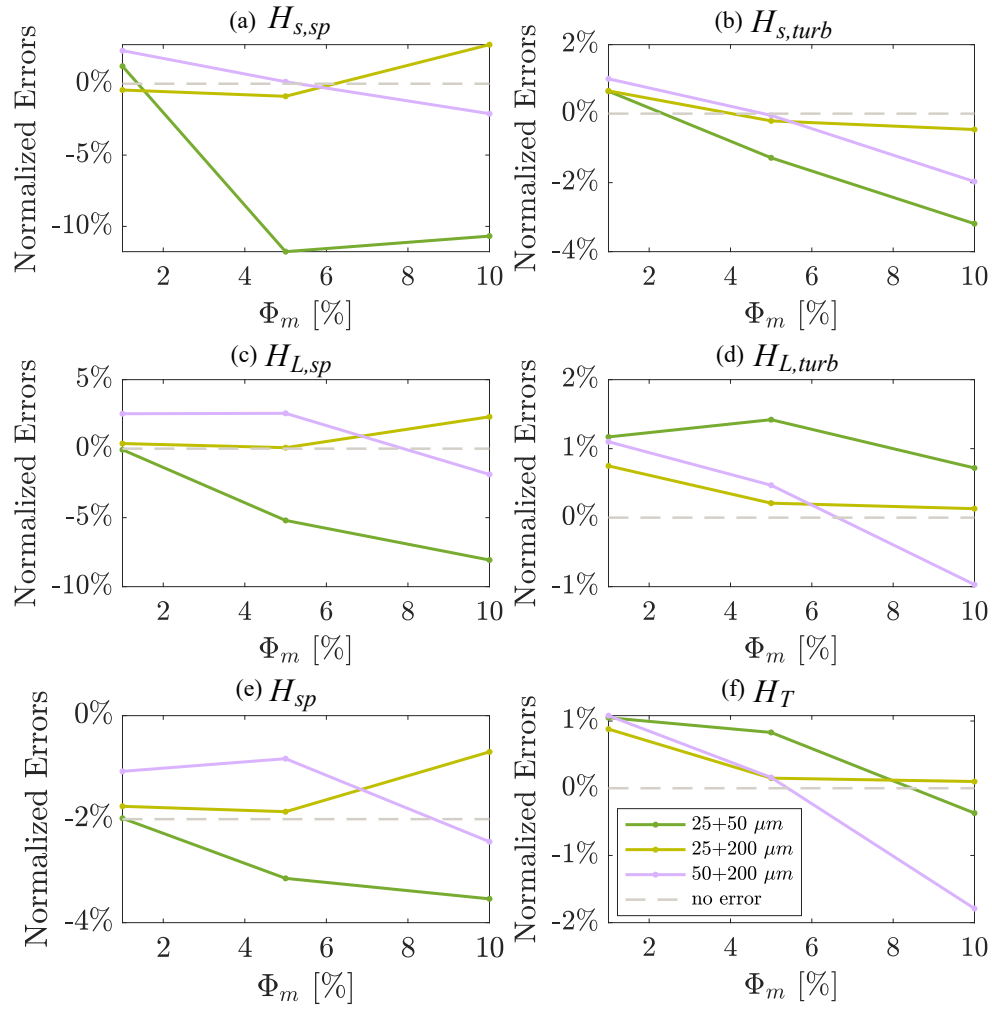


Figure 5.9. Mean error of heat fluxes between bi-dispersed cases and super-positioned cases. Negative errors indicate that the super-positioned value overestimates the corresponding DNS result.

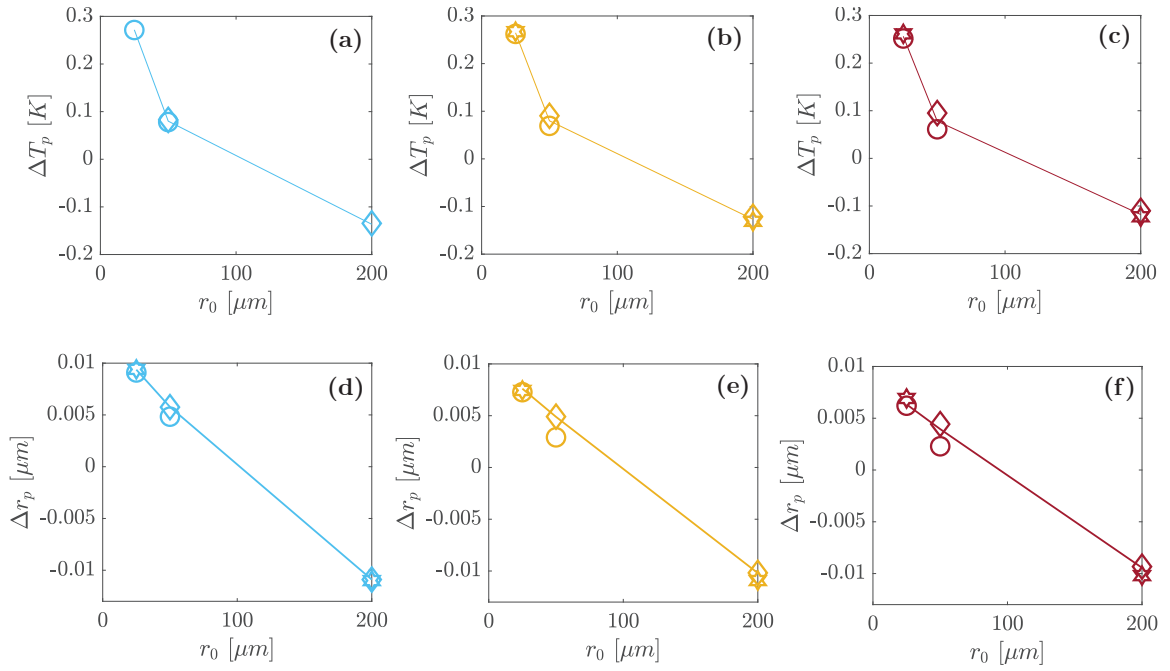


Figure 5.10.  $\Delta T_p$  and  $\Delta r_p$  for bi-dispersed cases (markers) and mono-dispersed cases (lines). Three mass fraction are plotted: panel (a) and (d):  $\Phi_m = 1\%$ ; panel (b) and (e):  $\Phi_m = 5\%$ ; panel (c) and (f):  $\Phi_m = 10\%$ .

$\mu\text{m}$  droplets, although the magnitude of the change is very small too. One possible reason is the increased humidity and temperature near the bottom boundary due to 200- $\mu\text{m}$  droplets.

For medium droplets ( $\sim 50\mu\text{m}$ ), how  $\Delta T_p$  and  $\Delta r_p$  vary from their mono-dispersed value depends on the size of droplets they are mixed with. When mixing with 25- $\mu\text{m}$  droplets, as mass fraction increases,  $\Delta T_p$  decreases from the mono-dispersed value (solid lines). Considering the decreased air temperature and increased humidity in the air (see Fig. 5.3) induced by 25- $\mu\text{m}$  droplets, the change in the field could be the reason for the decrease of  $\Delta T_p$  for 50- $\mu\text{m}$  droplets. Similarly, as we have seen the increase in the air humidity in Fig. 5.3,  $\Delta r_p$  for 50- $\mu\text{m}$  droplets also decreases since the increased background humidity weakens the radius change.

In an opposite way, when large droplets coexist with medium droplets, taking the cases with 50- and 200- $\mu\text{m}$  droplets (diamonds in Fig. 5.10) as an example,  $\Delta T_p$  and  $\Delta r_p$  slightly increase with  $\Phi_m$ , although the trend is not as significant as the scenario when mixed with 25- $\mu\text{m}$  droplets. Note that the normalized residence time  $\tilde{t}_L = t_L/\tau_T$  for 50- $\mu\text{m}$  droplets is at  $O(1)$ , so the  $\Delta T_p$  at this size range tend to rely on the ambient condition, which can be modified by both small and large droplets.

For large droplets ( $\sim 200\mu\text{m}$ ),  $\Delta T_p$  and  $\Delta r_p$  also stay nearly the same as the mono-dispersed cases. However, under higher concentration (e.g., 5% or 10%), mixing with 25- $\mu\text{m}$  droplets increases the magnitude of both  $\Delta T_p$  and  $\Delta r_p$  shown in panels (c) and (f) for hexagrams. In other words, 200- $\mu\text{m}$  droplets tend to give up more sensible and latent heat compared to the mono-dispersed cases. This is a similar phenomenon to 50- $\mu\text{m}$  droplets when co-existing with 25- $\mu\text{m}$  droplets as  $T_f$  decreases and  $RH$  increases for the most of the domain. For the 50- and 200- $\mu\text{m}$  bi-dispersed cases, only a slight decrease in the magnitude of  $\Delta T_p$  and  $\Delta r_p$  of 200- $\mu\text{m}$  droplets is observed when  $\Phi_m = 10\%$ .

To summarize, the extent of how  $\Delta T_p$  and  $\Delta r_p$  are influenced by other sizes

varies by spray size and mass fraction. While small droplets have a minimal change in  $\Delta T_p$  and  $\Delta r_p$ , they modify the humidity and temperature field, which is ‘felt’ by droplets with a larger size (thus larger thermal response times). On the other hand, small droplets with short thermal response times will adjust their temperature based on the last moment before returning to the lower boundary, where larger droplets deposit heat and moisture so they could potentially be indirectly influenced by large droplets. Nevertheless, the changes in  $\Delta T_p$  and  $\Delta r_p$  are insignificant unless under a high concentration with large droplets (e.g.,  $200\mu\text{m}$ ).

### 5.2.5 Bulk estimates of heat fluxes

The formula of the bulk model is conceived by assuming that all feedback effects between spray and turbulence are induced by evaporation and related to the spray-mediated latent heat flux. As previously discussed, bulk models rely on accurate estimates to  $\Delta T_p$  and  $\Delta r_p$  to capture the spray-mediated heat fluxes.

While the bulk model assumes that statistics of droplets such as  $\Delta T_p$  and  $\Delta r_p$  are not affected by size distribution, we have seen how  $\Delta T_p$  and  $\Delta r_p$  are affected by other sizes in Fig. 5.10. To test this assumption, when applying the bulk model fit by the mono-dispersed DNS results in Eq. 4.3 with  $\gamma = -0.74$ , we can rewrite the equation as:

$$H_T = H_{T,0} + \sum_{i=1}^{N_{r_0}} [\bar{Q}_{s,i} + \gamma \bar{Q}_{L,i}], \quad (5.10)$$

where  $N_{r_0} = 2$  for the bi-dispersed cases, and  $\bar{Q}_{s,i}$  and  $\bar{Q}_{L,i}$  are the nominal sensible (with subscript ‘s’) and latent (with subscript ‘L’) heat exchange rate (explained in Eqs. 5.4 and 5.5).

In Fig. 5.11, we plot the estimated  $H_T$  from the bulk model with the results directly computed in DNS (markers filled in gray). We can see most predictions (in gray) overestimate the  $H_T$ , especially, for the case consisting 25+200 $\mu\text{m}$  under a high

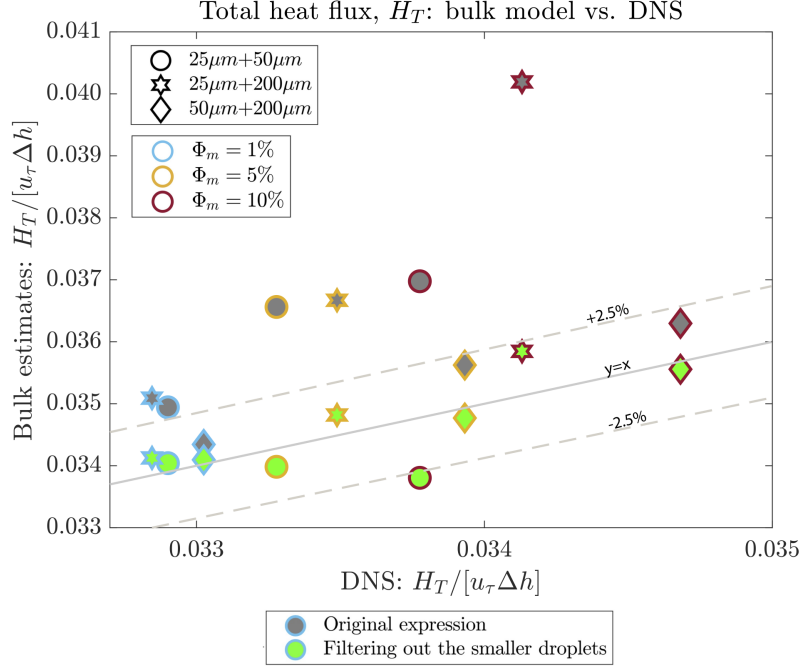


Figure 5.11. Bulk estimation of  $H_T$  vs. the DNS computed values. Markers filled in grey use the original expression shown in Eq. (4.3), and markers filled in green filter out the smaller size between the two sizes in a simulation.

$\Phi_m$ , where the error is around 15.5% (e.g., dark red hexagrams filled in gray).

Thus, by observing the errors in Fig. 5.11, we can infer that the overestimates of  $H_T$  might be a result of over-estimating the contributions from small droplets. As we discussed in the previous sections, the changes in air temperature and humidity are dominated by small droplets, so they modify the effective ambient environment for larger droplets. However, the  $\Delta T_p$  and  $\Delta r_p$  of small droplets is determined by the temperature and humidity field near the bottom boundary, where larger droplets dominate the concentration. These ‘conflicting’ facts indicate that the influence of larger droplets could also be included in these statistics for small droplets, potentially leading to double counting the influence from both sizes, thus overestimates of  $H_T$ . Considering that small droplets tend to have a net cancellation effect by redistributing

the heat fluxes, in Fig. 5.11, we try to re-evaluate the bulk estimation and remove the contribution from the smaller droplets by setting the corresponding generation rate  $F_i = 0$ .

In Fig. 5.11, we plot the estimates of  $H_T$  to compare with the original bulk model in Eq. (5.10). The updated results are plotted with the same markers but filled in green. For cases with 25 + 200  $\mu\text{m}$  droplets (hexagrams), removing the contribution significantly improves the prediction quality, especially for cases with a high  $\Phi_m$ , where errors for all three cases are reduced to  $\pm 2.5\%$ . The correction by filtering out the smaller droplets also works for cases with 50- $\mu\text{m}$  and 200- $\mu\text{m}$ , where the errors after the correction approached within  $\pm 0.5\%$ .

However, for cases with 25+ 50 droplets, although removing the 25- $\mu\text{m}$  droplets improves the issue of overestimates, it also causes an underestimate of  $H_T$  under a high  $\Phi_m$  (dark red circles), indicating that the interaction between small and medium droplets is more complex than the combination mixing small and large droplets.

## 5.2.6 Summary for the bi-dispersed cases

To summarize, from a series of idealized bi-dispersed simulations, we find that the influence of droplets from different sizes are nearly independent when considering mean quantities such as temperature, humidity, and heat fluxes. However, this finding does not necessarily distract the attention for the interaction between droplets on the life-time temperature and radius change for droplets, which are essential to bulk models. In particular, we find evidence that small, medium, and large droplets influence each other but in different ways, resulting in the differences in how sensitive droplets are to other sizes. This difference suggests a reconsideration of the bulk estimation on the total heat flux.

### 5.3 Simulations with a poly-dispersed size distribution

Given a more realistic scenario, the poly-dispersity of spray droplets are parameterized by sea spray generation function (SSGF). In this study, we adopt two types of commonly used scaling of SSGF:

- a power-law scaling of droplet number to droplet radius ( $r_p^{-3}$ , uniform droplet mass) that is observed by the lab experiment by [Ortiz-Suslow et al. \(2016\)](#) for droplets ranging from 80  $\mu\text{m}$  to 1400  $\mu\text{m}$  (thereafter ‘UM’), and
- an exponential-decay of droplet number to droplet radius derived by [Andreas \(1998\)](#) which is further simplified by [Troitskaya et al. \(2016\)](#) for idealized study (thereafter ‘A98’).

Mathematically, for the two types of the scaling, one could write the SSGF  $S_n$  as

$$S_n(r_0) = \begin{cases} C_1 r_0^{-3} & \text{UM} \\ C_2 \left(\frac{U_{10}}{u_0}\right)^d \exp(-\chi r_0) & \text{A98} \end{cases} \quad (5.11)$$

where  $U_{10}$  is the 10-m wind velocity and selected at 40 m/s in the current study as an example, and the remaining fitting coefficients are set as  $d = 0.01 * (U_{10} - 40) + 5.5 = 5.5$  and  $\chi = 0.023$  ([Troitskaya et al., 2016](#)). In this study, we adopt the scaling of the SSGF but control the total mass of droplets in a simulation. Hence,  $C_1$  and  $C_2$  in Eq. (5.11) are the fitting constant coefficients to adjust the the droplet size sampled from  $S_n$  to the assigned mass fraction.

Converting Eq. (5.11), one can get the probability of droplet generated ( $\mathcal{P}(r_{0,i})$ ) for each size class  $i$  in a discrete perspective as,

$$\mathcal{P}(r_{0,i}) = \frac{S_n(r_{0,i})}{\sum_{i=1}^{N_{r_0}} S_n(r_{0,i})}, \quad (5.12)$$

with the cumulative probability for each size as

$$\mathcal{F}(r_{0,j}) = \sum_{j=1}^i \mathcal{P}(r_{0,j}), \quad (5.13)$$

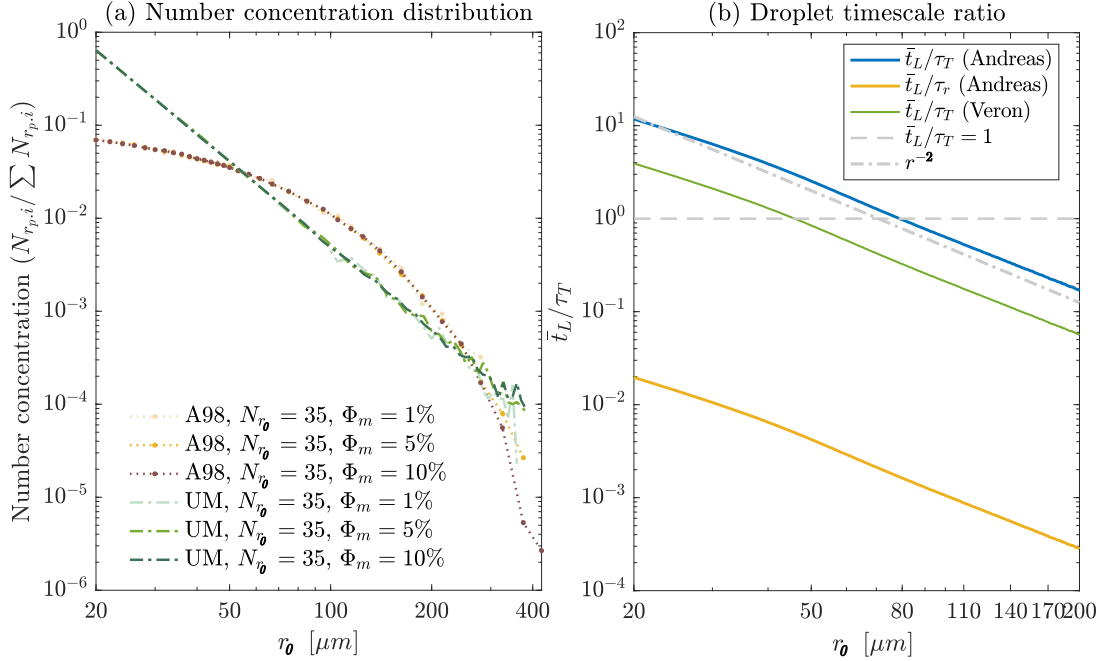


Figure 5.12. (a) Number concentration distribution of the initial size ( $r_0$ ) for different SSGFs, and (b) Ratios of spray timescales given the initial size ( $r_0$ ). Note that the ratio between residence time ( $t_L$ ) and radius response time ( $\tau_r$ ) is much smaller than the ratio scaled by the temperature response time ( $\tau_T$ ).

where  $j = 1$  to  $i$ , and  $i = 1$  to  $N_{r_0}$ .

To initialize the number of droplets in the simulation, first, the mass of water  $m_w$  in the droplet phase is calculated based on the mass fraction (defined as  $\Phi_m = m_w/m_a$ , where  $m_a$  is the mass of air in the domain). At the initialization stage, the radius array  $r_{0,i}$  (where  $i = 1$  to  $N_{r_0}$ ) is defined, and a random number is drawn from a uniform distribution ranging from 0 and 1. The size  $r_{0,i}$  that has the closest cumulative probability  $\mathcal{F}(r_{0,j})$  to this random number will be selected as the droplet radius. The drawing continues until the total  $\Phi_m$  reaches the set value. To ensure a statistically steady size distribution, new droplets introduced to the system have the same initial radius of its precedent one at a random location and with a random

initial velocity.

In this section, we approximate the continuum SSGFs in the simulation to sample the SSGF with an incremental size  $\delta r_0 = 1\mu\text{m}$  for the initial droplet size. To simplify the complexity in sampling simultaneous flow and spray statistics for the DNS solver in parallel, we also consider a group of case for the poly-dispersity, where  $N_{r_0}$  is reduced to 35 with a wider interval of  $\delta r_0$ .

### 5.3.1 Changes in droplet temperature and radius

To begin with, we evaluate the droplet  $\Delta T_p$  and  $\Delta r_p$  for the uniform-mass SSGF as a comparison to Fig. 5.10. Similar to the bi-dispersed cases, we measure the change in droplet temperature ( $\Delta T_p$ ) and radius ( $\Delta r_p$ ) throughout its residence time for all sizes. In Fig. 5.13, we plot the 2-D probability density functions (PDFs) sampled in simulations (subplots (a) and (c), in log color-scale) and mean values of  $\Delta T_p$  and  $\Delta r_p$  are plotted against droplets' initial size  $r_{0,i}$  (subplots (b) and (d)).

From the 2-D PDFs, one can see a larger variability in  $\Delta T_p$  given the initial size than the more concentrated distribution for radius change  $\Delta r_p$ , qualitatively in agreement to the statistics sampled for mono-dispersed cases in Ch. 4. Moreover, we also see that smaller droplets (e.g.,  $r_0 < 50\mu\text{m}$ ) have a strong preference in  $\Delta T_p$  and  $\Delta r_p$  in the high-density region, indicating the local influence of droplet statistics in this size range.

For  $\Delta T_p$ , Fig. 5.13 shows that droplets with radius greater than about  $70\mu\text{m}$  have a negative  $\Delta T_p$  while smaller droplets (with  $r_0 < O(70\mu\text{m})$ ) have a positive  $\Delta T_p$ . This general trend of  $\Delta T_p$  on droplet size here is consistent with the results in Chap. 3 and 4. From Fig. 5.12 we notice that the transition zone between positive and negative  $\Delta T_p$  is around  $r_0 = 70\mu\text{m}$ , which has a corresponding  $\tilde{t}_L = t_L/\tau_T$  in  $O(1)$ .

In addition, it is remarkable that there is a small difference of the mean  $\Delta T_p$  when

it comes to the small droplets (size ranging from 25 to 50  $\mu\text{m}$ ) regarding the different total mass fraction ( $\Phi_m$ ) and SSGF. The insensitivity of  $\Delta T_p$  here again gives another example that the temperature of small droplets with  $\tilde{t}_L \gg 1$  is determined by the boundary conditions rather than its residence time. As the droplet size increases, the differences in  $\Delta T_p$  among different simulations also become more significant, where the maximum magnitude of  $\Delta T_p$  occurs in  $O(100 \mu\text{m})$  (i.e.,  $\tilde{t}_L$  ranges between  $O(1)$  to  $O(0.1)$ ).

Compared to the relative insensitivity of  $\Delta T_p$  to the SSGFs (between yellow and green lines), spray's sensitivity in  $\Delta T_p$  is stronger to the total droplet mass fraction ( $\Phi_m$ ), where a higher  $\Phi_m$  results in a smaller magnitude of  $\Delta T_p$  for larger droplets. This indicates that the extra heat and moisture due to a high  $\Phi_m$  slows down the evaporation of larger droplets. However, as  $\Phi_m$  increases, the magnitude of positive  $\Delta T_p$  for droplets around  $50\mu\text{m}$  slightly increases, indicating smaller droplets may experience a higher humidity once returning the lower boundary. As we discussed in Ch. 4, the increase of  $\Delta T_p$  is primarily caused by the condensation of saline droplets at a high  $RH$ . In mono-dispersed cases, we learned that the magnitude of  $\Delta T_p$  decreases with  $\Phi_m$ . Hence, larger droplets in the system cause the change in the trend of  $\Delta T_p$  for smaller droplets.

When it comes to the mean radius change, we see slightly more complex behavior among all droplet size classes. First, there does not exist the same  $\Delta r_p$  for small droplets (e.g., 20  $\mu\text{m}$ ). For example,  $\Delta r_p$  for small droplets ( $< 50 \mu\text{m}$ ) decreases when  $\Phi_m$  increases, indicating a negative feedback effect by the change in the humidity field near the bottom boundary due to increased droplet mass. When the droplet size increases, one can see a similar trend of  $\Delta T_p$  for  $\Delta r_p$ , where the differences in  $r_0$  among various cases are more significant. Also, the magnitude of  $\Delta r_p$  increases with  $r_0$  until it saturates at about 250  $\mu\text{m}$ .

We also notice, in Fig. 5.13 (second panel), that there is a neck-like zone for  $\Delta r_p$

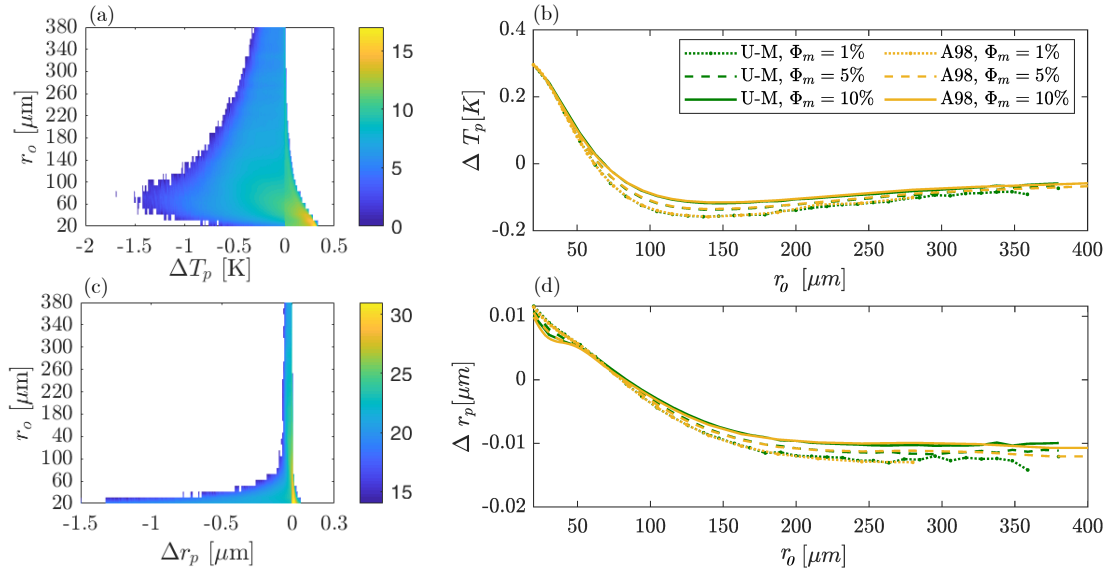


Figure 5.13. Statistics of droplet temperature change ( $\Delta T_p$ ) and radius change ( $\Delta r_p$ ) as a function of initial droplet radius on different evaporation and two-way coupling conditions. In the left column, subplots (a) and (c) show the 2D-PDF for the “U-M” case (raw) under  $\Phi_m = 5\%$ ; in the right column, subplots (b) and (d) show the mean of  $\Delta T_p$  and  $\Delta r_p$  for both “U-M” and “A98” SSGF under different  $\Phi_m$ .

when  $r_0$  is between  $50 \mu\text{m}$  and  $100 \mu\text{m}$  before the  $\Delta r_p$  reaches the net-zero value. Since medium-size droplets can receive influence from both small and large droplets, this could be the reason for the low sensitivity on both mass fraction and SSGFs for this size range.

As a summary, for the poly-dispersed simulations, we see a similar trend of  $\Delta T_p$  and  $\Delta r_p$  from the mono-dispersed and bi-dispersed cases, and the interactions between sizes are noticeable, especially under high mass fraction.

### 5.3.2 Bulk estimation for the poly-dispersed cases

Recall Eqs. (2.26) and (2.25), the sensible and latent spray-mediated heat fluxes,  $H_{s,sp}$  and  $H_{L,sp}$  respectively, are written based on  $\Delta T_p$  and  $\Delta r_p$ . In this part, we first examine the estimates of bulk models on the spray-mediated heat fluxes to see if the bulk model works on all sizes and then discuss the estimates on the total heat flux.

#### 5.3.2.1 Spray-mediated heat fluxes

Based on Eqs. (5.6) and (5.7), we estimate spray-mediated heat fluxes in a similar way to Ch. 4 but for each size component in a simulation. In Fig. 5.14, we plot the ratio between bulk estimates and DNS results of total spray-mediated heat flux ( $H_{sp}$ ) and its sensible and latent components at the surface ( $z = 0$ ), against the initial droplet radius for the uniform-mass SSGF.

As we can see, these ratios between the bulk estimates and DNS for the spray-mediated heat fluxes are not always equal to 1. Hence, the bulk model does not always give an accurate prediction. First, for the total spray-mediated heat flux  $H_{sp}$ , the bulk estimates are fairly accurate for droplets below  $50 \mu\text{m}$  (where results are plotted near the dashed reference lines). However, the bulk model constantly underestimates the  $H_{sp}$  for droplets larger than  $70 \mu\text{m}$ . The ratio between bulk estimates and DNS results is about 0.9. In Fairall et al. (1994), using  $\bar{Q}_s$  to approximate  $H_{sp}$  is based on

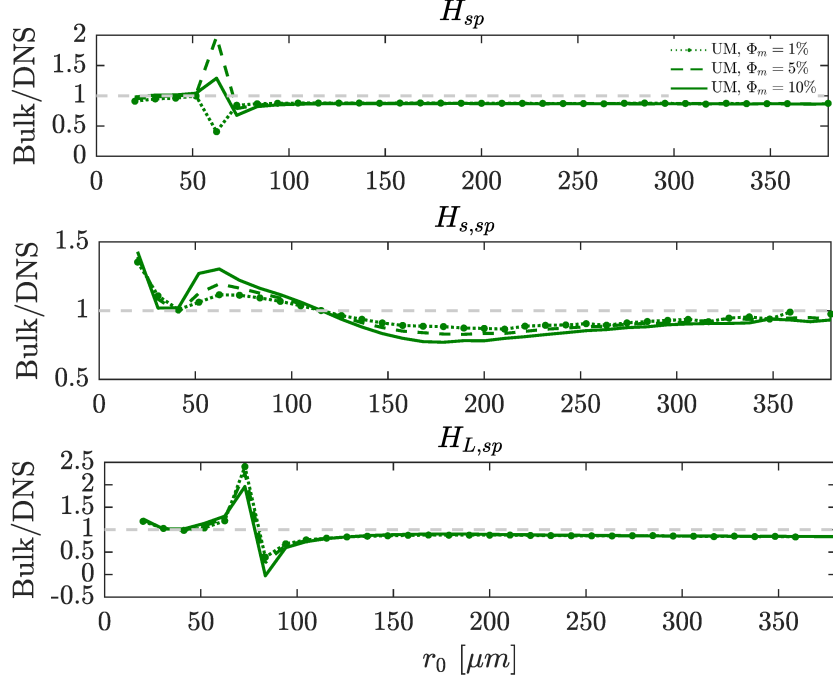


Figure 5.14. Spray-mediated heat fluxes: the ratio between the bulk estimates and DNS results as a function of initial droplet for the three mass fractions of the ‘UM’ SSGF ( $N_{r_0} = 35$ ). If the ratio between bulk-estimated value and DNS results is great than 1, it indicates the overestimation by the bulk models, and vice versa.

the assumption that the evaporation of droplets is in equilibrium. Since  $\tilde{t}_L$  indicates whether or not droplets enter the equilibrium stage, there is no surprise that the bulk model provides a good result for  $r_0 < 50 \mu\text{m}$  (with  $\tilde{t}_L > O(1)$ ).

Between 50 to 70  $\mu\text{m}$ , predictions in this range involve significant errors. In fact,  $\tilde{t}_L = t_L/\tau_T$  for this range is  $O(1)$ . Droplets in this size range have very small  $\Delta T_p$  and  $\Delta r_p$  as we seen in previous figures, and the spray-mediated heat fluxes  $H_{s,sp}$  and  $H_{L,sp}$  are also small compared with small droplets (c.f. Fig. 5.3). Therefore, the errors are easily magnified when estimating the flux in this range due to the small value from DNS in the denominator.

However, in contrast to  $H_{sp}$ , the bulk model, in fact, is inferior for providing

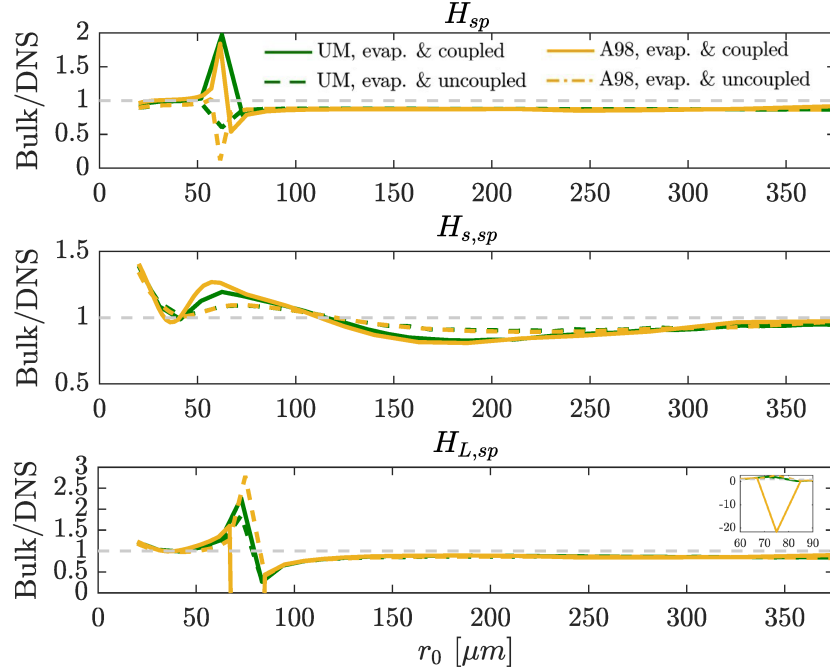


Figure 5.15. Spray-mediated heat fluxes: the ratio between the bulk estimates and DNS results for ‘UM’ (in green) and ‘A98’ (in yellow) ( $N_{r_0} = 35$ ). Different line styles indicates the evaporation and coupling conditions. Ratio  $> 1$  indicates the overestimation by the bulk models, and vice versa.

a reasonable prediction on the sensible spray-mediated flux  $H_{s,sp}$ . First, for the small droplets, it overestimates  $H_{s,sp}$ , with a significant error for more than 40% for 20- $\mu\text{m}$  droplets. Also, from 50  $\mu\text{m}$  to 100  $\mu\text{m}$ , there is a local maximum for the overestimating errors. For droplets larger than about 125  $\mu\text{m}$ , an underestimation occurs, while the extent of the underestimation hits a local maximum between 150 to 200  $\mu\text{m}$  and then gradually recovers back to an accurate estimation.

For the latent spray-mediated heat flux ( $H_{L,sp}$ ), we see a more similar trend to the total spray-mediated flux  $H_{sp}$ , with less sensitivity to the mass fraction than the sensible counterpart  $H_{s,sp}$ . However, the errors between 50 to 100  $\mu\text{m}$  are still significant.

To find the reason why the bulk model fails to predict spray-mediated heat fluxes

in a certain size range, we consider more scenarios with varying conditions on evaporation and SSGF. For both ‘UM’- and ‘A98’- size distributions, we consider a case with evaporation but no two-way thermal coupling and a case with no evaporation nor the thermal coupling, along with the original two-way coupled.

In Fig. 5.15, we plot the same evaluation in Fig. 5.14 for  $\Phi_m = 5\%$ . For the two-way coupled cases (solid lines), two different size distributions have a similar general trend to the results on spray-mediated heat fluxes. However, for the sensible component  $H_{s,sp}$ , different size distributions yield different accuracy on the bulk estimates, which can be seen near 50 to 100  $\mu\text{m}$ , showing the sensitivity of the influence from another sizes in this size range via the two-way coupling.

Then, we compare the results between the uncoupled (dashed lines) and coupled (solid lines) cases. We find the most sensitive size range for the interactions and feedback from other sizes occurs at 50 to 70  $\mu\text{m}$ . For the sensible components  $H_{s,sp}$ , implementing two-way thermal coupling increases the error when predicting the medium size range, and it also emphasizes the sensitivity of SSGF on the quality of bulk models. That being said, when inferring the background temperature field in a practical model by implementing constant heat fluxes with Monin-Obukhov similarity theory (e.g. Mueller and Veron (2014b)), neglecting the coupling effects would lead noticeable errors due to neglecting the coupling effects.

By comparing to the non-evaporating cases (dotted lines) and fully coupled cases, we find that evaporation of droplets is the ultimate reason why the discrepancies arise between bulk and DNS models for droplets, and the errors are magnified by the two-way coupling.

### 5.3.2.2 Total heat flux

Last but not least, we revisit the bulk estimation for the total heat flux  $H_T$ . Here, along with those plotted in Fig. 5.11, we consider another modification to the bulk

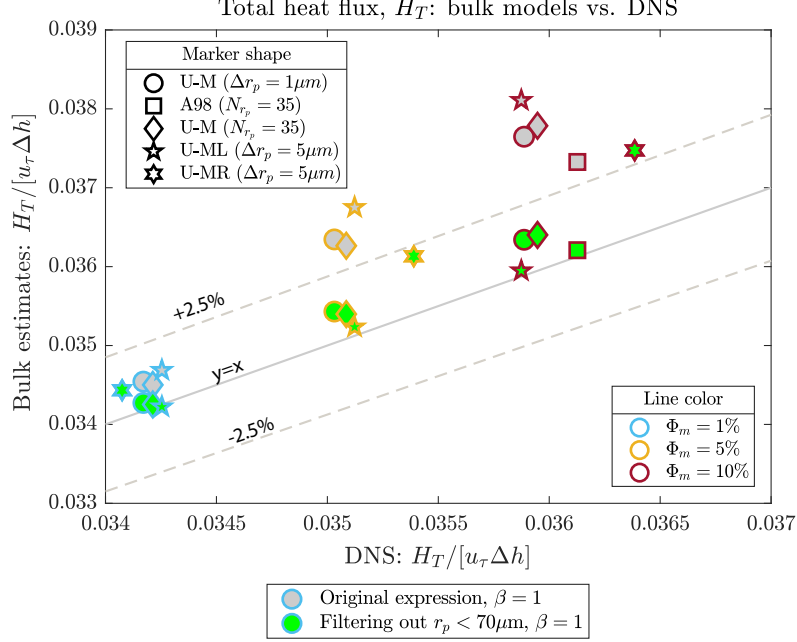


Figure 5.16. Bulk estimation of  $H_T$  vs. the DNS computed values for poly-dispersed cases. Markers filled in grey use the original expression shown in Eq. (4.3), and markers filled in green filter out the size smaller than  $70\mu m$  in a simulation. A group of results considering  $\beta = 0.9$  are also plotted as a comparison to the original expression.

model. The original bulk estimation can be write as  $H_T = H_{T,0} + \beta \bar{Q}_s + \gamma \bar{Q}_L$ . In Ch. 4, we adopt  $\beta = 1$  from Fairall et al. (1994) and fit the feedback term ( $\gamma$ -term) based on the difference between laden and unladen cases ( $H_{T,0}$ ) for how much the interfacial flux is changed.

In Fig. 5.16, we plot a larger variety of size range in Fig. 5.16 (e.g. pentagrams for  $20\text{-}135\mu m$  and hexagrams for  $70$  to  $200\mu m$ ). We notice that filtering out small size significantly reduced the errors, where the limiting size is set at  $70\mu m$  after several trials between  $35\mu m$  to  $100\mu m$ . In particular, for a high mass fraction, the errors are also significantly reduced. Therefore, the plot again shows that the original bulk model itself cannot capture the interaction between different droplet sizes and thus double-counts the influence from smaller droplets.

Consider the important role that spray timescales play, we hence put forward the following tentative correction to Eqs. (4.3) and (5.10) for the bulk model to eliminate the over-counting issue based on droplet timescales, i.e.,

$$H_T = H_{T,0} + \sum_{i=1}^{N_{r_0}} \mathcal{H}(-\log \tilde{t}_L) [\beta \bar{Q}_{s,i} + \gamma \bar{Q}_{L,i}], \quad (5.14)$$

where  $\mathcal{H}(x)$  is the Heaviside step function, which is equal to 1 when  $x \geq 0$ .  $\tilde{t}_L = t_L/\tau_T$  is the timescale ratio defined in Eq. (4.4), and  $\beta$  is set in  $O(1)$  with  $\gamma = -0.74$ . The updated results applying Eq. (5.14) are plotted with markers filled in green in Fig. 5.16.

### 5.3.3 Representative droplet sizes of a continuum size distribution

To make a further simplification for the spray model, an a “fast” model is introduced to use one size to representing the SSGF (e.g., Andreas et al. (2008, 2015); Rastigejev and Suslov (2016)), where the representative size is assumed based on either the statistical characteristics of an SSGF (*a priori*) or the proportion of the contribution of sensible and latent heat fluxes from each size class in the bulk model (*ad hoc*, i.e., the size where most spray-mediated heat fluxes come from).

In reality, however, the inertia and the settling effect of droplets result in a varying size distribution along the vertical direction, which indicates that the SSGF parameterized at the ocean surface may not reflect the size distribution for the majority of the lower MABL. For example, some of the droplets with large  $St_k$  can merely be transported upward away from the lower domain by the turbulence. Thus, unless all droplets play the same role in heat fluxes and the turbulence dispersed the sensible and latent heat into the whole region of interests, using one size may introduce errors due to ill-posed assumptions on spray-mediated heat and mass transfer. Then, a further question is how to pick this representative droplet size for a given SSGF.

In this section, we test the three representative sizes on a ‘UM’ (cubic-decayed) on a benchmark boundary condition (“M1” in Table. 2.3), where the vertical profile of air temperature, relative humidity, and heat fluxes are examined.

### 5.3.3.1 Poly-dispersity and the representative size of SSGFs

Three representative sizes based on a given size distribution are considered in this study, which are the arithmetic mean, square-root mean, and cubic-root mean of the distribution. Specifically, given  $n = 1, 2, 3$ , one could write the representative sizes as:

$$\langle r_p \rangle_{(n)} = \left( \frac{\sum_{i=1}^{N_p} r_p^n}{N_p} \right)^{\frac{1}{n}}, \quad (5.15)$$

where  $i$  is the unique index for generated droplets, and  $N_p$  is the total amount of droplets given a specific size distribution and mass fraction.

In Eq. (5.15), for the arithmetic mean when  $n = 1$ , it indicates the contribution of heat and mass from spray are not related to spray’s properties such as size or density; for the square-root mean when  $n = 2$ , the representative size indicates that only the total surface area matters exists among all spectre of spray droplets that dominate the heat and mass transfer (i.e., a surface process); when  $n = 3$ , the representative size indicates that heat and mass transfer is a volume-process where the volume/mass of droplets is the important parameter, so that the shape or the size may not be important.

Applying Eq. (5.15) to the uniform-mass SSGF, we calculate the representative size given the size range starting with  $20 \mu\text{m}$ , which yields the three representative sizes listed in Table 5.2.

In Fig. 5.17, we plot the three representative size  $\langle r_p \rangle_{(i)}$  ( $i = 1, 2, 3$ ) for three cases in Table 5.2 for all droplets and the vertical profiles of  $\langle r_p \rangle_{(3)}(z)$  when only taking the horizontal average. We notice that turbulence only transports a cer-

TABLE 5.2

## POLY-DISPERSED CASES AND THEIR REPRESENTATIVE SIZES

SSGF	Size range	$\langle r_p \rangle_{(1)}$	$\langle r_p \rangle_{(2)}$	$\langle r_p \rangle_{(3)}$
UM-narrow	20-200	36.0	42.7	52.2
UM-medium	20-250	36.6	44.7	56.6
UM-wide	20-380	37	48.1	65.6

Note:  $\langle r_p \rangle_{(1)}$ ,  $\langle r_p \rangle_{(2)}$ , and  $\langle r_p \rangle_{(3)}$  are calculated based on Eq. 5.15. ‘UM’ represents the uniform-mass (cubic-decay) scaling of droplet concentration. Unit: [ $\mu\text{m}$ ].

tain range of size upward as already seen. Within the spray layer ( $\delta_{inj} = \frac{1}{8}\delta$ ), the volume-weighted mean radius is much larger than  $\langle r_p \rangle_{(3)}$  due to the presence of heavy droplets. However, the mean size weighted by volume above the spray layer is smaller than  $35\mu\text{m}$ , which is slightly smaller to the value of the arithmetic mean  $\langle r_p \rangle_{(1)}$ . In addition, despite the different size range, the mean size for these SSGFs above  $\delta_{inj}$  quickly converges, which are invariant to the difference in the concentration of heavy droplets.

### 5.3.3.2 Comparisons on air temperature, humidity, and heat fluxes

To compare the response in temperature and humidity fields to the droplet representative sizes, in Fig. 5.18, we plot the vertical profiles of  $T_f$  and  $RH$  for three different representative sizes and the corresponding poly-dispersed size distributions. We find that the volume-weighted  $\langle r_p \rangle_{(3)}$  successfully predicts the  $T_f$  and  $RH$  profiles for the 5% mass-loading case. In Fig. 5.18, one could see that the blue dashed lines (representing  $\langle r_p \rangle_{(3)}$ ) are overlapped with the solid magenta line (poly-dispersed case), although there is slight error in the lower domain for  $RH$ . That being said,

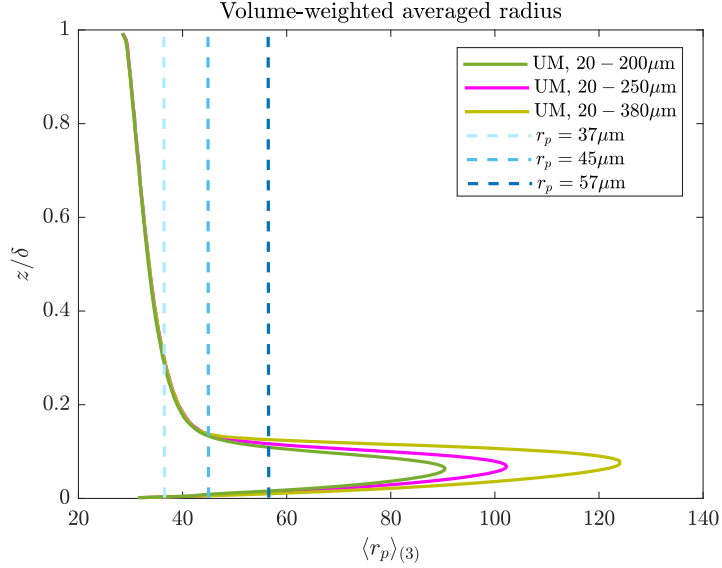


Figure 5.17. The volume-weighted mean radius for three size ranges of the ‘UM’ SSGF, along with three representative sizes calculated for the ‘UM-medium’ case.

although the volume-weighted radius for the most of the domain (when  $z/\delta > 0.2$ ) is close to the arithmetic mean (around  $37\mu\text{m}$ ),  $T_f$  and  $RH$  of the air phase respond to the spray droplets in a similar way regardless of how the droplets are transported by the turbulence (c.f. Fig. 5.17), under the current system with one-way momentum coupling in the current turbulent flow.

By comparing the heat fluxes, it is seen that the sensible spray-mediated and turbulent heat fluxes can be generally predicted by the mono-dispersed case with  $\langle r_p \rangle_{(3)}$ , although error occurs within the injection layer. For example, Fig. 5.20 shows that  $\langle r_p \rangle_{(3)}$  better predicts the sensible spray-mediated and turbulent heat fluxes compared to the latent counterparts. For the latent spray-mediated heat flux, Fig. 5.20 shows that  $\langle r_p \rangle_{(3)}$  still gives the closest estimation among three representative sizes, while one could also notice the significant errors in the lower domain where heavier droplets reside.

Since a representative size better predicts the sensible heat fluxes, a potential

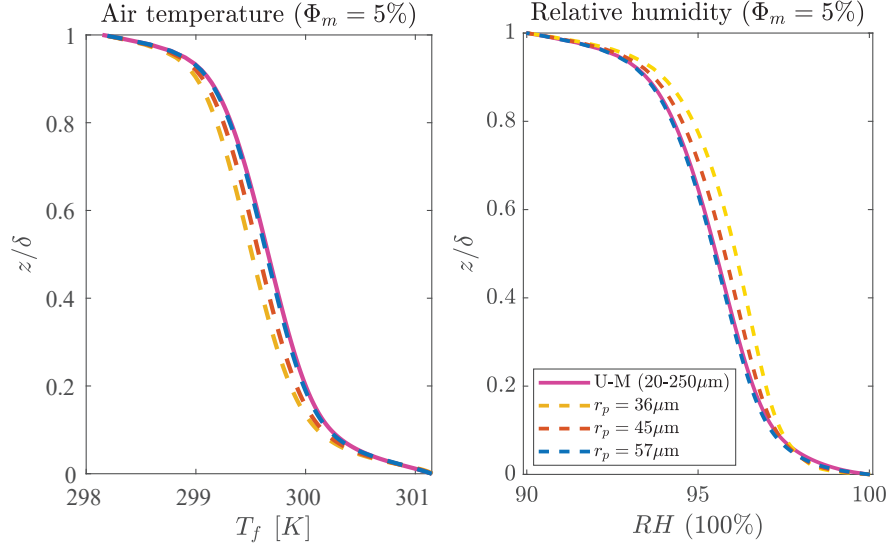


Figure 5.18. Air temperature ( $T_f$ , left) and relative humidity ( $RH$ , right) for the three representative cases and the ‘UM-medium’ case.

reason could be that the equilibrium temperature of droplet evaporation prevents droplets further from going below the limit given a similar background temperature and humidity. For example, based on Eq. (2.10), the lowest droplet temperature in the system for a droplet is near the wet-bulb temperature (c.f. the quasi-equilibrium of  $T_p$  in Fig. 2.3). In the left panel of Fig. 5.18, one notices where the results for representative size and the SSGF overlaps above  $z = \frac{1}{8}\delta$ , and in Fig. 5.2 the volume-weighted average radius above  $z = \frac{1}{8}\delta$  is around  $70 \mu\text{m}$  or less. In Fig. 5.12, we see that droplets in radius below  $O(50 - 70 \mu\text{m})$  have  $\tilde{t}_L > 1$ , which suggests that droplets beyond  $z > \frac{1}{8}\delta$  are capable to reach the quasi-equilibrium statistically.

We further test on different boundary conditions (listed in Table 2.3) for the zero temperature difference (denoted as ‘‘M2’’, hence no sensible turbulent heat flux in principle) and an inverse temperature difference (denoted as ‘‘M6’’, colder air at the bottom boundary) than the benchmark boundary conditions. As one can see in Fig. 5.19, under different boundary conditions, the volume-weighted representative size

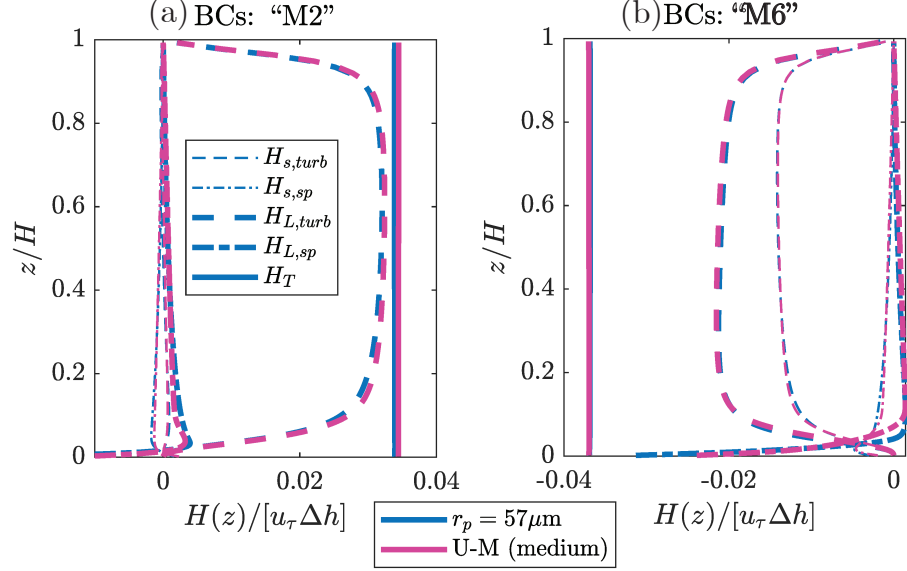


Figure 5.19. Comparisons of heat fluxes between the poly-dispersed cases and cases with the volume-weighted representative size ( $r_p=57\mu\text{m}$ ) for different boundary conditions listed in Table 2.3: (a) bottom and top boundaries have the same temperature (“M2”); and (b) inverse temperature difference (“M6”).

$\langle r_p \rangle_{(3)}$  arguably captures all heat fluxes across the domain, especially above the so-called spray-layer ( $\delta_{inj}$ ). Therefore, the volume-weight average size of an SSGF is a decent *a priori* option of the representative size.

In fact, in the previous section, when applying super-positioned solutions of  $T_f$  and  $RH$  as well as heat fluxes from two mono-dispersed cases with a half droplet mass for the corresponding bi-dispersed cases, we have implicitly applied the volume-weighted average to the temperature and humidity field. Thus, we see the super-positioned results give fairly well prediction of the bi-dispersed cases, showing the feasibility to use  $\langle r_p \rangle_{(3)}$  as the representative size.

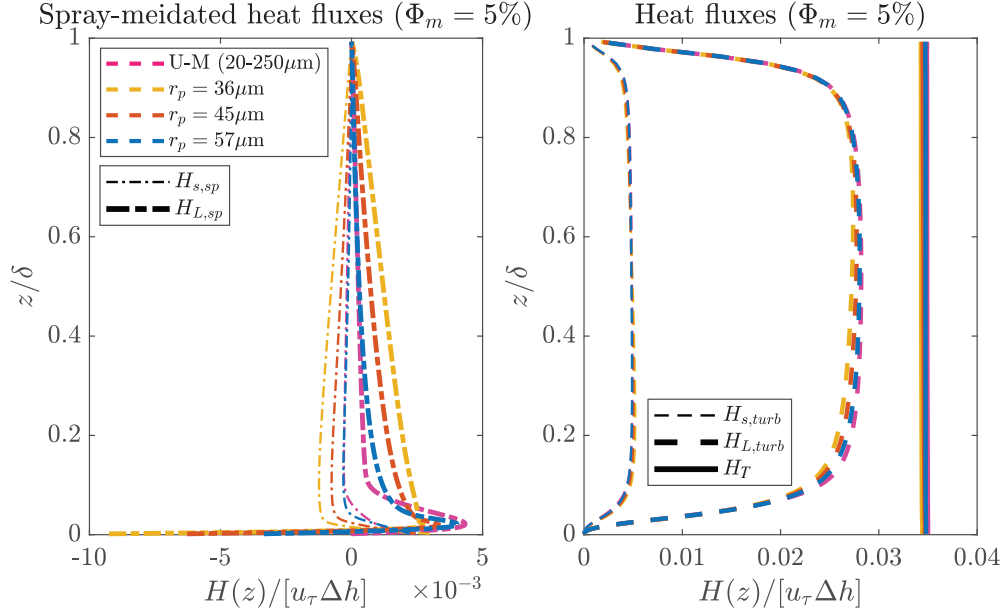


Figure 5.20. Sensible and latent spray-mediated heat fluxes (left), turbulent and total heat flux (right) for the three representative cases and the ‘UM-medium’ case.

### 5.3.3.3 Effective size range

To avoid the caveat due to a specific selection of the size range and to examine the sensitivity to different size ranges of SSGF, we also compare the results of the  $\langle r_p \rangle_{(3)}$  calculated for 20-250  $\mu\text{m}$  to other two size ranges listed in Table 5.2 by changing the size limit of heavy droplets.

In Fig. 5.21, the overlapped curves between all three cases and representative mono-dispersed cases indicate that the heavy droplets may not have a significant influence on the fields of  $T_f$  and  $RH$ . Since we have learned from the bi-dispersed section that small droplets lead the changes in the temperature and humidity fields, the limited turbulent transport on these heavy droplets plus its low mass fraction could explain the minor changes when narrowing or expanding the range of the size distribution.

For the heat fluxes, from panels (b) and (c) in Fig. 5.21, one can notice only slight

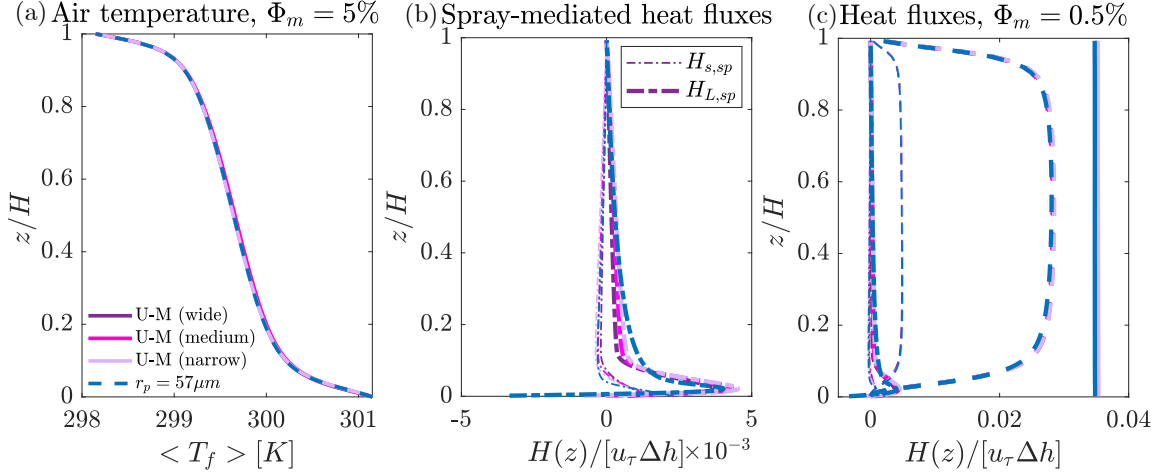


Figure 5.21. Vertical mean profiles of (a) Air temperature ( $T_f$ ), (b) Sensible and latent spray-mediated heat fluxes, and (c) turbulent and total heat flux for  $\langle r_p \rangle_3$  of the ‘UM-medium’ case and three ‘UM’ cases with different size distributions.

differences in both the spray-mediated and turbulent heat fluxes by extending the heavy-end of the size distribution, but overall the differences are trivial considering the changes in the volume-weighted mean radius shown in Fig. 5.17.

As mentioned in both Mueller and Veron (2014b) and Ortiz-Suslow et al. (2016), large droplets (e.g., the spume droplets) occur under very high wind speed, and the end of size spectrum increases with the wind speed. Unless the distribution of the mass significantly increases at the heavy end of the SSGF, our results here does not suggest a remarkable sensitivity of the heat fluxes to the extending heavy size of the size distribution, because heavy droplets essentially could become a part of lower boundary above the ocean surface while smaller droplets are transported away from this region.

To thoroughly investigate the influence of the tail of the droplets, other factors such as turbulence intensity, the increase in mass fraction, and other surfaces processes (e.g., wave breaking) need to be systematically considered. However, due to the limitation of the solver, we cannot resolve heavy droplets such as  $2000 \mu m$ . Other-

wise, it violates the hypothesis of point-particles for the Lagrangian solver. However, based on the discussion on Ch. 4, a possible result when wind speed increases could be that the increased residence time of droplets shifts the transition area to a larger size, which in turn compensates the heat-deposit effect due to increased mass in very heavy droplets. Nevertheless, to reveal the scaling relationships between wind speed and the increase in  $\tilde{t}_L$  or the change in the SSGF requires further investigations, which is beyond the scope of the current dissertation.

#### 5.4 Summary

In this chapter, we discuss the spray effects with multiple sizes involved in a simulation, and we examine another fundamental assumption of the so-called bulk model for heat fluxes when the poly-dispersed size distribution is involved. With idealized two-size experiments, we find that from an Eulerian perspective, droplets have a relatively independent impact when mixing with other sizes, so that the vertical profiles of temperature, humidity, and heat fluxes can be reasonably approximated by superpositioning the results from mono-dispersed DNS simulations. Furthermore, we test three different averaging methods to find a representative size of a continuum size distribution. We find that the volume-weighted-mean size predicts the temperature and humidity field well and qualitatively captures the vertical profiles of heat fluxes, which could help simplify the computation for the large-scale models.

However, we find issues when applying droplet temperature and radius change to our DNS model. The interactions between droplet sizes indicate that assuming independent contributions from different spray classes may introduce error, which is the overestimation issue of the bulk model. By analyzing the direction how droplets are influenced in the idealized two-size simulations, we find the overestimation of bulk models is caused by over-counting the contribution by small droplets. We hence put forward correction by filtering out the contribution from the droplets with  $\tilde{t}_L > 1$ ,

which in turn successfully improves the accuracy of bulk estimations on the total heat flux.

For the spray-mediated heat fluxes, we further evaluate a common bulk model by Fairall et al. (1994), where the hypothesis is based on equilibrium evaporation. In contrast to the mono-dispersed study shown in Ch. 4, the bulk estimates do not always predict the spray-mediated heat flux for all size when considering polydispersity spray distribution. While the bulk estimates generally captured the total spray-mediated heat flux, the bulk model has a poor performance on the sensible components and all fluxes with timescale ratio  $\tilde{t} = t_L/\tau_T \approx O(1)$  – the size range that is most susceptible to the influences from other sizes.

For the representative size, we evaluated three different averaging methods to find a representative size of a continuum size distribution. We find that the volume-weighted mean size predicts the temperature and humidity field well and qualitatively captures the vertical profiles of heat fluxes given different boundary conditions, which could help simplify the computation for the large-scale models. We further discuss the effective size range, with varying weights on the heavy droplets under the uniform-mass distribution. We find an overall weak influence from heavy droplets on heat flux as well as temperature profiles under the uniform-mass size distribution, indicating the limited influence from the heavy droplets in terms of heat exchange.

The conclusions may sound conflicting, but the frameworks discussed of the two perspectives (Eulerian vs. bulk) in this chapter are different. Thus, the different perspectives lead to different treatments for predicting the thermal influence from spray in turbulence where fluctuations are in a wide range of temporal signatures. Though the simulations are based on a simplified surface layer, the current study provides physical evidence for simplification of the complex physics associated with spray, which potentially improve both the accuracy and efficiency of spray model development.

## CHAPTER 6

### CONCLUSIONS

Due to the inherent complexity of the system, there are many limitations that hinder the process from revealing the underlying physics on the feedback effects of sea spray. With direct numerical simulations, we simulate a simplified air-sea interface via a spray-laden turbulent open-channel flow. With the high-resolution Eulerian-Lagrangian solver, we resolve the dynamics and thermodynamics of spray droplets in turbulence. With the high-fidelity model, we conduct a series of numerical experiments to investigate topics related to spray effects that not well understood in the air-sea modeling community.

For the influences of spray droplets on the air-sea heat fluxes, we find that the role of spray depends on its size in Ch. 3. Since the size of droplets determines its signatures in dynamic and thermodynamic responses to the turbulence in the atmosphere, spray droplets have a different residence time and temperature/radius response times at the air-sea interface. Reciprocally, the feedback effects from spray droplets to the turbulence vary with the size of droplets.

From the DNS, we observe two categories of influences from spray droplets. The smaller droplets respond rapidly to the ambient environment and have long suspension times. Hence, they modify and redistribute the latent and sensible heat in the turbulence. However, the competing signs of this modification lead to an overall weak effect on the total heat flux. On the other hand, larger droplets have a slower thermodynamic response to the environment, so they are less prone to insert this compensating effect. When this compensating effect is not present, the total heat

flux is enhanced given the warmer lower sea surface, but the enhancement is dependent on the concentration and suspension time. Therefore, one can identify the role that spray droplets play in the turbulence (c.f. Fig. 3.11) by considering the ratio between the residence time and temperature response time ( $\tilde{t}_L$  in Eq. (4.4)). The main difference between our study and the previous understandings lies in the influence of droplets with  $\tilde{t}_L > 1$ , where studies that ignore the cancellation effect overestimate their influences.

We then connect our findings on the governing roles of droplet timescales with the bulk models of Andreas et al. and Fairall et al. in Ch. 4. We find that the quality of the underlying assumptions of bulk models is sensitive to spray's timescales. While both models assume that spray experiences a uniform and steady ambient condition, our results show that this assumption only works well for droplets with long thermodynamic time scales and relatively short lifetime. When the thermodynamic time scales are short, the models fail to predict the correct temperature and radius change of spray that are irrelevant to the field that droplets have experienced. Thus, the models introduce errors in predicting spray-mediated heat fluxes, which in turn overestimates the total heat fluxes. Moreover, we find a negative feedback mechanism induced by the spray evaporation that may be missing in the bulk models. Ignoring this feedback effect could lead to further overestimates of the total heat flux when the spray-mediated flux is treated as an add-on to the corresponding interfacial flux.

For the hypotheses on the poly-dispersity of spray droplets, we discussed them in Ch. 5 for the interaction between different droplet sizes. From idealized bi-dispersed simulations, the mean profiles of temperature, heat, and heat fluxes of a poly-dispersed system can be primarily inferred by super-positioning corresponding mono-dispersed simulations, but the errors in the heat fluxes suggest the interaction between droplets in different sizes. We also observe the interactions between different spray size classes in terms of the statistics of droplet temperature and radius change.

Hence, neglecting the cross-size interactions may lead to further misunderstanding of the total heat flux when applying bulk models due to the double-counting problems. To avoid the potential double-counting issues, we suggest the removal of the contribution from smaller droplets with  $\tilde{t}_L > O(1)$ . This correction improves the bulk estimate of the total heat flux from the DNS results. In addition, the representative size of a continuum distribution is also discussed in this chapter. We find that the mono-dispersed cases with the volume-weighted mean size qualitatively reproduce the vertical profiles of temperature and humidity as well as heat fluxes of the poly-dispersed cases. Hence, the volume-weighted average size of SSGFs may be used as the non-*ad hoc* representative size, although we observe that errors are present near the lower domain where heavy spray droplets are dominant.

There are prospects for the extension of the current study. First, given the spray microphysics with small-scale fluctuations are revealed in this study, one may apply the current Eulerian-Lagrangian model into different spatial scales via large-eddy simulations with more physical processes included. The sub-grid model for spray dispersion and evaporation can be built using the findings in the DNS study. Second, the current DNS produces an enormous amount of information on the flow fields and droplet trajectories. Thus, one could apply statistical analysis to test the hypotheses in Eulerian or Lagrangian-stochastic models (e.g., [Mueller and Veron \(2014b\)](#); [Rastigejev and Suslov \(2016\)](#)) and conduct studies for the model comparison. Third, it is well known that solving Navier-Stokes equations for turbulence to the Kolmogorov-scale is very expensive, while it is relatively easier to compute spray trajectories and its evolution in temperature and radius. Thus, a data-driven model (e.g., [Ma et al. \(2016\)](#); [Tryggvason et al. \(2016\)](#)) that tuned by small-scale simulations like the one in this dissertation could possibly help increase the accuracy while retaining the efficiency and simplicity for large-scale models, for spray transport in a Lagrangian perspective or profiles of heat fluxes in an Eulerian perspective .

## BIBLIOGRAPHY

- E. L. Andreas. Time Constants for the Evolution of Sea Spray Droplets, 1990. ISSN 1600-0889. URL <http://onlinelibrary.wiley.com/doi/10.1034/j.1600-0889.1990.t01-3-00007.x/abstract>.
- E. L. Andreas. Sea spray and the turbulent air-sea heat fluxes. *Journal of Geophysical Research*, 99(C7):14345, 1992. ISSN 0148-0227. doi: 10.1029/92JC00876. URL <http://doi.wiley.com/10.1029/92JC00876>.
- E. L. Andreas. The Temperature of Evaporating Sea Spray Droplets, 1995. ISSN 0022-4928.
- E. L. Andreas. A New Sea Spray Generation Function for Wind Speeds up to 32 m s<sup>-1</sup>. *Journal of Physical Oceanography*, 28(11):2175–2184, 1998. ISSN 0022-3670. doi: 10.1175/1520-0485(1998)028<2175:anssgf>2.0.co;2.
- E. L. Andreas. Approximation formulas for the microphysical properties of saline droplets. *Atmospheric Research*, 75(4):323–345, 2005. ISSN 01698095. doi: 10.1016/j.atmosres.2005.02.001.
- E. L. Andreas and J. Decosmo. *Sea Spray Production and Influence on Air-sea Heat And Moisture Fluxes over the Open Ocean*, pages 327–362. Springer Netherlands, Dordrecht, 1999. ISBN 978-94-015-9291-8. doi: 10.1007/978-94-015-9291-8\_13. URL [https://doi.org/10.1007/978-94-015-9291-8\\_13](https://doi.org/10.1007/978-94-015-9291-8_13).
- E. L. Andreas and K. A. Emanuel. Effects of sea spray on tropical cyclone intensity. *Journal of the Atmospheric Sciences*, 58:3741–3751, 2001. doi: 10.1175/1520-0469(2001)058<3741:EOSSOT>2.0.CO;2.
- E. L. Andreas and L. Mahrt. On the Prospects for Observing Spray-Mediated Air-Sea Transfer in Wind-Water Tunnels. *Journal of the Atmospheric Sciences*, page 150917120953004, 2015. ISSN 0022-4928. doi: 10.1175/JAS-D-15-0083.1. URL <http://journals.ametsoc.org/doi/abs/10.1175/JAS-D-15-0083.1>.
- E. L. Andreas, J. B. Edson, E. C. Monahan, M. P. Rouault, and S. D. Smith. The spray contribution to net evaporation from the sea: A review of recent progress. *Boundary-Layer Meteorology*, 72(1-2):3–52, 1995. ISSN 00068314. doi: 10.1007/BF00712389.

- E. L. Andreas, P. O. G. Persson, and J. E. Hare. A bulk turbulent air-sea flux algorithm for high-wind, spray conditions. *Journal of Physical Oceanography*, 38: 1581–1596, 2008. ISSN 0022-3670. doi: 10.1175/2007JPO3813.1.
- E. L. Andreas, L. Mahrt, and D. Vickers. An improved bulk air-sea surface flux algorithm, including spray-mediated transfer. *Quarterly Journal of the Royal Meteorological Society*, 141(687):642–654, 2015. ISSN 00359009. doi: 10.1002/qj.2424. URL <http://doi.wiley.com/10.1002/qj.2424>.
- J.-W. Bao, C. W. Fairall, S. a. Michelson, and L. Bianco. Parameterizations of Sea-Spray Impact on the AirSea Momentum and Heat Fluxes. *Monthly Weather Review*, 139(12):3781–3797, 2011. ISSN 0027-0644. doi: 10.1175/MWR-D-11-00007.1.
- M. M. Bell, M. T. Montgomery, and K. A. Emanuel. Air-Sea Enthalpy and Momentum Exchange at Major Hurricane Wind Speeds Observed during CBLAST. *Journal of the Atmospheric Sciences*, 69(11):3197–3222, 2012. ISSN 0022-4928. doi: 10.1175/JAS-D-11-0276.1.
- L. Bianco, J. W. Bao, C. W. Fairall, and S. A. Michelson. Impact of Sea-Spray on the Atmospheric Surface Layer. *Boundary-Layer Meteorology*, 140(3):361–381, 2011. ISSN 00068314. doi: 10.1007/s10546-011-9617-1.
- a. Bukhovostova, E. Russo, J. G. M. Kuerten, and B. J. Geurts. Comparison of DNS of compressible and incompressible turbulent droplet-laden heated channel flow with phase transition. *International Journal of Multiphase Flow*, 63:68–81, 2014. ISSN 03019322. doi: 10.1016/j.ijmultiphaseflow.2014.03.004. URL <http://dx.doi.org/10.1016/j.ijmultiphaseflow.2014.03.004>.
- S. S. Chen, W. Zhao, M. A. Donelan, and H. L. Tolman. Directional WindWave Coupling in Fully Coupled AtmosphereWaveOcean Models: Results from CBLAST-Hurricane. *Journal of the Atmospheric Sciences*, 70(10):3198–3215, 2013. ISSN 0022-4928. doi: 10.1175/jas-d-12-0157.1.
- R. Clift, J. R. Grace, and M. E. Weber. *Bubbles, Drops, and Particles*. Academic Press, 1978. ISBN 9780121769505. URL <https://books.google.com/books?id=n8gRAQAIAAJ>.
- G. de Leeuw, E. Andreas, M. Anguelova, C. W. Fairall, R. Ernie, C. O’Dowd, M. Schulz, and S. Schwartz. Production Flux of Sea-Spray Aerosol. *Reviews of Geophysics*, 49(2010):1–39, 2011. ISSN 8755-1209. doi: 10.1029/2010RG000349.
- J. DeCosmo, K. B. Katsaros, S. D. Smith, R. J. Anderson, W. A. Oost, K. Bumke, and H. Chadwick. Air-sea exchange of water vapor and sensible heat: The Humidity Exchange Over the Sea (HEXOS) results. *Journal of Geophysical Research: Oceans*, 101(C5):12001–12016, may 1996. ISSN 2156-2202. doi: 10.1029/95JC03796. URL <http://doi.wiley.com/10.1029/95JC03796><http://dx.doi.org/10.1029/95JC03796>.

- W. M. Drennan, J. A. Zhang, J. R. French, C. McCormick, and P. G. Black. Turbulent Fluxes in the Hurricane Boundary Layer. Part II: Latent Heat Flux. *Journal of the Atmospheric Sciences*, 64(4):1103–1115, 2007. doi: 10.1175/JAS3889.1. URL <http://dx.doi.org/10.1175/JAS3889.1>.
- J. B. Edson and C. W. Fairall. Spray droplet modeling 1. Lagrangian model simulation of the turbulent transport of evaporating droplets. *Journal of Geophysical Research*, 99(C12):25295–25311, 1994. ISSN 0148-0227. doi: 10.1029/94JC01883.
- J. B. Edson, S. Anquetin, P. G. Mestayer, and J. F. Sini. Spray droplet modeling 2. An interactive Eulerian-Lagrangian model of evaporating spray droplets. *Journal of Geophysical Research*, 101(C1):1279–1293, 1996. ISSN 01480227. doi: 10.1029/95JC03280.
- K. Emanuel. Tropical Cyclones. *Annual Review of Earth and Planetary Sciences*, 31(1):75–104, 2003. ISSN 0084-6597. doi: 10.1146/annurev.earth.31.100901.141259. URL <http://www.annualreviews.org/doi/10.1146/annurev.earth.31.100901.141259>.
- C. W. Fairall, J. D. Kepert, and G. J. Holland. The effect of sea spray on surface energy transports over the ocean. *The Global Atmosphere and Ocean System*, 2: 121–142, 1994.
- C. W. Fairall, M. L. Banner, W. L. Peirson, W. Asher, and R. P. Morison. Investigation of the physical scaling of sea spray spume droplet production. *Journal of Geophysical Research*, 114(C10):C10001, 2009. ISSN 0148-0227. doi: 10.1029/2008JC004918. URL <http://doi.wiley.com/10.1029/2008JC004918>.
- C. S. Garbe, A. Rutgersson, J. Boutin, G. de Leeuw, B. Delille, C. W. Fairall, N. Gruber, J. Hare, D. T. Ho, M. T. Johnson, P. D. Nightingale, H. Pettersson, J. Piskozub, E. Sahlée, W.-t. Tsai, B. Ward, D. K. Woolf, and C. J. Zappa. Transfer Across the Air-Sea Interface. In *Ocean-Atmosphere Interactions of Gases and Particles*, pages 55–112. 2014. ISBN 9783642256431. doi: 10.1007/978-3-642-25643-1.
- L. Hasse. On the contribution of spray droplets to evaporation. *Boundary-Layer Meteorology*, 61(3):309–313, 1992. ISSN 00068314. doi: 10.1007/BF02042938.
- B. Helgans and D. H. Richter. Turbulent latent and sensible heat flux in the presence of evaporative droplets. *International Journal of Multiphase Flow*, 78:1–33, 2016. ISSN 03019322. doi: 10.1016/j.ijmultiphaseflow.2015.09.010. URL <http://dx.doi.org/10.1016/j.ijmultiphaseflow.2015.09.010>.
- H. J. Holterman. *Kinetics and Evaporation of Water Drops in Air*. IMAG rapport. IMAG, 2003. ISBN 9789054062349.
- D. Jeong, B. K. Haus, and M. a. Donelan. Enthalpy Transfer across the AirWater Interface in High Winds Including Spray. *Journal of the Atmospheric Sciences*, 69(9):2733–2748, 2012. ISSN 0022-4928. doi: 10.1175/JAS-D-11-0260.1. URL <http://journals.ametsoc.org/doi/abs/10.1175/JAS-D-11-0260.1>.

- J. Kepert, C. Fairall, and J.-W. Bao. *Modelling the Interaction Between the Atmospheric Boundary Layer and Evaporating Sea Spray Droplets*, pages 363–409. Springer Netherlands, Dordrecht, 1999. ISBN 978-94-015-9291-8. doi: 10.1007/978-94-015-9291-8\_14. URL [https://doi.org/10.1007/978-94-015-9291-8\\_14](https://doi.org/10.1007/978-94-015-9291-8_14).
- S. Komori, K. Iwano, N. Takagaki, R. Onishi, R. Kurose, K. Takahashi, and N. Suzuki. Laboratory Measurements of Heat Transfer and Drag Coefficients at Extremely High Wind Speeds. *Journal of Physical Oceanography*, 48(4):959–974, 2018. doi: 10.1175/JPO-D-17-0243.1. URL <https://doi.org/10.1175/JPO-D-17-0243.1>.
- C.-Y. Lee and S. S. Chen. Symmetric and Asymmetric Structures of Hurricane Boundary Layer in Coupled AtmosphereWaveOcean Models and Observations. *Journal of the Atmospheric Sciences*, 71(7):3576–3594, 2012. doi: 10.1175/JAS-D-12-046.1.
- E. R. Lewis and S. E. Schwartz. *Sea Salt Aerosol Production: Mechanisms, Methods, Measurements and Models A Critical Review*, volume 152. 2004. ISBN 9780875904177. doi: 10.1029/GM152.
- J. Liu, J. A. Curry, C. A. Clayson, and M. A. Bourassa. High-Resolution Satellite Surface Latent Heat Fluxes in North Atlantic Hurricanes. *Monthly Weather Review*, 139(9):2735–2747, 2011. ISSN 0027-0644. doi: 10.1175/2011MWR3548.1. URL <http://journals.ametsoc.org/doi/abs/10.1175/2011MWR3548.1>.
- M. Ma, J. Lu, and G. Tryggvason. Using statistical learning to close two-fluid multiphase flow equations for bubbly flows in vertical channels. *International Journal of Multiphase Flow*, 85:336–347, 2016. ISSN 03019322. doi: 10.1016/j.ijmultiphaseflow.2016.06.021. URL <http://dx.doi.org/10.1016/j.ijmultiphaseflow.2016.06.021>.
- P. Mestayer and C. Lefauconnier. Patrice Mestayer and Claude Lefauconnier. 93: 572–586, 1988.
- M. T. Montgomery, R. K. Smith, and S. V. Nguyen. Sensitivity of tropical-cyclone models to the surface drag coefficient. *Quarterly Journal of the Royal Meteorological Society*, 136(653):1945–1953, 2010. ISSN 00359009. doi: 10.1002/qj.702.
- J. Mueller and F. Veron. A Lagrangian Stochastic Model for Sea-Spray Evaporation in the Atmospheric Marine Boundary Layer. *Boundary-Layer Meteorology*, 137(1): 135–152, 2010. ISSN 0006-8314. doi: 10.1007/s10546-010-9520-1.
- J. A. Mueller and F. Veron. Impact of sea spray on air-sea fluxes. Part I: Results from Stochastic Simulations of Sea Spray Drops over the Ocean. *Journal of Physical Oceanography*, 44:2835–2853, 2014a. ISSN 0022-3670. doi: 10.1175/JPO-D-13-0246.1.

- J. A. Mueller and F. Veron. Impact of sea spray on air-sea fluxes. Part II: Feedback effects. *Journal of Physical Oceanography*, 44:2835–2853, 2014b. ISSN 0022-3670. doi: 10.1175/JPO-D-13-0246.1.
- . Nolan. What is the trigger for tropical cyclogenesis? *Aust Meteorol Mag*, 56 (August):241–266, 2007. ISSN 00049743.
- D. G. Ortiz-Suslow, B. K. Haus, S. Mehta, and N. J. M. Laxague. Sea Spray Generation in Very High Winds. *Journal of the Atmospheric Sciences*, 73(10): 3975–3995, 2016. ISSN 0022-4928. doi: 10.1175/JAS-D-15-0249.1. URL <http://journals.ametsoc.org/doi/10.1175/JAS-D-15-0249.1>.
- S.-H. Park, J. B. Klemp, and W. C. Skamarock. A Comparison of Mesh Refinement in the Global MPAS-A and WRF Models Using an Idealized Normal-Mode Baroclinic Wave Simulation. *Monthly Weather Review*, 142(10):3614–3634, 2014. ISSN 0027-0644. doi: 10.1175/mwr-d-14-00004.1.
- T. Peng and D. Richter. Influence of Evaporating Droplets in the Turbulent Marine Atmospheric Boundary Layer. *Boundary-Layer Meteorology*, 165(3):1–22, 2017. ISSN 15731472. doi: 10.1007/s10546-017-0285-7.
- T. Peng and D. Richter. Sea Spray and Its Feedback Effects: Assessing Bulk Algorithms of Air-Sea Heat Fluxes via Direct Numerical Simulations. *Journal of Physical Oceanography*, 49(6):1403–1421, 2019. ISSN 0022-3670. doi: 10.1175/jpo-d-18-0193.1.
- H. R. Pruppacher and J. D. Klett. *Microphysics of Clouds and Precipitation*. Atmospheric and Oceanographic Sciences Library. Springer Netherlands, 1996. ISBN 9780792344094. URL [https://books.google.com/books?id=1mXN{}\\_qZ5sNUC](https://books.google.com/books?id=1mXN{}_qZ5sNUC).
- W. E. Ranz and W. R. Marshall. Evaporation from drops: Part 1 and 2. *Chemical Engineering Progress*, 48(3):141–147, 173–180, 1952.
- Y. Rastigejev and S. A. Suslov. Effect of evaporating sea spray on heat fluxes in a marine atmospheric boundary layer. *Journal of Physical Oceanography*, 2019. ISSN 0022-3670. doi: 10.1175/jpo-d-18-0240.1.
- Y. Rastigejev and S. A. Suslov. Two-Temperature Nonequilibrium Model of a Marine Boundary Layer Laden with Evaporating Ocean Spray under High-Wind Conditions. *Journal of Physical Oceanography*, 46(10):3083–3102, 2016. ISSN 0022-3670. doi: 10.1175/JPO-D-16-0039.1. URL <http://journals.ametsoc.org/doi/10.1175/JPO-D-16-0039.1>.
- D. H. Richter. Turbulence modification by inertial particles and its influence on the spectral energy budget in planar Couette flow. *Physics of Fluids*, 27(6), 2015. ISSN 10897666. doi: 10.1063/1.4923043.

- D. H. Richter and D. P. Stern. Evidence of spray-mediated air-sea enthalpy flux within tropical cyclones. *Geophysical Research Letters*, 41:2997–3003, 2014. doi: 10.1002/2014GL059746.
- D. H. Richter and P. P. Sullivan. The Sea Spray Contribution to Sensible Heat Flux. *Journal of the Atmospheric Sciences*, 71(2):640–654, 2014. ISSN 0022-4928. doi: 10.1175/JAS-D-13-0204.1. URL <http://journals.ametsoc.org/doi/abs/10.1175/JAS-D-13-0204.1>.
- D. H. Richter, R. Bohac, and D. P. Stern. An assessment of the flux profile method for determining air-sea momentum and enthalpy fluxes from dropsonde data in tropical cyclones. *J. Atmos. Sci.*, 73:2665–2682, 2016a. ISSN 0022-4928. doi: 10.1175/JAS-D-15-0331.1. URL <http://journals.ametsoc.org/doi/10.1175/JAS-D-15-0331.1>.
- D. H. Richter, O. Garcia, and C. Astephen. Particle stresses in dilute, polydisperse, two-way coupled turbulent flows. *Physical Review E*, 93(1):1–8, 2016b. ISSN 24700053. doi: 10.1103/PhysRevE.93.013111.
- E. Russo, J. G. M. Kuerten, C. W. M. van der Geld, and B. J. Geurts. Water droplet condensation and evaporation in turbulent channel flow. *Journal of Fluid Mechanics*, 749:666–700, 2014. ISSN 0022-1120. doi: 10.1017/jfm.2014.239.
- A. V. Soloviev, R. Lukas, M. A. Donelan, B. K. Haus, and I. Ginis. The air-sea interface and surface stress under tropical cyclones. *Scientific Reports*, 4:1–6, 2014. ISSN 20452322. doi: 10.1038/srep05306.
- P. R. Spalart, R. D. Moser, and M. M. Rogers. Spectral methods for the Navier-Stokes equations with one infinite and two periodic directions. *Journal of Computational Physics*, 96(2):297–324, 1991. ISSN 10902716. doi: 10.1016/0021-9991(91)90238-G.
- R. B. Stull, editor. *An Introduction to Boundary Layer Meteorology*. Springer Netherlands, Dordrecht, 1988. ISBN 978-90-277-2769-5. doi: 10.1007/978-94-009-3027-8. URL <http://link.springer.com/10.1007/978-94-009-3027-8>.
- S. A. Thorpe. *The Turbulent Ocean*. Cambridge University Press, 2005. ISBN 9781139445795. URL <https://books.google.com/books?id=Ax2d94PODgIC>.
- Y. Troitskaya, E. Ezhova, I. Soustova, and S. Zilitinkevich. On the effect of sea spray on the aerodynamic surface drag under severe winds. *Ocean Dynamics*, 66(5):659–669, 2016. ISSN 16167228. doi: 10.1007/s10236-016-0948-9.
- Y. Troitskaya, O. Druzhinin, D. Kozlov, and S. Zilitinkevich. The Bag Breakup Spume Droplet Generation Mechanism at High Winds. Part II: Contribution to Momentum and Enthalpy Transfer. *Journal of Physical Oceanography*, 48(9):2189–2207, 2018a. ISSN 0022-3670. doi: 10.1175/JPO-D-17-0105.1. URL <http://journals.ametsoc.org/doi/10.1175/JPO-D-17-0105.1>.

- Y. Troitskaya, A. Kandaurov, O. Ermakova, D. Kozlov, D. Sergeev, and S. Zilitinkevich. The Bag Breakup Spume Droplet Generation Mechanism at High Winds. Part I: Spray Generation Function. *Journal of Physical Oceanography*, 48(9):2167–2188, 2018b. ISSN 0022-3670. doi: 10.1175/JPO-D-17-0104.1. URL <http://journals.ametsoc.org/doi/10.1175/JPO-D-17-0104.1>.
- G. Tryggvason, M. Ma, and J. Lu. Dns-assisted modeling of bubbly flows in vertical channels. *Nuclear Science and Engineering*, 184(3):312–320, 2016.
- F. Veron. Ocean Spray. *Annual Review of Fluid Mechanics*, 47(1):507–538, 2015. ISSN 0066-4189. doi: 10.1146/annurev-fluid-010814-014651. URL <http://www.annualreviews.org/doi/abs/10.1146/annurev-fluid-010814-014651>.
- F. Veron, C. Hopkins, E. L. Harrison, and J. A. Mueller. Sea spray spume droplet production in high wind speeds. *Geophysical Research Letters*, 39(16):n/a–n/a, 2012. ISSN 1944-8007. doi: 10.1029/2012GL052603.
- C. S. Wang and R. L. Street. Transfers across an air-water interface at high wind speeds: The effect of spray. *Journal of Geophysical Research*, 83(C6):2959–2969, 1978. doi: 10.1029/JC083iC06p02959.
- Y. Wang, J. D. Kepert, and G. J. Holland. The effect of sea spray evaporation on tropical cyclone boundary layer structure and intensity. *Monthly Weather Review*, 129:2481–2500, 2001. doi: 10.1175/1520-0493(2001)129<2481:TEOSSE>2.0.CO;2.
- J. A. Zhang, P. G. Black, J. R. French, and W. M. Drennan. First direct measurements of enthalpy flux in the hurricane boundary layer: The CBLAST results. *Geophysical Research Letters*, 35(14):2–5, 2008. ISSN 00948276. doi: 10.1029/2008GL034374.